THE
PHYSICAL REVIEW

A journal of experimental and theoretical physics established by E. L. Nichols in 1893

SECOND SERIES, VOL. 71, No. 9 MAY 1, 1947

Neutrons From $C^{12}+D$*

W. E. BENNETT** AND H. T. RICHARDS***
The Rice Institute, Houston, Texas
(Received January 17, 1947)

Recoil protons in a cloud chamber have been used to measure the energy spectrum of the neutrons from $C^{12}+H^2$. The neutrons are found to be monochromatic when produced by 2-Mev deuterons. An accurate Q value of -0.27 ± 0.02 Mev is computed from the range of the recoil protons. This Q value gives a mass of 13.00988 ± 0.00004 for N^{13}.

INTRODUCTION

THE neutrons from carbon bombarded by deuterons have been used as a monochromatic source of fast neutrons of variable energy. In the present experiment the energy spectrum of these neutrons has been measured to determine whether or not the neutrons from C^{12} are in fact monochromatic.

EXPERIMENTAL ARRANGEMENT

A thin carbon target was prepared by depositing camphor black on a silver disk. Its thickness was determined by weighing and by comparing the yield of neutrons from it with the yield from a thick graphite target, using the known excitation curve[1] for the reaction to effect the comparison. Its thickness was found to be 75 kev for deuterons of two million volts.

The target was bombarded with 2.00-Mev deuterons from The Rice Institute pressure electrostatic generator. The energy of the neutrons in the forward direction was measured by stereoscopically photographing the recoil protons in a cloud chamber filled to half an atmosphere with methane and 95 percent ethyl alcohol. The cloud chamber was 25 cm in diameter, and its near side was 12 cm from the source of neutrons. Tracks in a strip 8 cm wide from front to rear of the chamber could be measured.

RESULTS

The lengths of tracks of recoil protons in the cloud chamber were measured when the direction of the track was within 15° of the line drawn from the source of neutrons. Tracks as short as one centimeter in length could be measured reliably. The lengths were converted to lengths in standard air using (a) the pressure of gas in the cloud chamber when expanded as measured on a Bourdon gauge, (b) the vapor pressure of 95 percent alcohol and water as given in the International Critical Tables, and (c) the atomic stopping powers of the gases in the cloud chamber as given by Livingston and Bethe.[2] Account was taken of the fact that the methane is

* This work was done in June 1942 under OSRD contract.
** Now at Illinois Institute of Technology.
*** Now at University of Wisconsin.
[1] T. W. Bonner, E. Hudspeth, and W. E. Bennett, Phys. Rev. 58, 185 (1940).
[2] M. S. Livingston and H. A. Bethe, Rev. Mod. Phys. 9, 274 (1937).

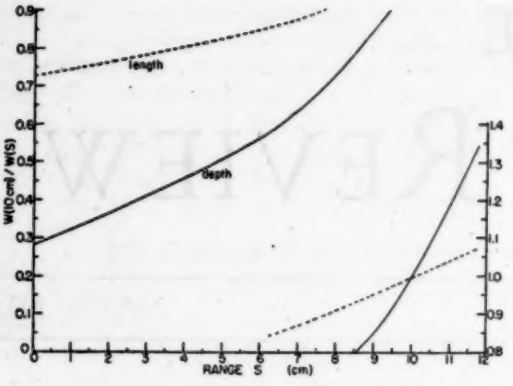

FIG. 1. Geometry corrections. The dotted curve is the correction for the finite length of the cloud chamber while the solid curve is for the finite depth of the illuminated portion of the chamber. S is the observed range in the cloud chamber.

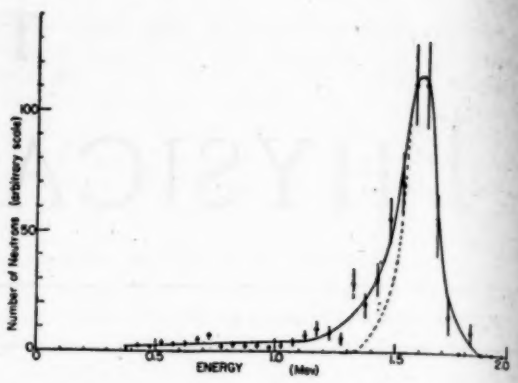

FIG. 2. The energy spectrum of neutrons from a thin target of carbon bombarded by 2.0-Mev deuterons. A methane filled cloud chamber at 0° to the deuteron beam was used for energy measurement.

actually natural gas and is 13 percent ethane. This was checked by determining the density of the gas from the methane cylinder.

Track lengths were converted to neutron energies using the Cornell range-energy curve for protons. The numbers of tracks in each energy interval of 0.05 Mev were counted. These numbers were corrected for the variation with energy of the cross section for neutron-proton scattering and also for geometrical factors which made more probable the measurement of short tracks than of long ones.

Longer recoil protons have smaller probability of being measured because they leave the chamber at the distant wall or at the top and bottom of the illuminated space. (If they left the side of the stereoscopic space they could still be measured on one of the stereoscopic photographs.) Hence, two geometrical corrections were required. The first, for the finite length of the chamber, is

$$W_L=(1/L_0)-1/(L_0+\lambda-S), \qquad (1)$$

where W_L is the probability of observing a track of length S in the rectangular illuminated area of a cloud chamber of diameter λ. L_0 is the distance from the source to the chamber and S is the range in the chamber of the recoil proton. The correction for the finite depth of the chamber is of the simple form

$$W_d=1-4S\sin\theta_0/3\pi d \qquad (2)$$

if the source is infinitely distant from the chamber. θ_0 is the maximum angle that the recoil proton can make with the neutron and still be acceptable for measurement; d is the depth of the illuminated portion of the chamber. However, if the neutron source is not infinitely distant, use of the above expression discriminates against the longer tracks. The correct expression for W_d when the neutron source is at a finite distance from the chamber may be obtained in a manner similar to that used in deriving the above expression;[3] however, the resulting expression is then rather involved and was actually solved numerically for only five different track lengths. A smooth curve was drawn through these five values and the resulting correction curve (normalized to one for a 10 cm track) is plotted on Fig. 1.

The final energy spectrum of neutrons from $C^{12}+D$ is shown in Fig. 2. For comparison, the dotted curve shows the width of a group of monochromatic neutrons, the straggling being caused by (a) the thickness of the target, (b) the fluctuations in voltage of the Van de Graaff machine, (c) the angular straggling of the neutrons which could reach the cloud chamber, (d) the angular straggling of the protons, which were measured out to 15°, and (e) the range straggling. The asymmetry on the low energy side of the group is probably to be attributed to small angle elastic scattering of neutrons in the wall and roof of the cloud chamber on the side toward

[3] H. T. Richards, Phys. Rev. 59, 796 (1941). The expression derived in this reference is for a different geometry than used in the present cloud-chamber measurements.

the neutron source. The wall was one-quarter inch of iron and the roof was one inch of glass.

The constant background at low energies probably represents scattering by the walls of the room rather than slow neutrons from the source. A blank run was taken with no carbon on the silver disk and the number of neutrons observed was negligible. Therefore, not more than a few percent of the neutrons observed could have been produced by the molecular beam in the analyzer.

The graph shows that the mean energy of the neutron group is 1.60 Mev. This becomes 1.65 Mev when corrected because recoil protons were measured out to 15°. The mean deuteron energy in the target was 1.96 Mev. This gives an energy evolution of $Q=-0.27\pm0.02$ Mev in the reaction.

CONCLUSIONS

The neutrons from carbon bombarded by deuterons are monochromatic, except for the high energy neutrons from C^{13}, when produced at 2 Mev; and are therefore likely to be monochromatic when produced at lower bombarding voltages.

The Q of the reaction is -0.27 ± 0.02 Mev. This value is believed to be more accurate than previous determinations.[4] This Q value gives a mass of 13.00988 ± 0.00004 for N^{13}.

[4] J. D. Cockcroft and W. B. Lewis, Proc. Roy. Soc. **154**, 261 (1936). $Q\geq-0.28$ Mev (from theshold of reaction).
T. W. Bonner, Phys. Rev. **53**, 496 (1938). $Q=-0.25\pm0.05$ Mev (from recoil protons in cloud chamber).
W. E. Bennett, T. W. Bonner, E. Hudspeth, H. T. Richards, and B. E. Watt, Phys. Rev. **59**, 781 (1941). $Q=-0.19\pm0.05$ Mev (from recoil protons in cloud chamber).

PHYSICAL REVIEW VOLUME 71, NUMBER 9 MAY 1, 1947

On the Neutron-Proton Scattering Cross Section

D. BOHM* AND C. RICHMAN
*Radiation Laboratory, Department of Physics, University of California,** Berkeley, California*

(January 22, 1947)

The sensitivity of the theoretical neutron-proton scattering cross section to possible variations in the quantities defining the potential has been investigated in the energy range from 0 to 6 Mev. It is found that in this energy range the variations in exchange or tensor character and range of the potential which are consistent with what is known about the interaction do not result in so large a modification of the predicted cross section as do variations in shape.

A well resembling a Yukawa potential ($A\exp(-\alpha r)/r$) is found to yield a cross section at 6 Mev which is 10 percent lower than that given by a square well fitted to the epithermal neutron cross section and the binding energy of the deuteron. The Yukawa well is in better agreement with experiment than is the square well. One of the constants entering into the determination of the potential is the epithermal neutron scattering cross section in hydrogen. We have determined this by extrapolating the data of Frisch with the aid of the theory, and obtained a value of 20.8×10^{-24} cm².

INTRODUCTION

CURRENT nuclear theories attempt to correlate all known facts about nuclear scattering and nuclear binding by means of the assumption that these phenomena are caused by a potential energy of interaction between the fundamental particles. Unfortunately, the present data are too meager and too crude to permit the determination of this potential in any but the most schematic way. As a result, it is desirable to find out how critically the predictions for experimental results depend on each of the many parameters needed to specify the potential, and thus to indicate the range and accuracy of experiments needed to determine any feature of the potential within the limits desired.

In this paper, the neutron-proton scattering cross section is investigated in the energy range

* Now at Princeton University.
** Contract No. W-7405-Eng-48.

from 0 to 6 Mev. The object of this investigation is to estimate the extent to which the predicted cross sections will vary when the potential is given the largest possible modifications which seem to be consistent with all data other than that of neutron-proton scattering. When this work was done, there was so little systematic information about the neutron-proton scattering cross section, that our emphasis was placed on estimating the uncertainties in the predicted cross section, on the basis of data then in existence. Since then, fairly complete measurements in the energy range have been made available,[1,2] and our results can now be used not only to provide closer limits on the potential, but also to indicate the direction in which the theory may be modified, if necessary, to obtain better agreement with experiments.

The four main independently specificable features of the potential are: (a) range, (b) fraction of tensor force, (c) exchange character, and (d) shape. The depths of singlet and triplet wells in neutron-proton interaction are most conveniently determined in terms of the other four features with the aid of two reliably known constants, the binding energy of the deuteron, and the epithermal neutron-proton scattering cross section.

Probably the feature of the potential about which the least is known is the shape. In fact, it is found that a square well fits all data other than that of neutron-proton scattering above 3 Mev about as well as any other shape. Since the modifications in cross section resulting from likely modifications in shape are not expected to be large, the analytic simplicity of the square well may be utilized advantageously in investigating the sensitivity of the cross section to features other than the shape. The study of effects of variations in shape will then be deferred until the other three parameters have been taken up.

I. VARIATION IN RANGE

The range of nuclear forces is usually determined by means of a detailed investigation of the variation of cross section with energy. In this way, Breit, Thaxton, and Eisenbud[3] have been able to estimate the range of proton-proton forces with considerable accuracy, obtaining a value of $(2.8\pm0.4)\times10^{-13}$ cm^2, with a square well. In the absence of grounds to the contrary, the tentative assumption is usually made that the range of neutron-proton forces is the same as that of proton-proton forces. This assumption, at present, obtains some qualitative support from the general features of nuclear binding, but its main quantitative support is twofold. First, it is found[3,4] that if the neutron-proton singlet well is taken to be the same as that for proton-proton interaction, the epithermal neutron-proton scattering cross section and other low energy neutron-proton cross sections, can be fitted within experimental error. Second, calculations of Rarita and Schwinger[5] show that a square well of radius 2.8×10^{-13} cm^2 is consistent with the observed quadripole moment of the deuteron. That the range of neutron-proton forces is not much less than that of proton-proton forces is made clear by the calculations of Sen,[6] which indicate that a well of radius 2.4×10^{-13} cm is the narrowest that can yield simultaneously the correct quadrupole moment and magnetic moment.

In the interests of seeking the simplest hypothesis consistent with what is now known about nuclear interactions, it seems desirable to retain the assumption of equality of all nuclear forces, and to try to obtain agreement with experiment within the limits of this hypothesis. If this assumption is made, it is then of interest to investigate the variations in the neutron-proton cross section which may result from the uncertainty of the proton-proton forces, as obtained from proton-proton cross sections. In accordance with proton-proton data, a range of 2.8×10^{-13} cm was taken to be the most probable, with permissable variations as large as 0.4×10^{-13} cm. Calculations showed that this uncertainty in the radius introduced an uncertainty of 5 percent in the cross section at 6 Mev, with

[1] C. L. Bailey, William E. Bennet, T. Bergstrahl, Richard G. Nucholls, H. T. Richards, and J. H. Williams, Phys. Rev. 70, 118 (1946); Phys. Rev. 70, 583 (1946).
[2] Bretscher (to be published).
[3] Breit, Thaxton, and Eisenbud, Phys. Rev. 55, 1018 (1939).
[4] L. E. Hoisington, S. S. Share, and G. Breit, Phys. Rev. 56, 884 (1939).
[5] W. Rarita and J. Schwinger, Phys. Rev. 59, 436 (1941) and 59, 556 (1941).
[6] Sen (unpublished).

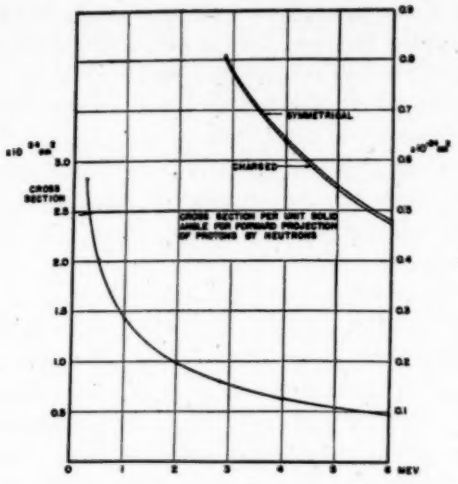

FIG. 1. Upper curves are drawn with expanded ordinate in order to show the extent of uncertainty arising from lack of knowledge of the exchange character of nuclear forces.

correspondingly smaller uncertainties at lower energy. The cross section is larger, the larger the nuclear radius. The reason for the comparatively small sensitivity to nuclear radius, exemplified by the fact that a 5 percent change in cross section accompanies a 30 percent reduction in the "area" of the well, is that the depth is always adjusted to give the correct deuteron binding energy and epithermal neutron-proton cross section.

II. TENSOR FORCES

Tensor forces are introduced into nuclear interactions in order to account for the observed quadrupole moment of the deuteron. Rarita and Schwinger[5] have shown that a variation in the fraction of tensor force of about $\frac{1}{10}$ is consistent with the probable error in the quadripole moment. It is, therefore, necessary to determine whether this uncertainty in the tensor force affects the cross section. It may be expected that the effect of this uncertainty will be small, because at moderate energies, the tensor force behaves very much like an addition to the ordinary radially symmetrical force, except for the production of a small D wave, which is responsible for the quadrupole moment. The expectation is borne out by the calculations of Rarita and Schwinger[5] and Sen,[6] who show that for a radius of 2.8×10^{-13} cm, the tensor force results in a reduction of only 2 percent in the triplet cross section at 0 Mev and at 2.82 Mev. Sen also shows that these cross sections are not changed appreciably when the fraction of tensor force is varied from 0.5 to 1.

The effects of tensor forces at higher energies can be estimated from the results of Rarita and Schwinger,[5] who give the $3S_1+3D_1$ cross section at 15.3 Mev, when the fraction of tensor force is adjusted to obtain agreement with the quadrupole moment of the deuteron. We find that this cross section is only 1 percent greater than that predicted by ordinary forces at this energy. Hence, it seems safe to conclude that, in the range from 0 to 6 Mev, the uncertainty in the fraction of tensor force should produce a negligible uncertainty in the cross section. In fact, even the complete neglect of the effects of tensor forces should result in an error of less than 2 percent in the cross section in this energy range. We have, therefore, decided that, for the purpose of studying the sensitivity of cross section to other parameters, the use of tensor forces is not necessary. Their effect will then be taken into account approximately, however, by means of a uniform reduction of 2 percent in all $3S$ cross sections.

III. EXCHANGE FORCES

Exchange forces are introduced into nuclear interactions for the purpose of explaining the saturation character of nuclear binding. A fairly wide range of combinations of exchange and ordinary forces is, however, consistent with the present experimental data. It is, therefore, necessary to find out whether the cross section depends appreciably on the precise exchange character of the forces in the range from 0 to 6 Mev.

The combinations studied in this paper were, in the terminology of Rarita and Schwinger, the "charged" and the "symmetric" theories, which represent about the widest possible variation in the exchange character consistent with the existence of saturation. The results of the calculations showed that the contribution of the "P" wave to the total cross section was so small that the exchange character did not make an appreciable difference in this cross section. Even the angular dependence varied by less than 1 percent (see Fig. 1). In order to understand the smallness of the angular dependence, it is helpful to analyze

the sources of the P scattering. On account of the spin dependent tensor forces which operate only in the triplet state,[5] the phases are different for $^3P_0$, $^3P_1$, and $^3P_2$. The calculations showed that although the $^3P_0$ phase was fairly large from 4 to 6 Mev, the angular dependence arising from it was almost cancelled by that arising from the $^3P_1$ and $^3P_2$ phases, which are smaller, but which occur with greater statistical weight. The reason for this cancellation is that the tensor forces average out to zero in the first approximation. The net result is that practically all the angular dependence arises from the singlet state, which occurs with only one-fourth of the total weight. Consequently, both the angular dependence of the cross section and its uncertainty arising from the uncertainty in the exchange character, are very small below 6 Mev.

IV. SHAPE

Up to this point, the sensitivity of the cross section to possible variations in the parameters specifying the potential has been studied with the aid of the simplifying assumption of a square well. It is now necessary to estimate the effects of possible derivations from the square shape. The principal deviations from the square form which are significant for moderate energy scattering are (a) a tail and (b) a concentration of force near the origin. Hoisington, Share, and Breit[4] have studied such variations in the case of proton-proton scattering, and have found that the best agreement with experiment is obtained by making these two modifications simultaneously. For example, they find that the exponential well, which is characterized mainly by a long range tail without a great concentration of force near the origin, predicts both a wrong energy dependence for "S" scattering and excessive "P" anomaly. On the other hand, the Yukawa potential ($A \exp(-\alpha r)/r$), which embodies both the tail and the necessary concentration of potential, is found to fit the proton-proton data as well as the square potential, while it is also in very good agreement with the epithermal neutron-proton cross section. It is necessary, however, to choose a range corresponding to a meson mass of 300 electron masses. The significance of the disagreement of this value with that of 200 electron masses obtained from cosmic-ray experiments is not clear at present, particularly because of the uncertain status of the details of all current meson theories. In any case, it seems that a Yukawa potential with this range represents about the widest variation in shape from that of a square well which is consistent with the hypothesis of equality of all nuclear forces, and it is, therefore, the most promising one for study.

In order to simplify the calculations, and to separate clearly the effects of the tail from those of the concentration of force near the origin, it is obviously permissible to represent these two main features by an L-shaped potential, consisting of a deep short range well followed by a shallow long range well. The proportions of the L should be chosen to give a general resemblance to the above Yukawa potential in the range of importance, which is in the region from 10^{-13} cm to 5×10^{-13} cm. This method of fitting yields somewhat ambiguous results, but it turns out that almost any proportions of the L which lie within the range of ambiguity yield practically the same cross sections, if the depths are adjusted to yield the deuteron binding energy and epithermal neutron-proton cross sections. The small adjustment of singlet depth needed to give the epithermal neutron-proton cross section is easily within the range of the ambiguity in fitting. Since the L well now resembles the Yukawa potential which also gives the correct proton-proton and epithermal neutron-proton scattering, and because this agreement is not critically dependent on the precise proportions of the well, it may be concluded that the small ambiguity in shape has no important effect on the cross section.

A further requirement which the L-shaped potential must satisfy is that it gives the correct quadrupole moment of the deuteron. According to the work of Sen, the radius of the concentration of the force near the origin which we have chosen (2.2×10^{-13} cm) is definitely below that needed without a tail to give simultaneously the correct quadrupole moment and magnetic moment. The tail is, however, very effective in producing quadrupole moment, which is proportional to the mean value of r^2. Because the magnetic moment is proportional to r, the tail is less effective in producing it Approximate calcu-

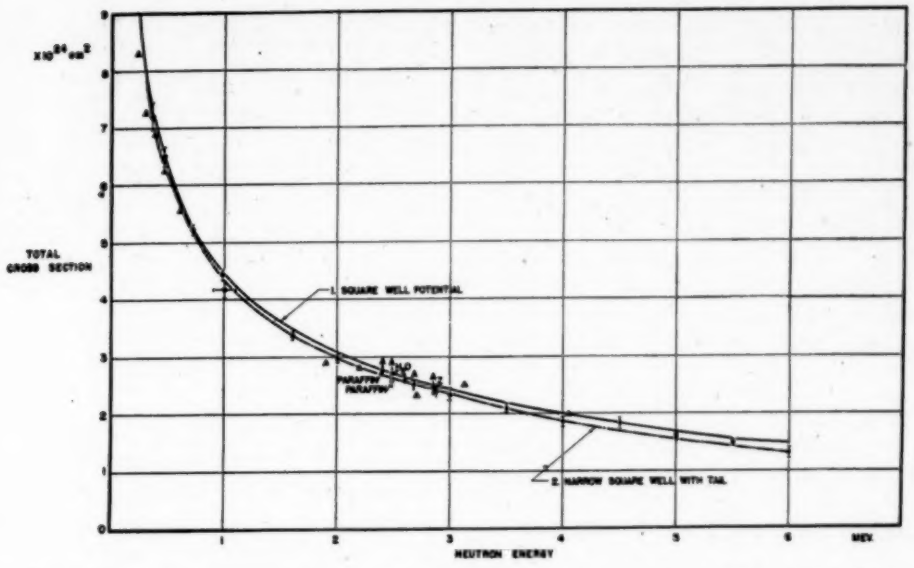

FIG. 2. Comparison of cross section for neutrons-proton scattering for two different well shapes. Specification of wells.—1. Square well-range 2.8×10^{-13} cm. Singlet depth: 11.85 Mev; Triplet depth: 21.2 Mev. 2. Narrow square well with tail: a. Square well-range 2.2×10^{-13} cm. Singlet depth: 18.39 Mev. Triplet depth: 30.33 Mev. b. Square tail-range $2.2\text{–}5.6\times10^{-13}$ cm. Single depth: 0.3 Mev. Triplet depth: 0.5 Mev. ⊹ Experimental points. ⊹ Williams, *et al.* △ Bretscher, *et al.* *A*—Aoki. *Z*—Zinn, Seeley and Cohen.

lations show that the well chosen by us can yield the correct quadrupole moment and magnetic moment of the deuteron within experimental error, and that the fraction of tensor force needed to obtain the agreement is about the same as that obtained by Rarita and Schwinger[5] for a square well of radius 2.8×10^{-13} cm.

V. RESULTS

The cross sections were calculated in the usual way, which is too well known to require further discussion.[7] Our results (Fig. 2) show that the L-shaped well yields a cross section which is at 6 Mev, 10 percent lower than that predicted by the square well, with correspondingly smaller differences at lower energies. Below 1 Mev, the difference in cross sections is practically undetectable. It is of interest to understand why the cross sections behave in this manner. The agreement at low energies is, of course, a consequence of the fitting of the binding energy of the deuteron and the epithermal neutron-proton scattering cross section. At higher energies, the "tail," which is only 0.5 Mev deep, begins to have very little effect on the wave function, and the main part of the scattering is then due to the deep narrow well at the center.

Because the tail is very effective at low energies, however, the concentration of potential near the origin is not actually deep enough to produce by itself the correct binding or epithermal neutron scattering cross section. If the depth were such as to give the correct deuteron binding and epithermal scattering, then the narrowing of the effective radius would result in a considerable decrease in the triplet cross section, and a slight decrease in the singlet cross section.[8] The decrease of effective depth, however, decreases the slope of the wave function at the edge of the well,[8] and thus introduces a tendency to increase the cross section. In the singlet state, this increase is the main effect, but in the triplet state, it is considerably over-balanced by the decrease resulting from the narrowing of the well. Because the increase of singlet cross section is less than the decrease of triplet cross section, and because of the greater statistical weight of the triplet

[7] Mott and Massey, *Theory of Atomic Collisions*, Chapter II.

[8] H. A. Bethe and R. F. Bacher, Rev. Mod. Phys. **8**, 83 (1936).

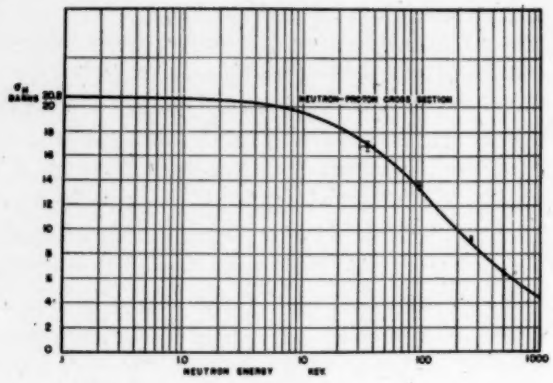

FIG. 3.

state, the net effect is to decrease the cross section at high energies.

VI. COMPARISON WITH EXPERIMENTS

The best early experiments are those of Aoki,[9] and those of Zinn, Seely, and Cohen,[10] which cover a range from 2.1 to 2.9 Mev. Later experiments[1,2] done after this work was completed, cover a range from 0.35 Mev to 6 Mev. In general, the experimental cross sections are in much better agreement with the L well than with the square well, wherever the two predictions differ. Although experimental errors are great enough to permit the assignment of a square well of range 2.4×10^{-13} cm, which would give a 6 Mev, a cross section 5 percent below that given by the well of range 2.8×10^{-13} cm, the mean of the data is in definitely better agreement with the predictions of the L-shaped well. Besides, the range of 2.4×10^{-13} cm is probably the extreme limit of error in the proton-proton range, and not a particularly likely value. Since the square shape has nothing to recommend it, except analytic simplicity, it seems preferable to assume tentatively that the well resembles a Yukawa potential.

One of the most important parameters used in the choice of a potential is the epithermal neutron-proton cross section. A very accurate value of this quantity was obtained by extrapolating to zero energy with the aid of the theory, the neutron-proton cross sections of Frisch,[11] which were made in the energy range from 35 kev to 490 kev. Because the uncertainties in the potential do not appreciably affect the cross section at these low energies, the extrapolation is quite reliable. This is verified in Fig. 3, which shows that the variation of cross section with energy in this range is in very good agreement with the theory. The extrapolated value of the epithermal cross section is 20.8×10^{-24} cm^2, as compared with the previously accepted value of $(20\pm2)\times10^{-24}$ cm^2.[12]

More work on this problem is desirable, particularly with regard to obtaining a more systematic study of the sensitivity of cross section to shape. Now that a Yukawa potential seems to give better agreement with experiment than a square well, an effort should be made to fit a Yukawa potential directly to all known data, including proton-proton scattering, neutron-proton scattering, binding energy of the deuteron, and quadripole and magnetic moments of the deuteron. The prediction of the cross sections at energies above 6 Mev, where the exchange and tensor character of the forces is important, is particularly significant. Some theoretical work has already been done on this problem.[13] It is necessary at higher energies to consider the possibility that the fundamental interactions cannot be described in terms of a potential, which is a function only of the relative coordinates.

We are greatly indebted to Professor Bethe and Mr. Sen for sending us some very helpful manuscripts. It is also a pleasure to acknowledge gratefully the help and encouragement received from Professor Oppenheimer and Professor Serber in the solution of the problem. This work was carried out under the auspices of the Manhattan District.

[9] H. Aoki, Proc. Phys. Math. Soc. Japan **21**, 232 (1939).
[10] W. H. Zinn, S. Seely, and V. W. Cohen, Phys. Rev. **56**, 260 (1939).
[11] D. Frisch, Phys. Rev. **70**, 589 (1946).
[12] V. W. Cohen, H. H. Goldsmith, and J. Schwinger, Phys. Rev. **55**, 106 (1939); H. B. Hanstein, Phys. Rev. **57**, 1045 (1940).
[13] J. Leites Lopes, Phys. Rev. **70**, 5 (1946). A list of references to the latest theoretical work on this subject is contained in this paper.

Yield of Photo-Neutrons from U^{235} Fission Products in Heavy Water*

S. BERNSTEIN, W. M. PRESTON, G. WOLFE, AND R. E. SLATTERY
Clinton Laboratories, P. O. Box 1991, Knoxville, Tennessee

(Received January 20, 1947)

The photo-disintegration of the deuteron has been used to study the hard γ-rays emitted by fission products of U^{235}. The neutrons created in the process were used as the indicator of the presence of hard γ-rays. The fission products were placed at the center of a 10″ radius sphere of heavy water. Conclusions about the periods and yields of the hard γ-rays were made from the total number of photo-neutrons being captured in a large tank of oil surrounding the sphere of heavy water. Eight half-lives were found: 2.5 sec., 41 sec., 2.4 min., 7.7 min., 27 min., 1.6 hr., 4.4 hr., and 53 hr. The shortest one and longest one of these are least reliable. Eighty-five percent of the photo-neutrons appear in the two shortest half-lives, the 2.5-sec. component being three times as intense as the 41 sec. component. The total saturated activity of the photo-neutrons for an infinite amount of heavy water was calculated from the 10″ radius sphere measurements to be about 16.5 percent of the saturated delayed neutron activity. It is calculated that there must be of the order of one to two photons of energy above 2.2 Mev emitted per fission by fission products with half-lives greater than one second.

I. INTRODUCTION

THE threshold property of the photo-disintegration of the deuteron can be used as a crude γ-ray spectrometer. The reaction

$$\gamma + D \rightarrow n + p$$

requires that the energy of the γ-ray be at least 2.17 Mev[1] (the binding energy of the deuteron). The use of this reaction immediately "resolves" γ-rays above the threshold from those below, independently of the relative intensities of the two groups. It is convenient to use the neutrons created in the process as an indicator of the presence of hard γ-rays, since they may be slowed down by a moderating medium to thermal energies where they are easily detected. The total relative number of photo-neutrons produced is also a fairly easily determined quantity. It is a measure of the relative intensity of the hard γ-rays. We have studied the periods and yields of photo-neutrons produced in heavy water by the γ-rays from U^{235} fission products and from these yields have estimated the corresponding yields of the high energy γ-rays themselves.

II. APPARATUS

A schematic diagram of the apparatus is shown in Fig. 1. It consisted of a ten-inch radius, $\frac{1}{8}$-inch wall, aluminum sphere immersed in a large tank of oil. A "rabbit" containing a sample of enriched uranium oxide could be transferred from the center of the Clinton Laboratories chain-reacting pile[2] to the center of the sphere in about 0.25 sec. by means of a pneumatic tube. The sphere could be filled or emptied of heavy

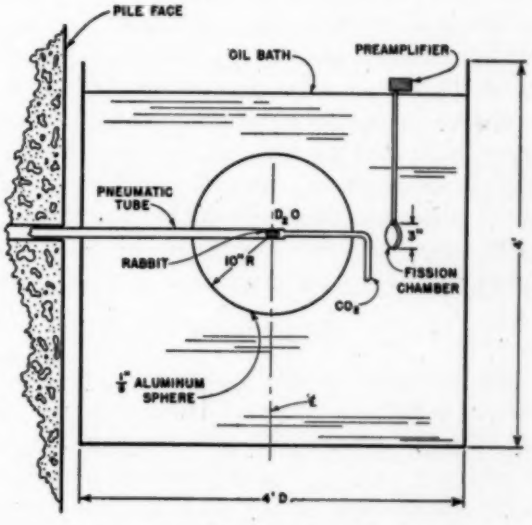

FIG. 1. Schematic diagram of apparatus.

* This document is based on work performed at Clinton Laboratory operated by Monsanto Chemical Company under contract No. W-35-058-eng-71 for the Manhattan Project and the information covered therein will appear in Division IV of the Manhattan Project Technical Series, as part of the contribution of Clinton Laboratories.

[1] F. T. Rogers, and M. M. Rogers, Phys. Rev. 55, 263 (1939).

[2] H. D. Smyth, *Atomic Energy for Military Purposes* (Princeton University Press, Princeton, 1945), Chapter VI; or Rev. Mod. Phys. 17, 392 (1945).

FIG. 2. Sample of film recorded data.

water in about one minute by means of a siphon arrangement. The number of photo-neutrons created in the sphere of heavy water by the fission product γ-rays was determined by studying the neutron distribution in the oil by means of fission chamber detectors. The chamber could be placed at chosen reproducible radial positions in the tank by means of a track and carriage arrangement. Since some of the periods involved are fractions of a second, it was necessary to keep the initial counting rates quite high in order to obtain good statistics throughout the run. An available amplifier and scaling circuit found to have a resolving time of 20 microseconds was adapted for use in the experiment. Exposure times and sample sizes were adjusted so that corrections for missed counts reached 5 percent only at the start of one or two of the runs. Fission pulses from the amplifier were fed into a scale of 256. The data were recorded by photographing the scaling circuit interpolation bulbs with an open shutter oscilloscope camera. The film moved past the neon bulbs in such a manner that each bulb appeared on the film as a dashed line for the period the bulb was lit. A time signal was impressed on the film every 0.1 second by means of a neon bulb and a revolving shutter driven by a synchronous motor. Another signal lamp connected through the electropneumatic control switch recorded the length of an exposure. Figure 2 shows a reproduction of a typical film.

III. METHOD

The method employed to measure the source activity is based on the following theory. Consider a point source of Q neutrons/sec., having an arbitrary energy distribution (above thermal energy), surrounded by an oil bath large enough to absorb all the neutrons. It is known that the absorption in the oil is caused almost entirely by capture of thermal neutrons by the protons. The number of captures of neutrons of energies higher than thermal is negligible. In the steady state the rate of production of neutrons must equal the rate at which they are captured, or $Q=\int(nv)_t\sigma_c dv$, where $(nv)_t$ is the flux of thermal neutrons at any point in the oil, σ_c is the macroscopic cross section for capture at thermal energy, and the integral is extended over the oil volume. Measurements with a fission chamber detector give a counting rate Y at any point in the oil which is proportional to $(nv)_t$, provided correction is made for the epicadmium counting rate.

For spherical symmetry, $Q \propto \int YR^2dR$. In our case, since there is negligible neutron absorption in the heavy water sphere, the integral is taken from R_0 to ∞, where R_0 is the sphere radius.

The ion chamber was fixed in a given radial position, the sample was sent into the pile for a fixed exposure time, then sent to the center of the sphere, and the resulting neutron counting rate recorded on the moving film as a function of time "t" after the end of the exposure. When the activity had decreased to an acceptable value, the ion chamber was moved to the next radial position and another exposure made with the same sample. A single series usually comprised exposures in four to eight positions. A complete experiment required three complete series: (*a*) with heavy water in the sphere, in which case both delayed and photo-neutrons are present; (*b*) with the sphere empty, so that the activity is that caused by delayed neutrons alone; and (*c*) with the sphere empty and the fission chamber surrounded by cadmium, in order to measure the delayed neutrons with epicadmium energies. With heavy water in the sphere the number of epicadmium neutrons was negligible.

The constancy of the pile power level and the detecting instruments was checked by repeating the initial exposure at the end of each experiment. Instrument sensitivity alone was checked by means of a Ra-α-Be source. Variations in the

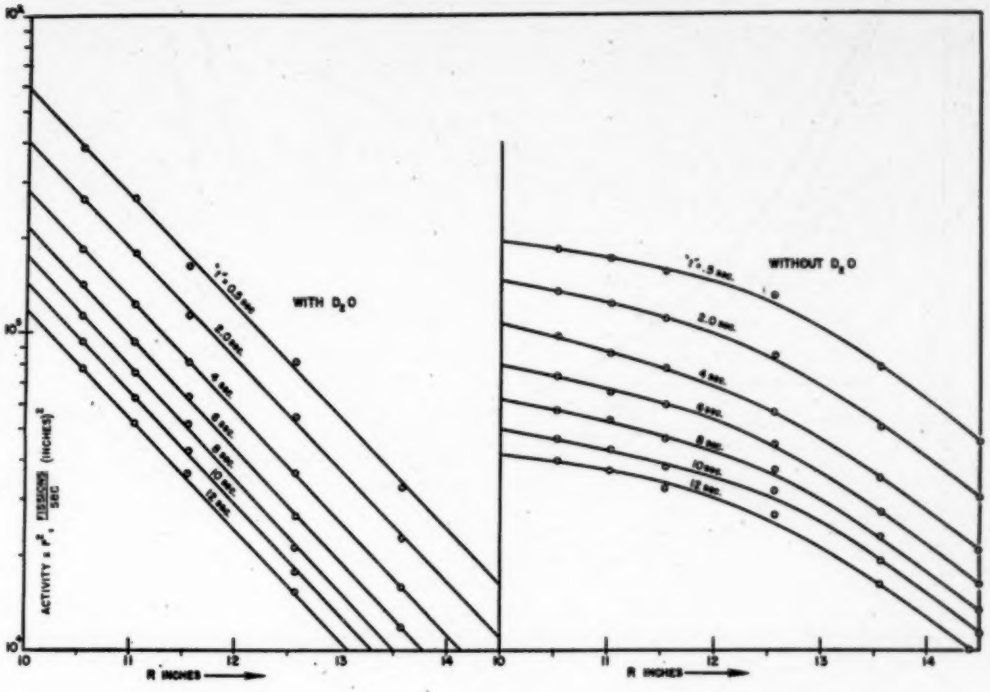

FIG. 3. Activity $\times R^2$ *vs.* R curves at different times t after the end of a 30-sec. exposure.

pile power level were found to be less than one percent over the period during which a set of data was taken, so that the use of an exposure monitor was not necessary.

For each exposure, a plot was made from the film data of the counting rate in the particular radial position as a function of t. From the group of curves forming a series, other curves were constructed of (counting rate$\times R^2$) *vs.* R, for successive fixed values of t. Here, R is the radial distance of the detector from the source at the center of the sphere. The source activity at any time is then proportional to the area under the corresponding curve.

TABLE I.* Delayed neutrons from U^{235}. τ=mean life, $\tau_{\frac{1}{2}}$=half-life, E=energy in Mev, A=saturated exposure yield relative to the yield of the 22-sec. period.

$\tau_{\frac{1}{2}}$	τ	E(Mev)	A
55.6	80.2	0.25	0.153
22.0	31.8	0.56	1.00
4.51	6.50	0.43	1.28
1.52	2.19	0.62	1.45
0.43	0.62	0.42	0.51
0.05	0.07		0.15
		Total	4.54

* Data for the first five periods from unpublished work of D. J. Hughes, J. Dabbs, and A. Cahn; for the shortest period from D. Hall.

Examples of these (counting rate$\times R^2$) *vs.* R curves are shown in Fig. 3. With heavy water in the sphere, the curves on a semi-log scale are linear with a relaxation length (inverse slope) which is constant and equal to 1.25 inches. This indicates that the neutrons have been well thermalized before they escape into the surrounding oil. When the sphere is empty, the semi-log plot of the neutron distribution shows a decided initial curvature caused by slowing down in the oil.

In general, the desired source activity due to photo-neutrons alone, at a time t_1, is the difference between the areas under the corresponding distribution curves, with and without heavy water, after correction for epicadmium activity. By computing a number of points, a curve may be drawn of source photo-neutron activity as a function of time.

We assume that the data can be represented by a formula of the form (1), where A_p is the photo-neutron activity of the source as a function of time t after the end of the exposure,

$$A_p(t)=\sum_i a_i(1-\exp-[T/\tau_i])\exp-[t/\tau_i], \quad (1)$$

T is the exposure time, τ_i the mean life, and a_i, the yield, is the activity of the ith radioactive com-

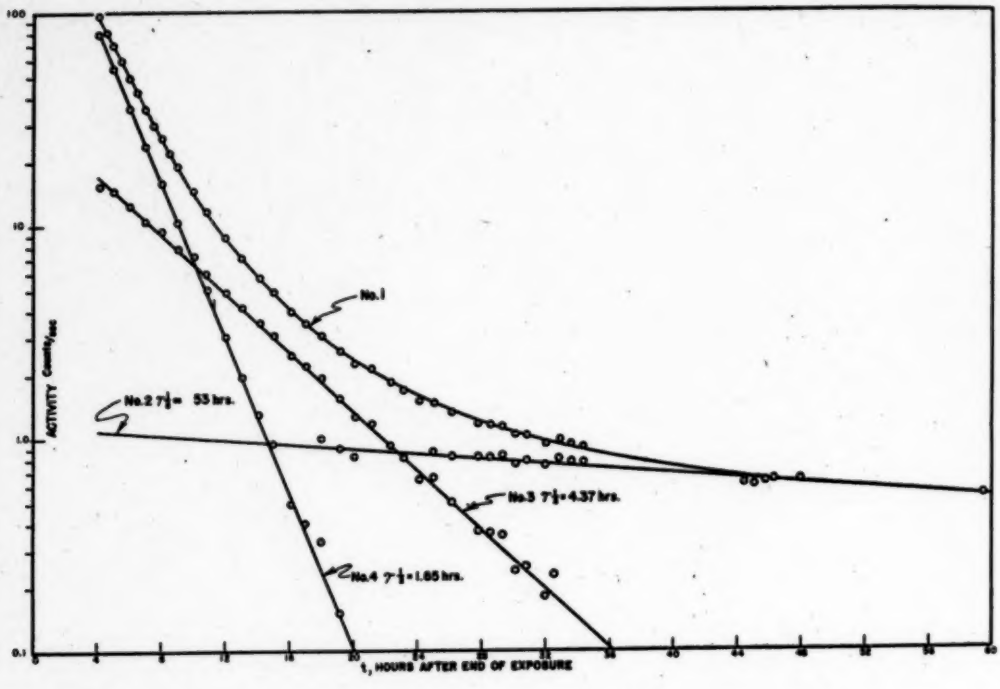

FIG. 4. 3.75-hour exposure with D_2O. Curve No. 1 shows unanalyzed data, which are decomposed into curves 2, 3 and 4 of half-lives, 53 hours, 4.4 hours, and 1.6 hours, respectively.

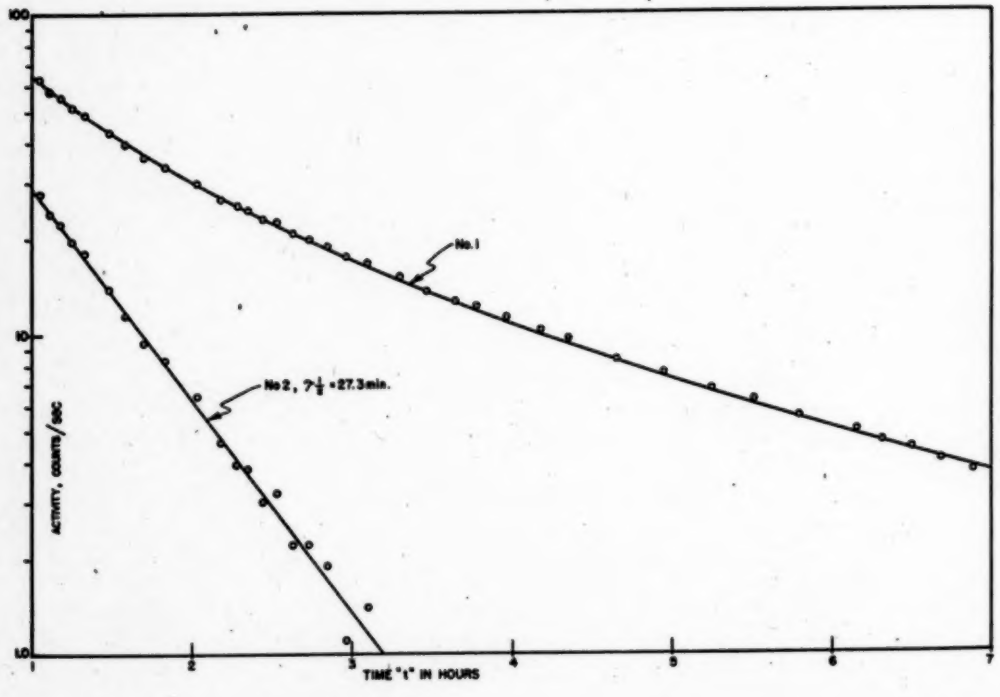

FIG. 5. Thirty-minute exposure with D_2O. Curve No. 1 shows unanalyzed data. Curve No. 2 of half-life 27 minutes is obtained by subtracting from curve 1 the activities caused by the 53-hour, 4.4-hour, and 1.6-hour periods.

ponent for $T=\infty$, $t=0$. The longest period is determined first, at large values of t when all shorter periods have died out, and its activity subtracted from the total. The shorter periods are determined, successively, by a repetition of the process. A similar formula for $A_d(t)$, the delayed neutron activity, was fitted to the decay curve taken with the sphere empty. In this case, the yields and periods[3] were taken from Table I.

[3] The yields and periods of the delayed neutrons have been studied by several groups of workers on the uranium project. One of the earliest studies is that of A. H. Snell, J. S. Levinger, R. G. Wilkinson, E. P. Meiners, and M. B.

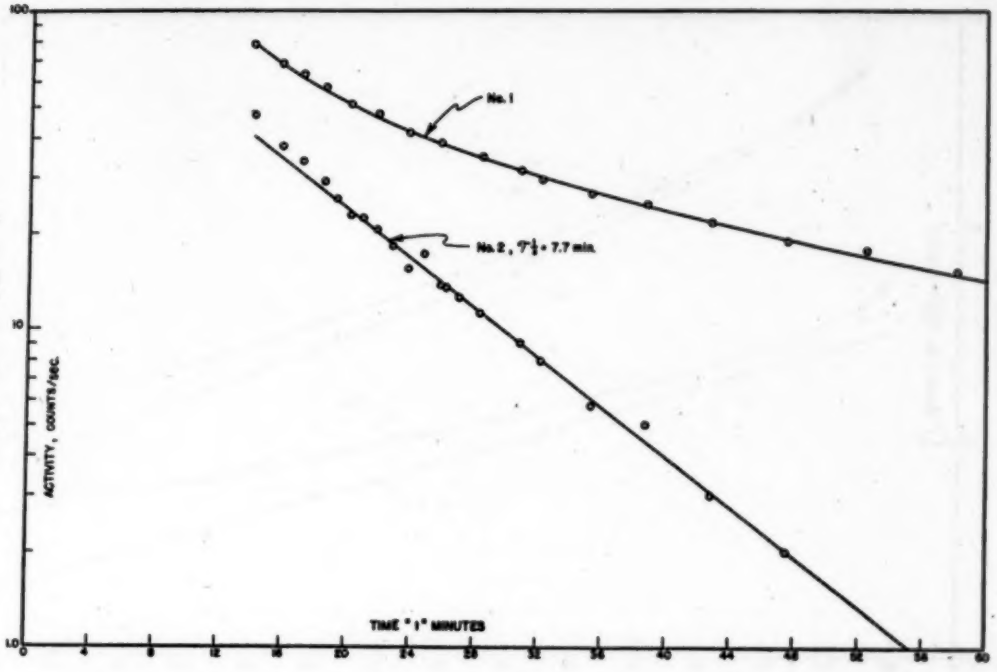

FIG. 6. Five-minute exposure. Curve No. 1 shows unanalyzed data. Curve No. 2 of half-life 7.7 minutes is obtained from curve No. 1 by subtracting the activities caused by the 4 longer periods.

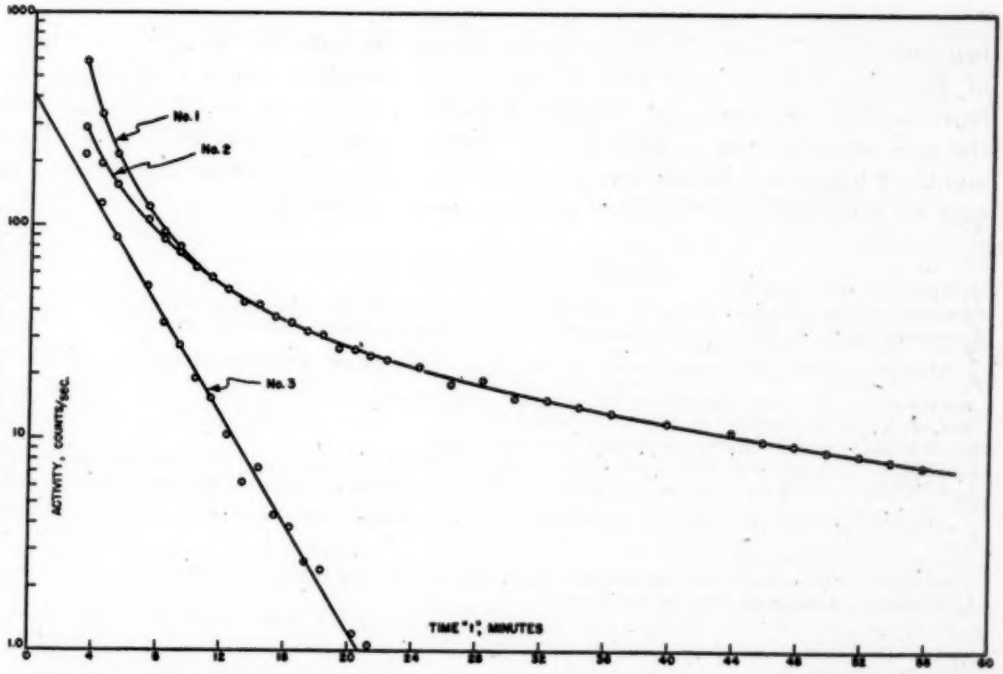

FIG. 7. Three-minute exposure. Curve No. 1 is the total activity with D_2O. Curve No. 2 is obtained from curve No. 1 by subtracting the delayed neutron activity. Curve No. 3, showing 2.4 minute half-life, is obtained from curve No. 2 by subtracting the activities caused by the 5 longer periods.

By extrapolation to $t=0$, $T=\infty$, we can then express the yields a_i of each photo-neutron period as fractions of the total delayed neutron yield $A_d(t=0, T=\infty)$.

Sampson, Phys. Rev. **70**, 111 (1946). The values in Table I were taken from more recent unpublished work of D. J. Hughes, J. Dabbs, and A. Cahn, and also from the work of D. Hall.

IV. EXPERIMENTAL RESULTS

A. Periods and Uncorrected Yields

The longest delayed neutron component has a half-life of 55 seconds, so for $t > 10$ min. the delayed neutron activity is negligible in comparison with that of the longer period photo-

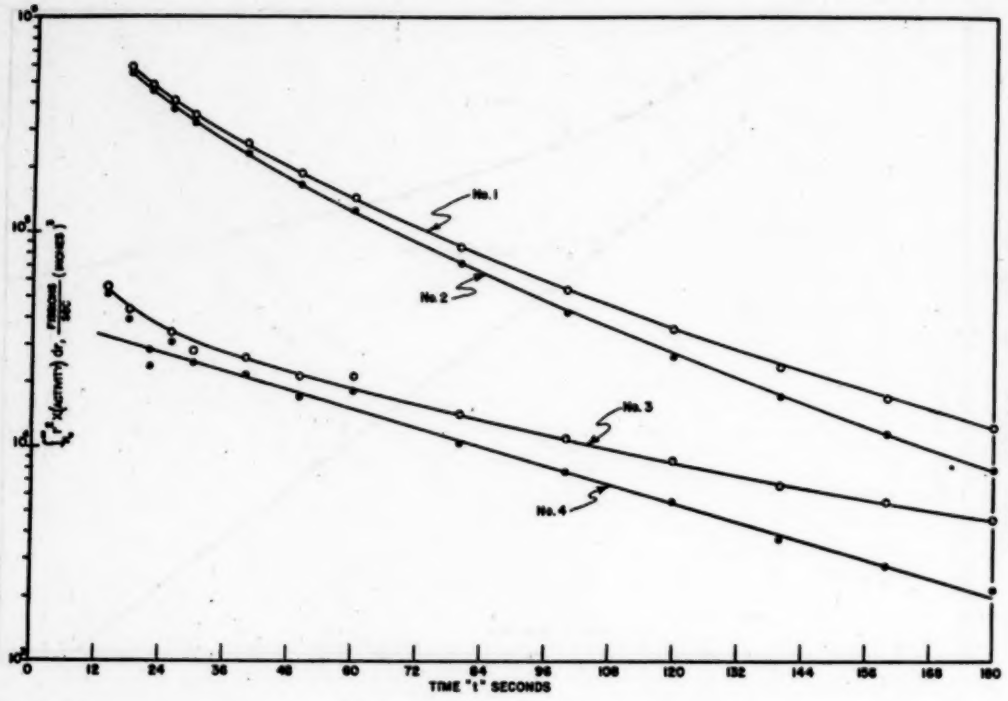

FIG. 8. Thirty-second exposure volume integrals. Curve No. 1 is the total activity with D_2O. Curve No. 2 is the total activity without D_2O. Curve No. 3, showing photo-neutrons alone, is obtained by subtracting No. 2 from No. 1. Curve No. 4, with half-life 41 seconds, is obtained from No. 3 by subtracting the activities due to the 6 longer periods.

neutrons. Under these conditions, decay curves of the gross activity with D_2O in the sphere represent photo-neutrons alone. Figures 4–6 show the gross activity from $t=15$ min. to $t=60$ hr., and the 5 component periods into which the data may be analyzed. The half-lives of these components are 53 hours, 4.4 hours, 1.6 hours, 27 minutes, and 7.7 minutes. The longest period, $\tau_{\frac{1}{2}}=53$ hr., was actually followed somewhat beyond the 60-hr. limit of Fig. 4, but its half-life is considerably less certain than those of the shorter periods.

TABLE II. Photo-neutron yields and periods.

$\tau_{\frac{1}{2}}$ = half-life, τ = mean life.
A = uncorrected photo-neutron yield relative to that of the 22-sec. delayed neutron period.
E_γ = γ-ray energy in Mev, from unpublished work of Hughes, Spatz, and Cahn.
$\frac{1}{F_\gamma}$ = factor to correct yields measured with the 10 in. radius sphere of D_2O to an infinite sphere.
α = correction for γ-ray absorption in the rabbit wall, Al tube, etc.
β = correction for multiple Compton scattering.
$A_s = A\times\alpha\beta/F_t$, yield corrected to infinite volume of D_2O.
$A_d = 100\,A_s/4.54$, percent yield of photo-neutrons relative to the total yield of delayed neutrons.
$A_f = 2\times 0.01\,A_d/100$, absolute yield of photo-neutrons per fission using the value: fast neutrons/fission = 2.
$\frac{1}{F_\gamma}$ = number of γ-ray photons per photo-neutron in an infinite volume of D_2O, assuming each collision reduces energy below threshold.
C = correction factor allowing for photons not reduced below threshold in first impact.
A_γ = absolute number of photons per fission.

Ref. No.	$\tau_{\frac{1}{2}}$	τ	A	E_γ	$\frac{1}{F_\gamma}$	α	β	A_s	% A_d	A_f $\times 10^4$	$1/F_\gamma$	C	A_γ
1	53 hr.	76 hr.	0.00038	(3)	1.69	1.06	1.085	0.00074	0.0163	0.0326	476	1.14	0.0015
2	4.4 hr.	6.3 hr.	.00119	(3)	1.69	1.06	1.085	.00232	.0515	.101	476	1.14	.0042
3	1.65 hr.	2.4 hr.	.0093	2.62	1.62	1.06	1.052	.0168	.370	.742	670	1.09	.045
4	27 min.	39 min.	.0082	2.60	1.63	1.06	1.056	.0149	.328	.656	643	1.09	.038
5	7.7 min.	11 min.	.0124	3.0	1.69	1.06	1.085	.0242	.534	1.065	476	1.14	.046
6	2.4 min.	3.4 min.	.0276	2.65	1.63	1.06	1.054	.0504	1.11	2.23	650	1.09	.132
7	41 sec.	59 sec.	.090	2.25	1.52	1.06	1.01	.147	3.24	6.50	2450	1.01	1.58
8	2.5 sec.	3.6 sec.	.225	3.4	1.77	1.06	1.11	.469	10.31	20.7	389	1.18	.675
									Total→16%	3.2×10^{-3}			2.5

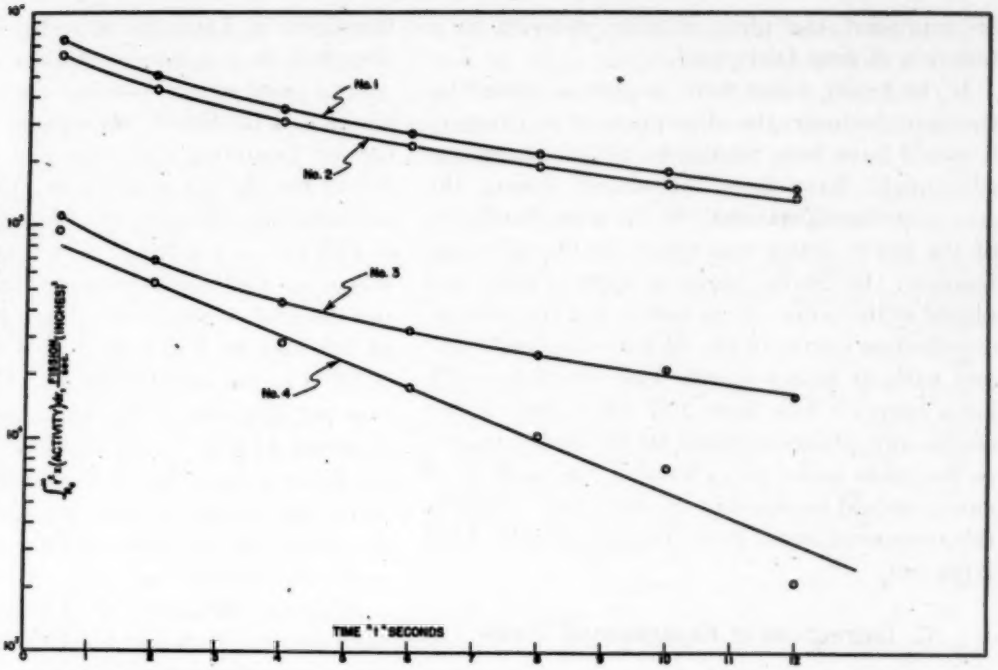

FIG. 9. Thirty-second exposure volume integrals. No. 1 is the total activity with D_2O. No. 2 is the total activity without D_2O. No. 3 is the activity caused by photoneutrons alone. No. 4, showing a half-life of 2.5 seconds is obtained from No. 3 by subtracting the activities due to the 7 longer periods.

Figure 7, curve No. 1, shows the total activity with D_2O following a 3-min. exposure. Curve No. 2 shows the photo-neutron activity alone, after subtracting from No. 1 the contribution of the delayed neutrons, determined with the sphere empty. A formula representing the 5 previously determined photo-neutron periods was fitted to curve No. 2 at $t=53$ min. and then subtracted off, giving curve No. 3. A sixth period is indicated, $\tau_{\frac{1}{2}}=2.4$ min. Extrapolating all yields back to $t=0$ and infinite exposure, the yields of the six photo-neutron periods could then be expressed in terms of the delayed neutron yields. These values are given in Table II.

In Fig. 8, curve No. 1 shows the total activity with D_2O and No. 2 the activity without D_2O, for an exposure of 30 sec. and a 0.15-g sample of enriched material. The delayed neutron curve has been corrected for epicadmium activity, which amounted to about 2 percent. The difference between curves 1 and 2 amounts to only 10 percent of the total activity at $t=30$ sec., so the experimental accuracy in determining the photo-neutron yields for the short periods is considerably less than for the longer periods. After subtracting off the longer periods, a component of half-life 41 sec. is indicated by curve No. 4.

Figure 9 gives the result of a 30-sec. exposure with a 1.5-g sample of unenriched uranium. Here the decay curve is extended back to within 0.5 sec. after the end of the exposure. A period $\tau_{\frac{1}{2}}=2.5$ sec. is found.

B. Estimated Accuracy

The accuracy to be expected in obtaining the area under one of the curves of the type illustrated in Fig. 3 is not better than one percent, owing to statistical probable errors alone. Hence, the yields given in column A, Table II, for the two shortest periods where the photo-neutron activity is of the order of 10 percent of the total are uncertain by about 15 percent. Except for the 53-hr. period, the yields of the longer periods should be considerably more accurate.

The half-life and yield of any short period depends on the previously determined constants of all longer periods, giving a cumulative error. The possibility cannot be ruled out that some of our shorter periods are fictitious, that perhaps some of them cannot be identified with individual fission isotopes. Indeed, the suggestion is made below that the shortest periods given in Table II cannot represent a single isotope but must be due to many half-lives too close together to be resolved. However, the periods and yields given

do represent the photo-neutron activity as a function of time fairly well.

If the heavy water were as pure as stated by the manufacturer, the absorption of neutrons in it would have been negligible. Since contamination might have been introduced during the course of the experiment, the neutron absorption of the heavy water was tested in the following manner: An Sb-Be photo-neutron source was placed at the center of the sphere and the neutron distribution curves in the oil were obtained, with and without heavy water. The γ-rays from Sb have energies less than 2.17 Mev and cannot create any photo-neutrons in the heavy water, so the areas under the (counting rate)$\times R^2$ *vs.* R curves should be equal in the two cases. Actually the areas were found to be the same within about 2 percent.

C. Corrections to Experimental Yields

In Table II, column A represents photo-neutron yields (saturated activities) for our sphere of heavy water relative to the 22-sec. delayed neutron period yield as 1.00. In order to correct these yields to the case of an infinitely large sphere of D_2O and complete γ-ray absorption, it is necessary to know the energy of the γ-rays. Conclusions about the initial energy of the photo-neutrons could not be made from the data of this experiment. The large amount of heavy water moderator slowed the neutrons down to such an extent that the shape of the distribution curve in the oil, where the measurements were taken, was no longer a measure of the initial neutron energy. Hence, we have tried to correlate our periods with those found by W. D. B. Spatz, D. J. Hughes, and A. Cahn in unpublished work on the same subject. Their values for the γ-ray energies are given in column E_γ, Table II. For purposes of calculation we have arbitrarily assumed an energy of 3 Mev for the two longest periods, which were not reported by Spatz, Hughes, and Cahn.

In D_2O and for γ-ray energies between 2 and 5 Mev the photoelectric effect and pair production are negligible in comparison with the Compton effect. If we assume that every Compton scattering of a γ-ray quantum by an electron reduces the quantum energy below the γ,n threshold in D_2O, the fraction of the quanta absorbed in a sphere of radius R cm, from a central point source, is $F_t=1-\exp-[(\mu_s+\mu_\gamma)R]$ where μ_s is the linear "absorption" coefficient per cm for Compton scattering and μ_γ is the coefficient for the γ,n reaction in D_2O. For this experiment the effective thickness of heavy water is 23.3 cm. $\mu_s=\sigma_s\times 3.35\times 10^{23}$ per cm^3 for D_2O, where σ_s, the Compton scattering cross section per electron varies from about 1.27×10^{-25} cm^2 at 2.5 Mev to 1.06×10^{-25} at 3.5 Mev. $\mu_\gamma=6.7\times 10^{22}\times\sigma_\gamma$ per cm^3, where σ_γ, the γ,n cross section per deuteron varies from zero at 2.17 Mev to about 14×10^{-28} cm^2 at 3.5 Mev. In Table II are listed values of $1/F_t$ the correction factor by which the yields A must be multiplied to give the yields for an infinite sphere of D_2O, for the assumed energies E_γ.

A small correction, $\alpha=1.06$, is listed in the next column of Table II. This compensates for the γ-ray absorption in the 0.050-inch wall thickness of the pneumatic tube, the fixed 0.125-inch thick Al tube through the center of the sphere, and in the $\frac{3}{16}$-inch thick wall of the plastic rabbit.

Column β in Table II gives an additional correction necessary because not every Compton scattering process reduces the energy of a γ-ray quantum below the γ,n threshold, so that the flux of γ-rays of energy above the threshold is everywhere higher than that calculated using the full Compton scattering cross section. β/F_t is then the ratio of the number of γ,n neutrons produced by multiple scattered photons in an infinite sphere of D_2O to that produced by multiple scattered photons in a sphere of radius 23.3 cm. The theory of the multiple scattering correction was developed for us by Mr. E. Greuling and Mr. H. Soodak.

Column A_c in Table II is $A\times\alpha\beta/F_t$, the corrected yield of photo-neutrons in an infinite D_2O medium, relative to the yield of the 22-sec. delayed neutron period. $A_d=100\times A_c/4.54$ is the percent yield relative to the total delayed neutrons (see Table I, column A). Column $A_f=2\times 0.01\times A_d/100$ is the absolute yield of photo-neutrons per fission, calculated from the data in column B, Table I, using the arbitrary value 2 for the number of instantaneous neutrons

emitted per fission of a U^{235} nucleus and 0.01 for the ratio[4] of delayed to instantaneous neutrons.

D. Gamma-Ray Yields

We now compute the number of γ-rays per fission necessary to produce the photo-neutrons of each period, with yields A_f in Table II. The fraction of the total γ-ray quanta from a point source which are absorbed in the γ,n reaction in an infinite D_2O sphere is

$$F_\gamma=\mu_\gamma/(\mu_\gamma+\mu_s),$$

provided each scattering process is assumed to reduce the energy below the threshold. If we take into account the fact that some scattered quanta still have energy above the threshold, the actual photo-neutron production will be higher by a factor C, which will be small near the threshold and increase with the initial energy of the γ-ray. In Table II are listed, for each period, the values of $1/F_\gamma$ and of C. The absolute yield of γ-ray quanta per fission, A_γ, will be

$$A_\gamma=A_f/F_\gamma C.$$

V. DISCUSSION OF RESULTS

A. The Effect of Possible Parent-Daughter Contributions

In the analysis of the data as described above it has been assumed that the hard γ-ray emitters are initial fission fragments. The interpretation of the data is made uncertain because of the possibility that the emitter of the photon giving the photo-neutron may be a daughter of the initial fragment. In such cases the data would yield the true period, but the amplitude deduced by extrapolating the decay back to zero time may be in error. If the daughter has a very much longer life than its parent, the error will not be large. If the two have comparable lifetimes the saturated activities given may be a considerable overestimate.

B. Number of Photons per Fission

From the number of photo-neutrons per fission, the number of hard photons per fission was calculated from a consideration of the relative probabilities of Compton and γ,n collisions. The results are given in column A_γ of Table II. The sum of the values in this column is 2.5 photons per fission of energy above 2.17 Mev. The highest single yield is 1.6 for the 41-sec. period. This value, however, is subject to great uncertainty. The assumed energy $E_\gamma=2.25$ Mev is very near the threshold, where the γ,n cross section is small and changing rapidly. If the true energy is only slightly higher, the calculated γ-ray yield A_γ would be much reduced. However, the highest observed yields of individual fission products are only about 6 percent, so the γ-ray yields of the 2.5-sec. 41-sec., and 2.4-min. periods are all much too high to be caused by single isotopes. These high photon yields can be explained by supposing that there are a large number of high energy γ-emitters with half-lives too close together to be resolved in this experiment.

C. Correlation of the Gamma-Ray Periods with Known Fission Products

We have been unable to correlate without ambiguity our periods with those given for the known fission products. It seems that in order to accomplish this correlation it would be necessary to repeat the experiment with individual fission products or with groups of products each containing a small number of members.

[4] H. D. Smyth, *Atomic Energy for Military Purposes* (Princeton University Press, Princeton, 1945), Appendix 3; or Rev. Mod. Phys. 17, 459 (1945).

A Calorimetric Determination of the Energy Produced by Plutonium (239)

J. W. STOUT* AND W. M. JONES
University of California, Los Alamos Scientific Laboratory, Santa Fe, New Mexico

(Received January 6, 1947)

The rate of energy production by alpha-disintegration of plutonium (239) has been measured calorimetrically. The method was to measure the rate of evaporation of liquid nitrogen by a 120-gram sphere of metallic Pu^{239} and compare this rate with that produced by the introduction of electrical energy. The power produced by Pu^{239} is 1.923 ± 0.019 abs. watts·gram^{-1}. Combining this with the energy per alpha-particle determined from range and range-energy measurements, one obtains 2.411×10^4 years as the half-life of Pu^{239} with respect to alpha emission.

THE energy produced by the alpha-particles from plutonium (239) is sufficient to cause a sample of the metal to feel slightly warm to the touch. There was available at the Los Alamos laboratory a very pure sample of Pu^{239} in the form of a 120-gram sphere. The heat generated by this sphere was about 3 calories per minute. This paper describes a calorimetric experiment designed to measure the heat to an accuracy of about 1 percent.

The power generated per atom of Pu^{239} can be combined with the value of the energy per alpha-particle to give the number of alpha-particles per unit time and consequently the half-life of Pu^{239} with respect to alpha-disintegration. In the sample we used, all sources of energy other than the alpha-disintegration were extremely small in comparison with the experimental error. The calorimetric value of the power, the measurements of which are described below, gives an accurate determination of the Pu^{239} half-life which is independent of the methods ordinarily used.

The sphere of Pu^{239} was 2.25 cm o.d. and had a central spherical hole 0.8 cm in diameter. It was made in two hemispheres. The surface, including the hemispherical hole and the equatorial planes, was coated with a 0.0025-inch film of silver. The sphere with silver coating weighed 121.53 grams and contained 120.06 grams of Pu^{239}.

The method adopted was to immerse the sphere in a calorimeter containing liquid nitrogen and measure the rate of evaporation of nitrogen gas due to the heat generated. Calibration experiments were done in which electrical energy was introduced at a rate approximating that of the sphere.

DESCRIPTION OF THE APPARATUS

The calorimeter was a silvered Pyrex glass Dewar vessel. It is shown in Fig. 1. Above the Dewar is a ground glass joint which was sealed with rubber cement diluted with toluene. This type "of seal" has been previously described[1] as suitable for use at low temperature, and we found it satisfactory. In every case the joint was tested and found to be tight after being cooled to liquid-air temperature and before beginning measurements. At the bottom of the calorimeter was an electrical heater, *D*, made of 275 ft. of No. 40 D.S.C. copper wire wound on a cylinder $1\frac{1}{8}$ inches in diameter and $2\frac{3}{4}$ inches high. Two leads of No. 30 copper wire, *C*, were soldered to the inside of the tungsten wires, *B*, sealed through the glass. Attached to the outside of each tungsten wire was a current and potential lead of No. 30 copper wire. These go to the electrical system.

The electrical energy was supplied by lead cells. The current was measured by reading with a 100,000 microvolt Leeds and Northrup White Double Potentiometer and H. S. Galvanometer the potential drop across a calibrated standard one-ohm resistance and the voltage by means of the same potentiometer used with a calibrated volt-box constructed from standard 100 and 10,000-ohm resistances. The accuracy of the electrical measurements is about 0.02 percent, and their contribution to the over-all error of the measurements is negligible. Corrections were made in the usual manner[2] for the energy dissi-

* Present address: Institute for the Study of Metals, University of Chicago, Chicago 37, Illinois.

[1] J. W. Stout and W. F. Giauque, J. Am. Chem. Soc. 63, 714 (1941).

[2] W. F. Giauque and R. Wiebe, J. Am. Chem. Soc. 50, 101 (1928).

pated in the volt-box and in the single leads to the heater.

The sphere was supported in a cylindrical cradle, *E*, $\frac{15}{16}$-inch diameter made of brass foil and closed at the bottom with a copper screen. The cradle containing the two hemispheres, *F*, each with its equatorial plane upwards, was lowered to the bottom of the calorimeter, and later removed, with a heavy thread, *G*. Since the measurements are made at constant temperature, the heat capacities of the sphere and cradle which are, of course, not present during the calibration runs, do not introduce any error.

The calorimeter was suspended by metal supports inside a large glass Dewar vessel $5\frac{1}{4}$ inches i.d. and 54 inches long. A glass filling tube, 0.6 cm i.d., extended through the closure of the Dewar vessel and connected the top of the calorimeter to stopcocks for evacuation, filling with nitrogen, and metering of the nitrogen evaporated. The tube was bent in a spiral a few inches above the calorimeter in order to intercept room temperature radiation. The large Dewar vessel was filled with liquid nitrogen-oxygen mixture of such composition as to be 2° to 5°K warmer than the calorimeter.

In making a measurement, the calorimeter was assembled (with or without the sphere), and the large Dewar containing liquid nitrogen-oxygen mixture was slowly raised in place. More liquid nitrogen was added to the large Dewar through a tube in the top closure so as to bring the liquid level well above the bend in the glass tube. The large Dewar was then evacuated until the temperature of the liquid in it fell below the boiling point of nitrogen at local atmospheric pressure. Meanwhile, the calorimeter was evacuated and flushed with dry nitrogen from a cylinder. All nitrogen condensed in the calorimeter was from this cylinder, which contained 99.8 percent pure N_2. It was dried by passing through two drying tubes filled with magnesium perchlorate and then went through a gas meter. The nitrogen passed through the meter at atmospheric pressure and then was condensed in the glass filling tube, from which the liquid fell into the calorimeter. About two hours were required to condense 110 cc of liquid nitrogen in the Dewar during the sphere measurements. When sufficient liquid was condensed in the calorimeter, dry air, nitrogen or oxygen was bubbled through a tube which extended to the bottom of the large Dewar vessel, until the liquid in this vessel was at its boiling point and uniform in temperature throughout. The rate of evaporation of nitrogen from the calorimeter due to the heat of the sphere or to electrical energy was measured with a second gas meter. A period of several hours after condensing the nitrogen was allowed in order for the thermal system to come to equilibrium. Since all gas entering or leaving the calorimeter was measured, the amount of liquid nitrogen in the calorimeter was known at all times.

The temperature of the bath was measured with three copper-constantan thermocouples attached to the outside of the calorimeter at points marked *H* in Fig. 1. They were read on the White potentiometer with an accuracy of about 0.1°K. The thermocouples were calibrated in a bath of liquid oxygen. The temperature of the liquid in the calorimeter was calculated from its pressure and the vapor pressure equation of Giauque and Clayton.[3]

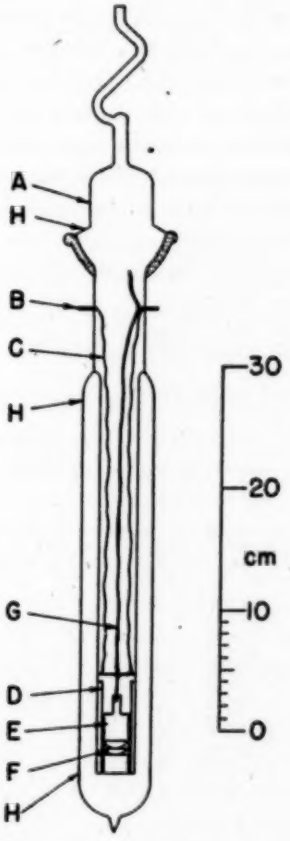

FIG. 1. Calorimeter.

[3] W. F. Giauque and J. O. Clayton, J. Am. Chem. Soc. 55, 4875 (1933).

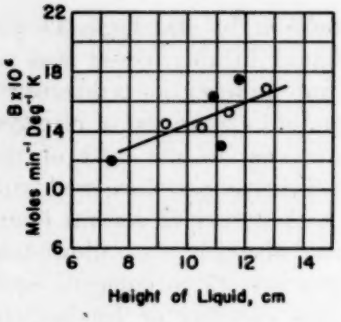

FIG. 2. Coefficient of heat leak.

The meters used were Precision wet test meters, which had been filled with butyl phthalate to eliminate the need for correcting for the vapor pressure of the sealing fluid. The meter hand made one revolution for every 0.1 cubic foot of gas. The time for a complete revolution was measured with a calibrated stopwatch. If care is taken to time only complete revolutions, the meter is reproducible to about ±0.5 percent. In the sphere measurements about 36 minutes were required for one revolution of the meter hand (0.1 cubic foot).

The temperature of the gas entering the meter was measured with a mercury thermometer, and the pressure was calculated from the barometric pressure combined with the pressure of a butyl phthalate manometer which measured the pressure difference between the gas entering the meter and the atmosphere. All pressure readings have been converted to international centimeters of mercury, using 979.1 cm sec.$^{-2}$ as the local acceleration of gravity and 980.665 cm sec.$^{-2}$ as the standard acceleration.

HEAT LEAK CALIBRATIONS

Measurements were made of the rate of evolution of nitrogen when no heat other than that due to heat leak was being introduced into the calorimeter. These measurements extended throughout the period of calibration and sphere runs and show no significant change with time. At first the gas evolved was measured with the meter, but since the rate was only a few percent of that during the calibration or sphere runs, the accuracy was not great. Later the rate of gas evolution during heat leak measurements was determined by allowing the gas to collect in an evacuated rubber prophylactic sack. The volume of gas was then determined by measuring with a buret the equivalent volume of water.

The heat leak was found to be a function of the height of liquid in the calorimeter. Most of the leak is due to conduction by residual gas across the evacuated space between the walls of the calorimeter Dewar. Measurements were made at different temperature differences between bath and calorimeter and at different heights of liquid in the calorimeter so as to cover the range in the calibration and sphere experiments. It was found that the heat leak obeyed Newton's law,

$$dn/dt = B(T_{\text{bath}} - T_{\text{calorimeter}}),$$

where dn/dt is moles·min.$^{-1}$ of nitrogen evaporated; B is coefficient of heat leak, moles·min.$^{-1}$·deg.$^{-1}$°K; T is temperature in °K. The values of B are plotted as a function of height of liquid in Fig. 2. This curve was used in calculating the calibration and sphere measurements. Points indicated by open circles were taken with the rubber sack and are given more weight than those indicated by filled circles which were measured with the gas meter.

TABLE I. Electrical calibration measurements.

No.	Duration of observations, min.	Electrical power, int. watts	Average pressure of nitrogen, int. cm mercury	Average temp. of nitrogen, at meter, °K	Obs. flow of nitrogen, moles min.$^{-1}$ ×10^3	$T_{\text{bath}} - T_{\text{cal.}}$, °K	Av. ht. of liquid, cm	Heat leak correction, moles min.$^{-1}$ ×10^3	Corrected rate of evolution of nitrogen moles min.$^{-1}$ ×10^3	Heat to vaporize nitrogen, int. joules mole^{-1}
1	80	0.19891	576.5	296.3	2.186	4.41	11.06	0.067	2.119	5632
2	86	0.22672	576.7	295.2	2.487	4.51	10.09	0.065	2.422	5617
3	45	0.24869	577.3	294.7	2.722	4.51	9.44	0.063	2.659	5612
4	67	0.27878	577.6	293.8	3.053	4.55	8.70	0.061	2.992	5591
5	139	0.23540	579.8	295.9	2.552	2.26	12.91	0.038	2.514	5618
6	86	0.23898	575.9	295.4	2.574	5.48	9.35	0.076	2.498	5740
7	70	0.23188	575.6	295.5	2.501	5.43	8.59	0.073	2.428	5730
8	116	0.25239	582.0	291.5	2.770	2.39	13.86	0.042	2.727	5553
9	107	0.24248	582.7	293.5	2.653	2.51	10.97	0.038	2.615	5564
									Mean	5629±40 (av. dev.)

TABLE II. Measurements of heat evolved by Pu^{239} sphere.

No.	Duration of observations, min.	Average pressure of nitrogen, int. cm mercury	Average temp. of nitrogen at meter, °K	Obs. flow of nitrogen, moles min.$^{-1}$ $\times 10^3$	$T_{bath} - T_{cal.}$, °K	Av. ht. of liquid, cm	Heat leak correction, moles min.$^{-1}$ $\times 10^3$	Corrected rate of evolution of nitrogen moles min.$^{-1}$ $\times 10^3$	Heat to vaporize nitrogen int. joules mole^{-1}	Heat evolved by sphere, int. watts
1	144	584.7	294.9	2.501	2.01	11.47	0.031	2.470	5629	0.2317
2	250	585.3	294.8	2.515	5.16	9.08	0.070	2.445	5629	0.2294
3	216	584.5	294.4	2.511	2.93	11.18	0.044	2.467	5629	0.2314
									Mean	0.2308±0.0010 (av. dev.)

CALIBRATION MEASUREMENTS

The data for the electrical calibration measurements are given in Table I. These measurements were taken both before and after those on the sphere. The agreement is good except for runs No. 6 and 7 which are unaccountably high. Since we have not been able to find any error in these two measurements, they have been included in the average. The top of the heating coil was 7.2 cm above the bottom of the Dewar so it was always covered with liquid.

The average value of the heat to vaporize nitrogen is 5629±48 (av. dev. from mean) int. joules·mole^{-1} or 1346±11 cal.·mole^{-1}. (One cal. =4.1833 int. joules.) It is interesting to compare this with the more accurate heat of vaporization of nitrogen measured by Giauque and Clayton.[3] They obtained 1332.9±1.0 cal.·mole^{-1} at the normal boiling point, 77.32°K. Taking $\Delta C_p = 6.6$ cal.·mole^{-1} one obtains for the heat of vaporization of nitrogen at 75.17°K, the temperature corresponding to our measurements, the value 1347.1±1.0 cal.·mole^{-1}. The agreement of our value with this is evidence that there are no large undetected errors in our measurements.

THE HEAT PRODUCED BY THE Pu^{239} SPHERE

The data on the runs with the Pu^{239} sphere are given in Table II. The height of the topmost portion of the sphere was about 3.8 cm; so it was well covered with liquid at all times. The average value of the heat produced is 0.2308 int. watt or 3.310 cal.·min.$^{-1}$. It is believed that this value is correct to within ±1 percent.

THE HALF-LIFE OF Pu^{239} WITH RESPECT TO ALPHA-DISINTEGRATION

The weight of Pu^{239} in the sphere was 120.06 g. The atomic weight of Pu^{239} is taken as 239.08. Other physical constants are from Birge's 1941 tables.[4] The energy given out by Pu^{239} is, therefore, $(0.2308\times1.00020)/120.06 = 1.923\times10^{-3}$ abs. joule·sec.$^{-1}$·gram^{-1}, or 7.633×10^{-18} erg·sec.$^{-1}$·atom^{-1}. Possible sources of energy due to other nuclear reactions and to impurities have been considered. These are small in comparison with the experimental error of our measurements, and may be neglected.

The range of Pu^{239} alpha-particles has been measured by Chamberlain, Gofman, Segrè, and Wahl[5] as 3.675 cm relative to polonium as 3.842 cm. Taking the energy of the polonium alpha-particles (5.2984 Mev) and the range-energy relationship from the paper of Holloway and Livingston[6] one obtains 5.144 Mev as the energy of the plutonium alpha-particle. The recoil of the residual nucleus contributes 0.086 Mev so the total energy per alpha-disintegration of Pu^{239} is 5.23 Mev or 8.38×10^{-6} erg·atom^{-1}.

The half life of Pu^{239} for alpha-emission is then

$$T_{\frac{1}{2}} = (0.69315\times8.38\times10^{-6})/(7.633\times10^{-18}\times3.15569\times10^{7}) = 2.411\times10^{4} \text{ years.}$$

We wish to thank Professor E. Segrè for many helpful discussions about this problem.

This paper is based on work performed under Contract No. W-7405-Eng-36 with the Manhattan Project at the Los Alamos Scientific Laboratory of the University of California. The information contained in it will appear in Division V of the Manhattan Project Technical Series as part of the contribution of the Los Alamos Laboratory.

[4] R. T. Birge, Rev. Mod. Phys. **13**, 233 (1941).
[5] Chamberlain, Gofman, Segrè, and Wahl, Phys. Rev. **71**, 529 (1947).
[6] Holloway and Livingston, Phys. Rev. **54**, 18 (1938).

Radioactivity of Be^{10}†

J. LEVINGER* AND E. MEINERS**
Metallurgical Laboratory, University of Chicago, Chicago, Illinois
(Received January 2, 1947)

From the beta-activity induced in beryllium by (1) fast deuteron bombardment, and (2) slow neutron capture, the half-life of Be^{10} is determined. The value is between 10^6 and 10^7 years. The beta-end-point is roughly 650 kev, and no gammas were observed. These results confirm those of McMillan and Ruben. The $B^{10}(n,p)Be^{10}$ cross section for thermal neutrons is computed by comparison with the known value for $B^{10}(n,\alpha)Li^7$, assuming disintegration to the ground state possible for the former reaction.

INTRODUCTION

McMILLAN and Ruben[1] have recently published measurements made in 1940 on the half-life and beta-end-point of a long-lived beryllium activity. A mass-spectroscopic separation by Pierce and Brown[2] has established that the active isotope has mass 10. In 1944 we measured the activity produced by Be^9 (d,p) and (n,γ) reactions; and from these yields estimated the Be^{10} half-life. We have also measured the beta end-point, and studied the gamma-activity. These measurements are not as complete as we would like, owing to our transfers to other sections of the Manhattan Project.

CHEMICAL SEPARATIONS

Our strongest sample of Be^{10} came from the thick beryllium target of the Washington University cyclotron, which had been activated by about 600,000-microampere hours bombardment by 10.45-Mev deuterons.[3] The target was etched to the calculated depth of deuteron penetration, giving us 1.7 grams of beryllium. The beryllium was purified by a chemical procedure similar to that used by McMillan and Ruben. The initial separation consisted of a chloroform extraction of beryllium basic acetate, and purification by precipitation of the copper group of sulphides. Six different samples were then prepared for counting the beta-activity, using different additional purifications in preparing each sample, as follows: (1) five beryllium hydroxide precipitations, and precipitation of the zinc group of sulphides, to remove contaminants; (2) one beryllium hydroxide precipitation; (3) three beryllium hydroxide precipitations; (4) two beryllium hydroxide precipitations, and an incomplete berryllium ammonium phosphate precipitation; (5) a beryllium ammonium phosphate precipitation of the material not precipitated in the previous procedure; and (6) a chloroform extraction of beryllium basic acetate. The average specific activity of these 6 samples was measured on a GM tube as 17.5 ± 1 betas/sec. mg of beryllium. This small difference among the six samples established that the activity was beryllium.

HALF-LIFE OF Be^{10}

Let Y' be the d-p yield for a thick beryllium target activated by 10.45-Mev deuterons. The total deuteron flux was 1.3×10^{22}. From the specific activity given above, the activity produced in the whole target is calculated as 29,000 betas/sec. This figure is certainly low, as we know that much of the beryllium was sputtered off the target during the bombardment.[4] The upper limit on the Be^{10} half-life is then

$$T_{\frac{1}{2}}\leqq\frac{1.3\times10^{22}\times0.693\,Y'}{29{,}000\times3.16\times10^{7}}=1.0\times10^{10}\,Y'\text{ years.}$$

† This document is based on work performed under Contract No. W-7401-eng-37 for the Manhattan Project and the information covered in this document will appear in Division IV of the Manhattan Project Technical Series, as part of the contribution of the Argonne National Laboratory.

* Now at Cornell University, Ithaca, New York.

** Now at Washington University, St. Louis, Missouri.

[1] E. M. McMillan and S. Ruben, Phys. Rev. **70**, 123 (1946).

[2] A. K. Pierce and F. F. Brown, III, Phys. Rev. **70**, 779 (1946).

[3] Based on a recent measurement of the deuteron energy by Kurie.

[4] This spalling off of active material has recently been confirmed by measurements of E. M. McMillan on the other Washington University target (private communication).

McMillan and Ruben measured the Be^{10} activity produced by 12,000-microampere hours bombardment of beryllium by 16-Mev deuterons. They give the half-life as $6.4\times10^{8}Y$ years, where Y is the d-p yield for 16-Mev deuterons. For comparison with their results, we may estimate Y/Y' from the ratio of the deuteron ranges as about 2. Then our measurement gives a half-life eight times the McMillan and Ruben determination; but, as already pointed out, our results can only be considered as an upper limit.

Assuming that the d-p cross section for high energy deuterons is somewhat less than half the geometrical cross section, and that the effective nuclear radius is about 5×10^{-13} cm, we calculate a d-p cross section of 0.3 barn (+0.3 b., −0.15 b.). This agrees in order of magnitude with the cross section as estimated from the thick target d-n yield for 1-Mev deuterons.[5] By use of this cross section, Y' is calculated as one nucleus of Be^{10} formed per 1000 deuterons, and Y as 1/500. The Be^{10} half-life from our results is estimated as less than 10^{7} years; and from McMillan and Ruben's measurements as about 1.3×10^{6} years.

Since the beryllium cross section for capture of slow neutrons is known,[6] the Be^{10} half-life can be determined from the specific activity induced in beryllium by a known neutron activation. Beryllium metal was activated in the Clinton pile for several months. After chemical separations similar to those given above for purification of the Washington University cyclotron target, the beta-activity was only 10 counts/min. We are uncertain whether this low activity is due to contamination, or to Be^{10}. The upper limit for the specific activity due to Be^{10} is taken as 0.02 beta/sec. mg of beryllium; and the Be^{10} half-life is calculated as greater than 10^{6} years. This value is in fortuitously good agreement with our calculation from McMillan and Ruben's measurements; and is consistent with the upper limit on the half-life set by our measurement of the d-p yield.

β AND γ ACTIVITY

Deflection of the particles by a small electromagnet placed between the active beryllium from the cyclotron target and the GM tube showed that the particles were negatrons. Absorption measurements in aluminum from 0.2 to 300 mg/cm² were made for both a thin and a thick source. The thin source gave an inspection end-point of roughly 200 mg/cm²; and an end-point from Feather analysis of 225 mg/cm², or 650 kev. Owing to the low beta-intensity and high gamma-background, the Feather analysis was carried only to 0.6 of the range, and the extrapolated range is therefore inaccurate. The inspection end-point for the thick source was 200 ± 20 mg/cm². These measurements are in fair agreement with the end-point of 180 ± 20 mg/cm², or 550 kev, given by McMillan and Ruben. Both measurements are consistent with the $Be^{10}-B^{10}$ mass difference of 550 ± 110 kev.[7]

Initially a gamma-ray of intensity roughly 4 quanta/beta was observed in the active material, and chemically determined to be a beryllium activity. The half-life from decay measurements, and energy from lead absorption for this gamma-activity were both in good agreement with the known values for Be^{7}. No gamma-activity due to Be^{10} was observed, in agreement with the results of McMillan and Ruben.

PRODUCTION OF Be^{10}

Samples with higher specific activity of Be^{10} might be produced by a $Li^{7}(\alpha,p)Be^{10}$ reaction using cyclotron alphas; by a $C^{13}(n,\alpha)Be^{10}$ reaction with fast neutrons (since this reaction is endothermic by about 3.5 Mev); or by a $B^{10}(n,p)Be^{10}$ reaction in a chain-reacting pile. Bretscher[8] was unable to find Be^{10} activity produced by this last reaction, using deuterons on lithium as a neutron source. He sets the upper limit for the fast neutron cross section for this reaction as $5\times10^{-7}T_{\frac{1}{2}}$ barn, where $T_{\frac{1}{2}}$ is the Be^{10} half-life in years. Using our estimated half-life of 2×10^{6} years, this sets the upper limit on the cross section as 1 barn. Cross sections which are thousands of times smaller than this can be measured using the high neutron fluxes now available. For sufficiently high neutron energies we would expect the $B^{10}(n,p)Be^{10}$ cross section to be of the same

[5] H. A. Bethe and M. S. Livingston, Rev. Mod. Phys. 9, 330 (1937).
[6] M. Goldhaber, Phys. Rev. 70, 85 (1946); and work at the Metallurgical Laboratory, to be published in the Plutonium Project Reports.
[7] B. J. Isaacs, Cornell Thesis, "A Revision of the Isotopic Mass Scale, (1942)"; H. A. Bethe and M. S. Livingston, Rev. Mod. Phys. 9, 245 (1937); and E. Pollard, Phys. Rev. 57, 241 (1941).
[8] E. Bretscher, Nature 146, 94 (1940).

TABLE I. Comparative data on $B^{10}(n,p)Be^{10}$ and $B^{10}(n,\alpha)Li^7$ reactions.

Measurements	$B^{10}(n,p)Be^{10}$ McMillan and Ruben[a]	$B^{10}(n,p)Be^{10}$ This paper	$B^{10}(n,\alpha)Li^7$
beta-end-point Be^{10}	550 kev	650 kev	——
reaction energy	230 kev	130 kev	2500 kev
Coulomb barrier	1850 kev	1850 kev	3700 kev
penetration factor	5×10^{-3}	3×10^{-4}	0.45
cross section (thermal neutrons)	8 barns	0.5 barn	700 barns

[a] Reference 1.

order of magnitude as the $N^{14}(n,p)C^{14}$ cross section, which is about 0.01 barn.[9]

The beta-decay theory[10] predicts a large spin for Be^{10}; while we would expect a spin of zero, since this is an even-even nucleus. Measurements of the ratio of the $B^{10}(n,p)Be^{10}$ and $B^{10}(n,\alpha)Li^7$ cross sections, especially for slow neutrons, might be of interest in establishing selection rules, leading to some knowledge of the spin of the ground state of Be^{10}. Comparison of the (n,p) cross section for thermal neutrons with that for fast neutrons might well be made by comparing the beryllium activity at the surface of a boron lump activated in a pile, with the beryllium activity in the inside of the lump.

[9] H. H. Barschall and M. E. Battat, Phys. Rev. **70**, 245 (1946).
[10] E. J. Konopinski, Rev. Mod. Phys. **15**, 222 (1943).

For thermal neutrons we may estimate the $B^{10}(n,p)Be^{10}$ cross section by comparing the penetration probability for the protons to escape through the Coulomb barrier, with the penetration factor for the much more energetic alpha-particles emitted in the competing $B^{10}(n,\alpha)Li^7$ disintegration, of known cross section.[11] We assume here that the compound nucleus is permitted to disintegrate to the ground state of Be^{10}; while the (n,α) reaction goes to a level of Li^7 about 0.5 Mev above ground.[12] Penetrations are calculated using the Gamow theory.[13]

Table I shows that in the absence of selection rules the $B^{10}(n,p)Be^{10}$ reaction could be observed by the beryllium activity produced by activation of boron by thermal neutrons in a pile; and that the cross section for this reaction is sensitive to the beta-end-point of Be^{10}.

ACKNOWLEDGMENT

The authors gratefully acknowledge their indebtedness to A. H. Snell for his help in guiding these experiments; and to H. A. Bethe and E. M. McMillan for helpful discussions on this problem.

[11] R. F. Bacher, C. P. Baker, and B. D. McDaniel, Phys. Rev. **69**, 443 (1946); James Rainwater and William W. Havens, Jr., Phys. Rev. **70**, 136 (1946).
[12] H. A. Bethe and M. S. Livingston, Rev. Mod. Phys. **9**, 340 (1937).
[13] H. A. Bethe, Rev. Mod. Phys. **9**, 166 (1937); using nuclear radius of $1.5\times10^{-13}A^{\frac{1}{3}}$ cm.

The Transmission of Slow Neutrons through Microcrystalline Materials*

E. FERMI,** W. J. STURM, AND R. G. SACHS
Argonne National Laboratory, Chicago, Illinois
(Received January 27, 1947)

The transmission of monochromatic slow neutrons through microcrystalline Be and BeO has been determined. The source of neutrons was the Argonne heavy water pile. These neutrons were monocromatized by means of a mechanical velocity selector for low energies and a neutron crystal spectrometer for higher energies. The results are in excellent agreement with the theory of elastic scattering from crystals. It is found by comparison of the results on BeO with the theory that the scattering amplitudes of Be and O have the same sign. This method may be used to determine the relative scattering phases of other pairs of nuclei which can be combined to form a crystalline material. The sample must consist of crystals smaller than a micron in linear dimensions. Other possible sources of disagreement between theory and experiment are discussed in Section 5.

1. INTRODUCTION

THE measurement of the effective scattering cross section of crystalline materials for slow neutrons is of considerable interest in connection with problems of neutron diffusion. If the material consists of nuclei having a small absorption cross section, the scattering cross section can be determined by measuring the transmission coefficient for slow neutrons. It is known that the scattering cross section determined in this way is a very sensitive function of neutron energy which shows violent fluctuations for small changes in the energy. These fluctuations are associated with the appearance of Bragg reflections from the appropriate planes in those of the microcrystals which are properly oriented. The shape of the transmission curve has been determined theoretically by Halpern, Hammermesh, and Johnson[1] and by Weinstock[2] for materials containing one atomic species. The generalization to multi-atomic materials is simple and will be given in Section 4.

With the intense monochromatic neutron sources which are now available, it is possible to obtain a rather precise measurement of transmission curves as a function of energy. Measurements of this kind have been carried out for microcrystalline Be and BeO. It is the purpose of this paper to present the results of these measurements and to compare them with theory. In particular, it will be shown in Section 4 how the results can be used to determine the relative phases of the Be and O scattering.

In Section 2, the experimental methods for obtaining monochromatic neutron beams are discussed and in Section 3 the experimental results obtained with these beams are given. Section 4 contains a discussion of the theory with particular reference to its application to materials containing more than one atomic species. The limits of applicability of the theory are considered in Section 5.

2. EXPERIMENTAL METHOD

The monoenergetic neutron beams required for the measurements were obtained by means of two velocity selectors in conjunction with the heavy water pile at the Argonne Laboratory. The first was the mechanical velocity selector first used by Fermi, Marshall, and Marshall as modified by Brill and Lichtenberger,[3] which by use of a motor driven cadmium shutter and proper timing devices can be applied to the measurement of cross sections for the range of neutron energies between 0.004 and 0.20 electron volt. The second, which extended the measurements in one case to about 1.0 electron volt,

* This document is based on work performed under the auspices of the Manhattan Project at the Argonne National Laboratory, This paper was submitted for declassification on November 27, 1946.
** Also a member of the Institute for Nuclear Studies, University of Chicago.
[1] O. Halpern, M. Hammermesh, and M. H. Johnson, Phys. Rev. 59, 981 (1941).
[2] R. Weinstock, Phys. Rev. 65, 1 (1944).
[3] This velocity selector will be described in forthcoming papers by E. Fermi, L. W. Marshall, and J. Marshall and by T. Brill and H. D. Lichtenberger. This description of a use of the instrument before publication of their papers is presented with the permission of these authors.

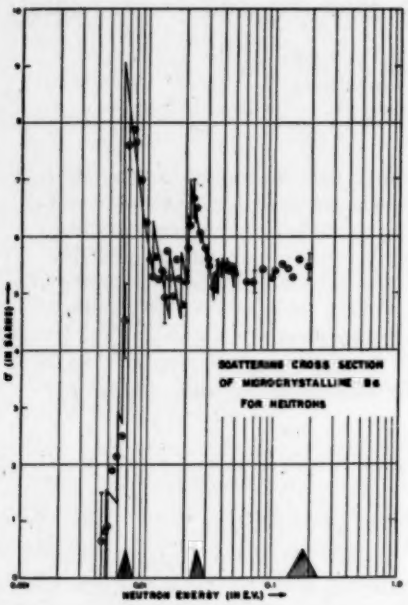

FIG. 1. The microcrystalline beryllium cross section. The solid line represents the cross-section function as calculated in Section 4. Triangles at the base of the curve indicate the resolution of the instrument in the various ranges of measurement. The cross sections, σ, are given in units of 10^{-24} cm^2/atom (barns).

made use of the monoenergetic beams of neutrons diffracted from LiF(100) in the neutron crystal spectrometer which has been previously described.[4]

The bursts of neutrons periodically released by the rotating shutter of the mechanical velocity selector passed through a neutron detector after traversing a measured path between the shutter and detector. The output of the detector, recorded during short measured intervals after the release of the initial burst and during the time the burst was passing through the counter, made it possible to record only neutrons in a very small velocity range. By introducing a sample of a microcrystalline substance into the periodic beam released by the shutter, it was possible to measure the transmission of the substance as a function of energy by measuring the fraction of neutrons scattered by the sample in each small energy interval. The value of the effective scattering cross section was calculated for this interval from the measured transmission data.

[4] W. J. Sturm and S. H. Turkel, Phys. Rev. **70**, 103 (1946); W. H. Zinn, Phys. Rev. **70**, 102 (1946).

The neutron source was a beam from the graphite thermal column of the chain reactor collimated by a series of three absorbing slits to a $\frac{3}{4}''\times 3''$ area. The spectrum of neutrons emitted from this source had an approximate Maxwellian distribution of velocities with its peak at about 0.04 electron volt. The intensities in the range between 0.004 to 0.20 electron volt were sufficient for these measurements; outside this range intensities were generally too low to be used. Passing through the shutter the interrupted beam fell upon the absorber and reached the detector, 150 cm from the rotating cylinder. The detector, mounted with its axis normal to the beam, was a BF_3 proportional counter, 3.8 cm in diameter and 11 cm long, having a central wire 0.002 inch in diameter. The filling gas was enriched in the isotope B^{10} to increase its counting efficiency. In order to minimize the effect of background neutron radiation, the whole counter except for a port to admit the beam was surrounded by a 2.5-cm shield layer of boron carbide.

Measurement of transmission was made by comparing the beam intensity at the various energies with the scattering sample interposed in the beam to the intensity of the unfiltered beam. A second series of similar measurements was taken at each energy to evaluate the intensity of neutrons leaking through the shield plus those fast neutrons which passed through the closed shutter. This measurement was made by stopping the shutter and setting it at the position which it assumed at the time the signal from the detector was sent to the recorders. In this position only fast neutrons could pass through the shutter to reach the detector. In all cases this background intensity was less than 5 percent of the total flux in each energy interval, reaching this fraction only in the extremes of the energy range. The transmission was then calculated from the relation

$$T=R(a)/R(0),$$

where $R(a)$ is the counting rate in the filtered beam corrected for background, and $R(0)$ is the counting rate of the open beam similarly corrected.

3. RESULTS

A. Beryllium

The sample for the measurements was prepared from a block of very pure microcrystalline beryllium metal reduced to chips by turning on a lathe. These chips, subsequently further pulverized by trituration in a mortar and pestle made of beryllium metal, were reduced to their final size in a beryllium ball mill. A 3.25″ diameter cylindrical disk of the material having a surface density of 2.45 grams/square centimeter was prepared by pressing in a die. The cross section per atom shown plotted in Fig. 1 was calculated from the relation

$$\sigma = -\ln T/N$$

in which N is the number of atoms of Be per cm² and T is the transmission measured in the manner discussed above. Solid lines represent theoretically predicted values. Uncertainties in the cross section were evaluated by assigning a statistical uncertainty equal to the square root of the number of counts to each of the four measured components of the transmission value. Because the intensities were lowest at the extremes of the energy range, cross-section measurements at these energies show the greatest statistical uncertainty.

B. Beryllium Oxide

A sintered block of BeO, prepared from very fine powder crystals was used to measure the scattering cross section for this compound. Cross-section values were calculated from transmission measurements and, as can be seen from Fig. 2, agree very well with the theoretical treatment given below.

In the case of the beryllium oxide curve, mechanical velocity selector measurements were repeated on the neutron crystal spectrometer in the range between 0.04 and 0.20 electron volt and extended to 1.0 electron volts by this method.

4. THEORY

Although the theory of the coherent scattering of neutrons by microcrystalline materials has been given,[1,2] it seems worth while to indicate the physical factors which go into the results. For this purpose, we consider a beam of neutrons moving in a given direction incident upon a single microcrystal. The wave-lengths of the neutrons in the beam are assumed to be distributed uniformly between λ and $\lambda+\Delta\lambda$. The orientation of the microcrystal is such that one of the wave-lengths in the interval $\Delta\lambda$ undergoes Bragg reflection from some particular set of lattice planes. Then, since the scattered wave is undergoing constructive interference, the scattered intensity is proportional to the square of the number of scattering centers. Thus, if N_0 is the number of nuclei in the microcrystal and F the scattering cross section of a nucleus, the scattered intensity is proportional to N_0^2F.

Since the crystal is finite in size, the scattered beam is spread by diffraction over a solid angle of the order of $(\lambda/l)^2/\cos\theta$ where l is the average linear dimension of a microcrystal and θ is the angle between the scattered beam and the

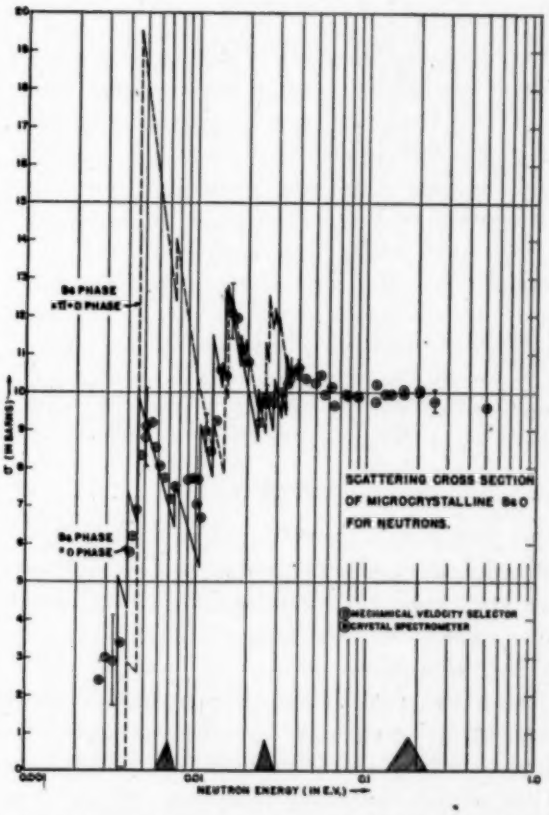

FIG. 2. Scattering cross section of BeO. Alternate theoretical curves for same and opposite phase of neutron scattering are shown as solid and dotted lines, respectively. Results indicate that the Be phase is the same as the oxygen phase.

normal to the crystal plane responsible for Bragg reflection. Since $\cos\theta = b\lambda/2$ where b is the product of the order of the reflection and the reciprocal of the spacing between lattice planes, the intensity of the scattered beam integrated over its spatial width is proportional to

$$\lambda N_0^2 F/l^2 b. \quad (1)$$

Only neutrons within a small range of wave-lengths in the interval $\Delta\lambda$ contribute to this scattering. The fraction of the neutrons with the proper wave-length can be obtained from the resolving power of the crystal which is $d\lambda/\lambda = 1/bl$ where bl is equal to the product of the order of the reflection and the number of crystal planes contributing to the reflection. The fraction of the incident neutrons which are scattered is therefore $d\lambda/\Delta\lambda = \lambda/bl\Delta\lambda$, so the ratio of the intensity scattered to the incident intensity is proportional to

$$N_0^2 F\lambda^2/l^3 b^2 \Delta\lambda. \quad (2)$$

This scattered intensity is now to be averaged over all orientations of the microcrystal. Since the crystal gives rise to a Bragg reflection only if its orientation is such that the Bragg condition is satisfied for some wave-length within $\Delta\lambda$, a contribution to the scattering is obtained only in the solid angle $2\pi\Delta(\cos\theta) = 2\pi b\Delta\lambda/2$. The average over-all orientations, therefore, gives rise to the factor $\Delta(\cos\theta)/2 = b\Delta\lambda/4$. The final result for the scattering cross section per nucleus corresponding to scattering of a particular order from a particular set of lattice planes is, apart from numerical factors,

$$\sigma_b = NF\lambda^2/b, \quad (3)$$

where N is the number of nuclei per unit volume. This cross section is to be summed over all sets of crystal planes and all orders of reflection which are consistent with the Bragg condition; i.e., for which $b \leq 2/\lambda$.

From this result it can be seen that for very low neutron energies of wave-length large compared to twice the spacing between any adjacent lattice planes, no Bragg reflection can occur so there is no coherent scattering. When the energy is increased to the point at which the Bragg condition is just satisfied for the most widely spaced pair of lattice planes, there is a discontinuous jump in the scattering given by Eq. (3). Then the cross section decreases proportionally to the square of the neutron wave-length until the Bragg condition is satisfied for the next most widely spaced pair of lattice planes. At that point, another term of the type Eq. (3) is introduced so the cross section again increases discontinuously. This behavior repeats itself as the energy is increased so a jagged curve of the form shown in Fig. 1 is obtained.

The exact form of the elastic scattering cross section with the correct numerical factors including a factor which takes into account the zero point and thermal oscillations of the crystal is[2]

$$\sigma_e = \sum_{b \leq 2/\lambda} FN\lambda^2 \exp(-\omega b^2)/8\pi b, \quad (4)$$

where ω is a constant which depends on the Debye temperature and temperature of the lattice and is to be obtained from reference 2, Eq. (30). F is to be interpreted as the form factor of the unit cell in the crystal and N the number of unit cells per unit volume. Then σ_e is the cross section per unit cell.

Since the Be lattice is hexagonal close packed, the form factor is given by

$$F_{\mathrm{Be}} = 2\sigma_{\mathrm{Be}}[1+\cos\pi(2l+4m+3n)/3]/\mu_{\mathrm{Be}}^2, \quad (5)$$

where σ_{Be} is the cross section of the free Be atom, μ_{Be} is the reduced mass, in units of the neutron mass, of the neutron and a free Be atom, and l, m, n are the products of the order of the reflection and the Miller indices of the plane leading to the particular Bragg reflection under consideration. The appearance of the factor $1/\mu_{\mathrm{Be}}^2$ is owing to the very large effective mass of a Be atom which scatters neutrons with an energy small compared to the binding of the Be in the lattice.[5] The theoretical curve obtained from Eq. (4) for Be at room temperature ($T = 293°\mathrm{K}$) is given in Fig. 2. The cross section σ_{Be} has been taken to be 6.1×10^{-24} cm^2. This value is obtained from the mean experimental cross section for a neutron energy of the order of several volts (an energy at which the Be atom may be treated as free). The Debye temperature of Be has been taken to be[6] $\Theta = 1000°\mathrm{K}$.

[5] E. Fermi, Ricerca Scient. **7**, No. 2, 13 (1936). See also R. G. Sachs and E. Teller, Phys. Rev. **60**, 18 (1941).

[6] Mott and Jones, *Properties of Metals and Alloys* (Oxford, 1936).

The generalization of these considerations to polyatomic crystals leads again to Eq. (4). In this case, however, the form factor depends on the positions of the different atomic species in the unit cell and on the relative signs of the amplitudes of the waves scattered from the different nuclei. If our considerations are limited to biatomic crystals, the form factor is given by

$$F=4\pi|A_1\sum_{abc}\exp[2\pi i(la+mb+nc) +A_2\sum_{\alpha\beta\gamma}\exp[2\pi i(l\alpha+m\beta+n\gamma)]|^2, \quad (6)$$

where abc are the positions in terms of the primitive translations of the lattice of the nuclei which scatter with amplitude A_1, and $\alpha\beta\gamma$ are the corresponding positions of the nuclei which scatter with amplitude A_2. For the BeO crystal this reduces to

$$F_{BeO}=4\pi|A_{Be}+A_O\exp 3\pi in/4|^2F_{Be}$$

where F_{Be} is to be obtained from Eq. (3). In particular, for $n=\pm1$, the amplitude dependent factor is

$$A_{Be}^2+A_O^2-\sqrt{2}A_{Be}A_O.$$

Since A_{Be} and A_O are of the same order of magnitude, this quantity depends rather sensitively on the relative signs of the amplitudes A_{Be} and A_O. It is larger if the signs are opposite. Thus, for the reflections from the twelve sets of planes $(l, m)=(\pm1, 0)$, $(0, \pm1)$, $(1, 1)$, $(-1, -1)$ with $n=\pm1$, there will be a considerable difference in the strength of the Bragg peak between the two cases of like sign and opposite sign. This makes it possible to determine experimentally by a transmission measurement whether the signs A_{Be} and A_O are equal or opposite.

The theoretical curves for the cross section as a function of energy are given in Fig. 2 for both possible choices of sign. In obtaining these curves, the magnitudes of the scattering amplitudes were obtained from

$$4\pi|A_{Be}|^2=\sigma_{Be}/\mu_{Be}^2, \quad 4\pi|A_O|^2=\sigma_O/\mu_O^2, \quad (7)$$

where σ_O is the scattering cross section of a free O atom (found as before from the scattering of one volt neutrons to be 4.1×10^{-24} cm^2) and μ_O is the reduced mass of the neutron plus a free O atom. The Debye temperature of BeO was estimated from the velocity of sound and found to be $\Theta=1200°$K. Comparison of the experimental points and the theoretical curves shows clearly that the signs of the amplitudes of the Be and O scattering are the same.

5. CONCLUSION

The good agreement between theory and experiment indicates that the application of Eq. (4) to other crystalline materials should give an adequate representation of the scattering cross section as a function of energy. There are, however, a number of conditions that may lead to deviations from this result.

Probably the most important of these would be the occurrence of such large microcrystals in the sample that the peaks in the scattering are wiped out by extinction in the crystals. An estimate of the maximum size of the microcrystals to be used can be obtained by determining what fraction of those neutrons of a given energy which hit a particular crystal at the Bragg angle are scattered. This fraction can be obtained by dividing the expression (1) by the projected cross-sectional area of the crystal which is given by $l^2\cos\theta=l^2b\lambda/2$. If we introduce the correct numerical factor which can be obtained by comparing Eqs. (1)–(4), the fraction of the neutrons scattered by a particular set of crystal planes turns out to be

$$N^2l^2F/\pi b^2. \quad (8)$$

Since it is desirable to have not more than 1 percent of the beam scattered by one microcrystal, the upper limit on the crystal dimensions may be taken to be

$$l\leq(\pi)^{\frac{1}{2}}b/10N(F)^{\frac{1}{2}}. \quad (9)$$

If $b=3\times10^7$ cm^{-1}, $F=10^{-23}$ cm^2 and $N=4\times10^{22}$, Eq. (9) becomes $l\leq5\times10^{-5}$ cm. Thus, for crystals of linear dimensions smaller than a micron, one would not expect an appreciable reduction in the peaks because of extinction. These dimensions refer to the prefect microcrystals of which the material is composed. Considerably larger crystallites would be acceptable if the crystallites consist of many such microcrystals oriented at small angles with respect to each other. In order to be sure that this condition was satisfied for the Be crystals on which were made the measurements discussed in Section 3, it was necessary to break

the material up mechanically; for BeO, there was no such difficulty.

Other sources of deviations from the theory may be the following:

(1) The microcrystals not randomly oriented. This may occur when the sample is prepared by extrusion.

(2) The temperature of the sample not small compared to its Debye temperature. Then an appreciable amount of inelastic scattering would be expected. This would render the peaks less sharp and would introduce appreciable scattering below the first Bragg limit.

(3) The crystal contains two or more isotopic constituents which have appreciably different scattering properties. The incoherent scattering background would then be appreciable. However, it is necessary that there be a very strong dependence of the scattering amplitude on the isotopic identity of the nucleus for this to be a large effect.

(4) The nuclei of the sample have a spin different from zero and the scattering is strongly spin dependent. This would again lead to an incoherent background which would be large only if the spin dependence of the scattering were very strong.

(5) If the sample used is made up of a very fine powder, the surface area will be so large that there is a chance that adsorbed surface films may contribute appreciably to the cross section. This may lead to an erroneous interpretation of the results, particularly if one is trying to distinguish between two possibilities corresponding to two different combinations of the signs of the scattering amplitudes. If a large amount of water, for example, is adsorbed on the crystals, there will be a smooth background cross section rising rapidly at low energies which could easily transform the lower curve in Fig. 2 into a curve that could hardly be distinguished from the upper curve.

If care is taken to avoid the difficulties mentioned above, it is believed that the transmission method offers a good procedure for determining the relative phases of the scattering of pairs of nuclei which can be compounded to form a microcrystalline material. This would then make it possible to determine the absolute sign of the scattering phases of a series of nuclei if the phase were determined for one particular nucleus.

The numerical work required for determining the theoretical curves in Figs. 1 and 2 was carried out by M. G. Goldberger.

PHYSICAL REVIEW VOLUME 71, NUMBER 9 MAY 1, 1947

Peak Contour and Half-Life of Metastable Ions Appearing in Mass Spectra

J. A. HIPPLE*
Westinghouse Research Laboratories, East Pittsburgh, Pennsylvania

(Received January 15, 1947)

A method is described for determining the half-lives of metastable ions by varying the voltage which sweeps the ions from the ionization chamber of a mass spectrometer. The half-life of the state corresponding to the transition $C_4H_{10}^+ \rightarrow C_3H_7^+ + [CH_3]$ has been found to be 2.0×10^{-6} second and the value found for the transition $C_4H_{10}^+ \rightarrow C_3H_6^+ + [CH_4]$ was 1.7×10^{-6} second. In answer to the objection that the diffuse peaks should not be prominent in the 180° instrument if they are to be attributed to spontaneous dissociation during transit, it is shown that this result is to be expected for metastable transitions. The relative number of ions in the metastable states initially is estimated.

INTRODUCTION

THE diffuse peaks appearing in the mass spectra of hydrocarbons have recently been attributed to the spontaneous dissociation of metastable ions during transit.[1,2] Several workers in the field have objected to this interpretation on the basis that the appearance of diffuse peaks in the 180° instrument is unexplained—the peaks having roughly the same appearance as in the sectored-field instrument such as that employing a deflection of 90°. In the latter instrument there is a considerable distance between the ion source and the deflecting magnetic field where the dissociation could occur without an appreciable deflection of the ions, and this situation does not obtain in the former case. This paper will attempt to show that a diffuse peak observed

* Present Address: National Bureau of Standards, Washington, D. C.

[1] J. A. Hipple and E. U. Condon, Phys. Rev. 68, 54 (1945).

[2] J. A. Hipple, R. E. Fox, and E. U. Condon, Phys. Rev. 69, 347 (1946).

with the 180° instrument will be quite similar in position and contour with the corresponding peak with the sectored-field instrument. In order to do this, it will be necessary to determine approximately the half-life of the metastable ion. The peak contour will then be constructed for simplified conditions to ascertain whether the actual contour can be explained reasonably by dissociation during transit.

DETERMINATION OF HALF-LIFE

Table I is a reproduction of a portion of Table II from an earlier paper.[2] The more rapid increase with ion-draw-out voltage ($\beta = V_1 - V_0$) of the peaks at the apparent mass numbers $m^* = 39.2$, 31.9, and 30.4 relative to the rest of the spectrum of n-butane was a potent argument for their origin being the spontaneous dissociations:

$$C_3H_7^+ (43) \rightarrow C_3H_5^+ (41) + [H_2] (2) \quad m^* = 39.2, \quad (1)$$

$$C_4H_{10}^+ (58) \rightarrow C_3H_7^+ (43) + [CH_3] (15) \quad m^* = 31.9, \quad (2)$$

$$C_4H_{10}^+ (58) \rightarrow C_3H_6^+ (42) + [CH_4] (16) \quad m^* = 30.4. \quad (3)$$

As before, brackets are placed around the neutral fragment since the mass spectrometer cannot determine the nature of the neutral fragment or fragments. The metastable ions will decay exponentially with time, and the higher values of β will cause them to reach the region where they may be detected as diffuse peaks earlier in their lifetime leading to a higher peak. A study of Table I in conjunction with the geometry of the instrument should make possible an estimate of the decay constant, λ.

Referring to Fig. 1, let it first be assumed that all ions that dissociate later than t_2 will contribute to the height of the diffuse peak. This

TABLE I. Relative peak heights at various voltages $(V_1 - V_0) = \beta$ (from Table II of Hipple, Fox, and Condon, Phys. Rev. 69, 347, 1946).

β	$\alpha'(\beta)$ 58	$\alpha'(\beta)$ 40	$\pi'(\beta)$ 39.2	$\pi'(\beta)$ 31.9	$\pi'(\beta)$ 30.4
1.0	1.00	1.00	1.00	1.00	1.00
2.0	1.73	1.57	2.22	2.21	3.82
3.0	1.78	1.67	2.62	2.72	5.26
4.0	1.75	1.69	3.11	2.97	5.52
5.0	1.75	1.69	3.33	3.29	6.07

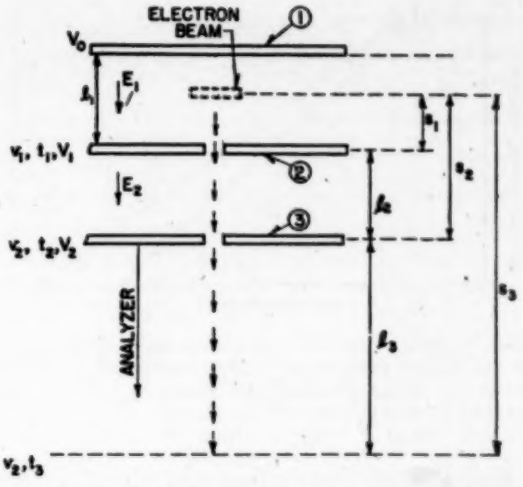

FIG. 1. Schematic diagram of ion source to relate the time of dissociation in terms of the geometry and the accelerating fields.

should hold fairly accurately for the sectored-field instrument if the half-life is quite short compared with the transit time through the analyzer. In this discussion only the field E_1 will be changed so $t_2(\beta)$ is defined as the value of t_2 when $V_1 - V_0 = \beta$, and $n^0(\beta)$ is the number of ions in a particular metastable state passing through the slit in electrode 3 when $V_1 - V_0 = \beta$. Considering the peak at $m^* = 31.9$, the collected ion current of mass 43 having 43/58 of the original energy will then be given by

$$n^0(\beta) = n_0 \exp -[\lambda t_2(\beta)], \quad (4)$$

$n^0(\beta)$ may be interpreted either as the number of ions of mass 58 left in a metastable state after passing through the slit in electrode 3, or the number of ions of mass 43 having 43/58ths of the original energy received at the ion collector (assuming all dissociate before reaching the collector and all these are collected). n_0 is the number of ions of mass 58 originally in the beam in the metastable state responsible for the diffuse peak at $m^* = 31.9$. As the normal stable ions increase in intensity with β, the metastable ions will also have this normal increase $\alpha(\beta)$ and hence

$$n^0(\beta)\alpha(\beta) = n(\beta). \quad (5)$$

Equation (4) now becomes

$$n(\beta) = \alpha(\beta) n_0 \exp -[\lambda t_2(\beta)]. \quad (6)$$

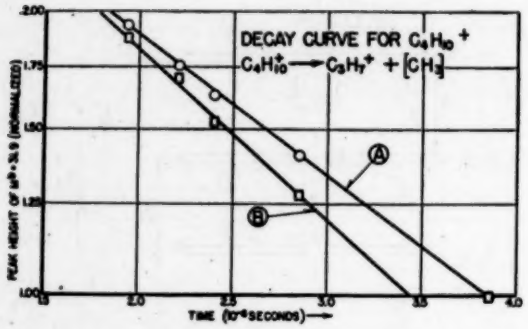

FIG. 2. Decay curve for the metastable state responsible for the diffuse peak at $m^*=31.9$ in n-butane. This is a plot of the data of Table I and Table II. For A mass 40 was used in normalizing and for B mass 58.

Equation (6) was derived with the assumption that all metastable ions passing through the slit in electrode 3 would contribute to the height of the diffuse peak regardless of the point at which they dissociate. Now suppose that, because of the geometry of the instrument, those ions which have travelled a distance greater than L in the analyzer will not contribute to the peak. Since the ion accelerating field E_2 is held constant, and most of the energy is acquired between electrodes (2) and (3), the velocity of the metastable ions remains essentially constant. Therefore, it can be assumed that all the ions contributing to the ion current being measured will dissociate between $t_2(\beta)$ and $t_2(\beta)+\tau$ where τ is a constant. From Eq. (6) this number is given by

$$\Delta n(\beta) = -\alpha(\beta)n_0 \exp-[\lambda[t_2(\beta)+\tau]] + \alpha(\beta)n_0 \exp-[\lambda t_2(\beta)]. \quad (7)$$

Normalizing to $\beta=\beta_0$

$$\frac{\Delta n(\beta)}{\Delta n(\beta_0)} = \frac{\alpha(\beta)n_0 \exp-[\lambda t_2(\beta)][1-\exp-[\lambda\tau]]}{\alpha(\beta_0)n_0 \exp-[\lambda t_2(\beta_0)][1-\exp-[\lambda\tau]]},$$

$$\frac{\Delta n(\beta)}{\Delta n(\beta_0)} = \frac{\alpha(\beta)}{\alpha(\beta_0)} \exp[\lambda(t_2(\beta_0)-t_2(\beta))]. \quad (8)$$

From Eq. (8) it is evident that the half-life may be determined without regard to those ions which dissociate at a time later than $t_2(\beta)+\tau$, i.e., considering only ions dissociating between $t_2(\beta)$ and $t_2(\beta)+\tau$. This, in turn, means that the half-life may be determined by varying β even though the half-life is not short compared with the transit time. The values of

$$n'(\beta)=\Delta n(\beta)/\Delta n(\beta_0)$$

and $\alpha'(\beta)=\alpha(\beta)/\alpha(\beta_0)$ for $\beta_0=1$ volt are given in Table I. It remains to determine $t_2(\beta)$.

Referring to Fig. 1, it can be shown that v_1, v_2, t_1, t_2 and t_3 are given by the following relations:

$$v_1=(2\alpha_1 s_1)^{\frac{1}{2}}, \quad (9)$$

$$v_2=(2\alpha_2 l_2+2\alpha_1 s_1)^{\frac{1}{2}}, \quad (10)$$

$$t_1=(2s_1/\alpha_1)^{\frac{1}{2}}, \quad (11)$$

$$t_2=(v_2-v_1)/\alpha_2+t_1, \quad (12)$$

and

$$t_3=l_3/v_2+t_2, \quad (13)$$

where $\alpha_1=E_1e/300m$ and $\alpha_2=E_2e/300m$, and E_1 and E_2 are expressed in volts per centimeter, e is the charge of the ion in e.s.u., and m is the mass of the ion in grams. In the apparatus used for obtaining the data of Table I, $l_1=0.39$ cm, $l_2=1.0$ cm, and s_1 is estimated to be 0.25 cm. The ion accelerating voltage was 600 volts and, therefore,

$$E_2=600/1.0=600 \text{ volts/cm}.$$

The values of $t_2(\beta)$ for various values of β are shown in Table II together with the corresponding values of $n'(\beta)/\alpha'(\beta)$. In column 3 the values of $\alpha'(\beta)$ for mass 40 are used and in column 4 the values for mass 58. The values of $n'(\beta)/\alpha'(\beta)$ are plotted in Fig. 2. It would seem more reasonable to use the $\alpha'(\beta)$ for mass 58 if the variation in height of a normal peak with changes in β is to be attributed to discriminating effects occurring before the ion enters the analyzer. The experimental results indicate that the change in the height of mass 58 due to the variation in the transit time of those ions of mass 58 in a metastable state is small. From

TABLE II. Normalized peak height $(n'(\beta)/\alpha'(\beta))$ of $m^*=31.9$ for various values of β (ion-draw-out voltage).

β	$t_2(\beta)\times10^6$ sec.	$\frac{n'(\beta)}{\alpha'(\beta)}$ $\frac{31.9}{40}$	$\frac{n'(\beta)}{\alpha'(\beta)}$ $\frac{31.9}{58}$
1.0	3.86	1.00	1.00
2.0	2.86	1.41	1.28
3.0	2.40	1.63	1.53
4.0	2.21	1.76	1.70
5.0	1.94	1.94	1.88

Fig. 2, it is seen that the half-life is approximately 1.6×10^{-6} second when correcting with mass 58 and 2×10^{-6} second with mass 40.

REMEASUREMENT OF THE DECAY CURVE

The results obtained with the data previously published suggested the desirability of repeating the experiment for a more extended range of β. This has been done with another mass-spectrometer tube of the same type. The main ion accelerating voltage was raised to 1000 volts and β varied from 0.18 to 10.0 volts. The electron accelerating voltage was 75 volts. The data is summarized in Table III and points on Fig. 3 are plotted from this data in the same manner as curve B of Fig. 2 with the exception that it is assumed that the measured voltage scale must be corrected by adding 0.2 volt to the measured values. This is the same type of correction employed in the measurement of appearance potentials with the mass spectrometer and could be attributed to contact potentials, polarization effects, or incomplete shielding of the ionization region from the strong fields between neighboring electrodes. In the present example this added voltage is only 0.02 percent of the main accelerating voltage and it is reasonable to expect the field E_2 to be shielded incompletely because of the slit in electrode 2. This correction is only important for small values of the ion-draw-out voltage. The experimental points are quite close to a stright line on the semi-log plot over a range from 1.5 to 6×10^{-6} second. The half-life from this curve is 2.0×10^{-6} second. Probably the greatest source of error is caused by the difficulty in determining s_1 accurately.

TABLE III. Data similar to Table II but obtained with a different mass-spectrometer tube using 1000-volt ions and an extended range of β.

β (volts)	$t_2(\beta)\times10^6$ (seconds)	Peak height (arbitrary units) 58	57	29	31.9	30.4	$n'(\beta)/\alpha'(\beta)$ 31.9/58	30.4/58
0.38	5.89	185.6	41.0	522.0	0.4		1.00	
0.45	5.44	393.5	81.7	1068.	1.2	0.6	1.41	1.00
0.70	4.43	530.0	111.0	1410.	2.1	1.0	1.84	1.24
0.95	3.84	551.0	115.6	1436.	2.7	1.6	2.27	1.91
1.20	3.46	547.0	114.6	1410.	3.1	1.7	2.63	2.04
3.20	2.25	556.0	116.6	1442.	4.9	3.0	4.09	3.54
5.20	1.84	560.0	—	1386.	5.3	3.3	4.39	3.87
10.20	1.41	444.0	91.0	1006.	5.1	3.1	5.33	4.58
The values below were obtained several days later and although $\alpha'(\beta)$ and $n'(\beta)$ are different, their ratio should fall closely on the curve if the method of correcting for the "normal" increase with ion-draw-out voltage is effective.								
1.70	2.96	476.0	97.0	1154.	3.0	1.7	2.92	2.34
2.45	2.53	482.0	98.8	1200.	3.9	2.3	3.75	3.13

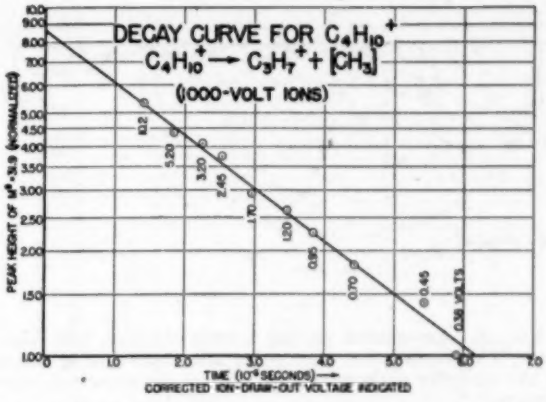

FIG. 3. Semi-log plot as in Fig. 2 but with new data over a more extended range.

PEAK CONTOUR IN 180° INSTRUMENT

Having determined the half-life, the next step is to relate the time at which the dissociation occurs with the apparent mass registered by the instrument. The simplifying assumptions will first be made that all the ions enter the analyzer normal to a line drawn between the entrance and exit slits, and the width of the entrance slit will be neglected. The metastable ion of mass m_0 then enters the analyzer and first travels in a circular path of radius r_0; after an angular deflection θ or a time T after entering the analyzer, it dissociates and the ionic component of mass m then travels a circular path of radius $r_0^*=(m/m_0)r_0$ (Fig. 4). When dissociation occurs at the moment of entry into the analyzer then $r^*=r_0^*$. The time T is given by

$$T=\frac{r_0}{v_2}\cos^{-1}\left[\frac{2m_0^{\frac{1}{2}}(m_0^{*\frac{1}{2}}-m_0^{\frac{1}{2}})-4m^{*\frac{1}{2}}(m^{*\frac{1}{2}}-m_0^{\frac{1}{2}})}{2(2m^{*\frac{1}{2}}-m_0^{\frac{1}{2}})(m_0^{\frac{1}{2}}-m_0^{*\frac{1}{2}})}\right]. \quad (14)$$

In this equation m_0^*, m_0, v_2, and r_0 are known from the experimental conditions and therefore T is known as a function of the apparent mass.

Since the half-life has been determined, the intensity as a function of T and through (14) as a function of the apparent mass m^* is known. In determining the peak contour of the diffuse peak at 31.9 in n-butane, $m_0=58$ and $m_0^*=(43)^2/58$. Thus, the number of ions between m^* and $m^*+\Delta m^*$ will be

$$n(m^*)-n(m^*+\Delta m^*) = \alpha n_0 \exp-[\lambda t_2][\exp-[\lambda T(m^*)] - \exp[\lambda T(m^*+\Delta m^*)]]. \quad (15)$$

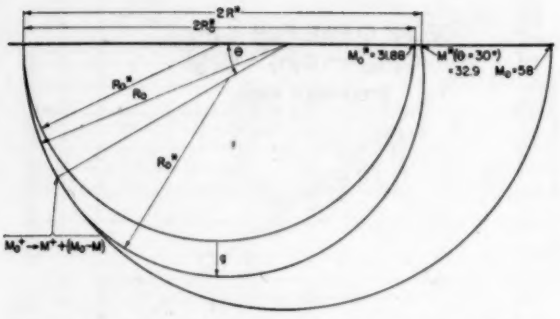

FIG. 4. Dissociation during transit through 180° analyzer. The dissociation may occur after appreciable travel in the analyzer without a large shift of the apparent mass from m_0^*.

In order to plot the peak contour the term $\alpha n_0 \exp-[\lambda t_2]$ may be taken as unity. If the half-life is 2×10^{-6} second then $\lambda=0.346\times10^{+6}$ sec^{-1}. Taking intervals of Δm^* the corresponding values of the time T are obtained from (14). If we assume that the tube is designed for a radius of curvature in the analyzer of 12.5 cm ($r_0^*=12.5$ cm) then $r_0=16.9$ cm. For ions of mass 58 and kinetic energy of 600 ev, $v_2=4.46\times10^6$ cm/sec. The values of $n(m^*)-n(m^*+\Delta m^*)$ for successive values of m^* are given in Table IV and from this data the histogram of Fig. 5 was plotted. This shows the general shape of the peak contour for the diffuse peak at mass 32 in *n*-butane which would be expected when this molecule is studied with the 180° instrument and the beam does not hit any part of the analyzer during transit. It is clear that the maximum appears at essentially the same position for the 180° instrument as for the sectored-field instrument. For a smaller value of the half-life, the ion current would have been even more concentrated about $m^*=32$.

Now in the 180° instrument it is conventional to place fairly wide slits at various points in the analyzer to prevent the formation of "ghosts" by reflections from the walls. These slits will cut out all those ions in Fig. 5 except those having an apparent mass close to 31.9. For instance, suppose the excursion from the median ray (r_0^*) is limited to a distance g in Fig. 4 by a slit at an angular deflection of 90° for this ray. Then for metastable ions dissociating after a small angular deflection θ in the analyzer, g will be given by

$$g=(r_0-r_0^*)(\theta). \qquad (16)$$

If $g=0.6$ cm, then $\theta=8°$. In terms of m^* this means that ions of $m^*>31.95$ (Fig. 5) will be eliminated.

It is apparently true that ions should be recorded only very close to $m^*=31.9$ in both the 180° instrument and the sectored-field instrument. The intensity should be somewhat greater in the sectored-field instrument. The difference, however, is not as great as one might expect. In the example just given, approximately 17 percent of the ions dissociating after entering the 180° analyzer would be collected. With the sectored-field instrument the ions are rapidly defocussed when the dissociation occurs in the magnetic field. If a 90° instrument with a radius of curvature of 12.5 cm is considered (such as that used for obtaining the data used in this paper), the distance of travel between the ion source and the magnetic field region is about 12.5 cm when the fringing field is neglected. However, since the air gap is ~2.5 cm, the fringing field is large for a considerable distance from the magnet and it would be unreasonable to assume that all ions resulting from dissociation in the first 12.5 cm of path in the analyzer will be properly focussed at $m^*=31.9$. If this distance is assumed to be as great as 8 cm, then $T=1.8\times10^{-6}$ sec. and 46 percent of the ions will be collected, which is only about 3 times the value for the 180° instrument. The diffuseness of the peaks in each case could be attributed to a mutual kinetic energy imparted to the fragments at dissociation, or the defocussing of the paraxial rays as a result of dissociations occurring in the magnetic field.

However, some of the ions will strike the tube

TABLE IV. Number of ions as a function of m^*.

m^*	θ (radians)	T (microseconds)	$n(m^*)$	$n(m^*)-n(m^*+\Delta m^*)$
31.88	0	0	1.00	
31.9	0.075	0.284	.906	0.094
31.95	.139	.527	.833	.073
32.0	.182	.690	.788	.045
32.05	.217	.822	.752	.036
32.1	.246	.932	.724	.028
32.15	.272	1.031	.700	.024
32.2	.297	1.125	.678	.022
32.3	.340	1.288	.640	.038
32.4	.377	1.429	.610	.030
32.5	.412	1.561	.583	.027
32.6	.443	1.679	.559	.024
32.7	.473	1.792	.538	.021
32.8	.500	1.895	.519	.019
32.9	.527	1.997	.502	.017
33.0	.551	2.088	.486	.016

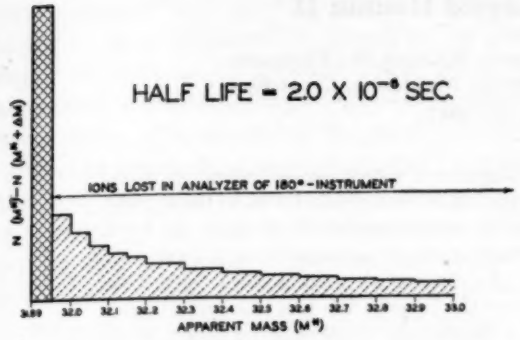

FIG. 5. Histogram illustrating that a large number of the ions dissociating after entering the analyzer of the 180° instrument will have an apparent mass close to m_0^* (=31.89). Ions having m^* very much different from m_0^* will be lost in the analyzer.

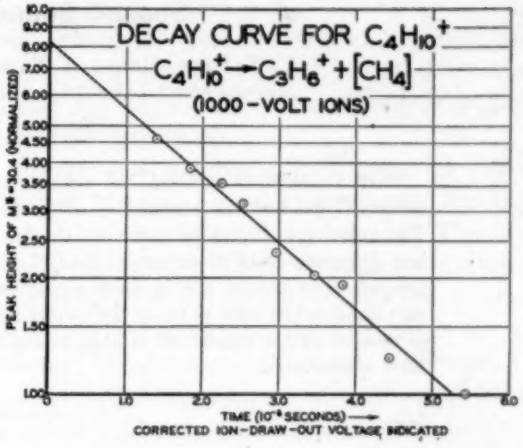

FIG. 6. Decay curve for metastable state responsible for the diffuse peak at $m^*=30.4$ in n-butane.

walls in passing through the 90° analyzer so the percentage getting through would be less than 46 percent. The value obtained would depend somewhat on the position of the main magnet relative to the mass-spectrometer tube.

In discussing the peak contour the width of the entrance slit was neglected and the distribution in intensity was obtained along the focal plane of a normal ion beam (not metastable). Actually the data was taken with an exit slit at a fixed position and the spectrum was scanned by varying the magnetic field. This makes no essential difference in regard to the general conclusions. Clearly, of course, the exit slit must be sufficiently wide to allow the passage of ions in the range between $m^*=31.89$ and $m^*=31.95$ (see Fig. 5) in order that the peak height will be a measure of the number of metastable ions that have passed through the analyzer without being lost. This requirement is fulfilled in the analytical instruments of the 180° type in general use today. The entrance slit to the analyzer is generally much smaller than the exit slit and for this reason will not materially affect our conclusions.

RELATIVE NUMBER OF IONS IN THE METASTABLE STATE INITIALLY

Since the half-life has been determined, it should now be possible to estimate the relative number of ions of mass 58 originally in the metastable state responsible for the diffuse peak at $m^*=31.9$. For $\beta=3.2$ volts, the peak height of $m^*=31.9$ is 4.9 divisions from Table III. If it is assumed on the basis of the previous discussion that only 40 percent of the ions that dissociate in the analyzer contribute to this peak height, then the peak height must be multiplied by 2.5 to obtain the value of $n^0(\beta)$, i.e., $n^0(\beta)=12.2$. All the quantities in (4) are now known except n_0 and this may be calculated:

$$n_0=12.2\exp[(0.346\times10^6)(2.25\times10^{-6})]=26.7.$$

This is only about 5 percent of the number of ions of mass 58 which reach the ion collector without dissociating.

The decay with time of the ions in the metastable state responsible for the diffuse peak at $m^*=30.4$ is shown in Fig. 6. The transition involved here is

$$C_4H_{10}^+\rightarrow C_3H_6^++[CH_4].$$

The data were obtained from the same charts used for the points in Fig. 3. This peak was smaller than that at $m^*=31.9$, and the current for $\beta=0.38$ volts was too small to include in the measurements. From this curve the half-life is 1.7×10^{-6} second and the corresponding value for n_0 is 18.8 divisions estimated in the same way as described for the other metastable transition. This is between 3 and 4 percent of the number of ions of mass 58 which reach the ion collector without dissociating.

Second Sound in Liquid Helium II

C. T. LANE, HENRY A. FAIRBANK, AND WILLIAM M. FAIRBANK
Sloane Physics Laboratory, Yale University, New Haven, Connecticut

(Received January 22, 1947)

With a resonance method, the velocity of the temperature waves (second sound) in liquid helium II has been determined as a function of temperature from about 1.4°K to the λ-point. The velocity is found to be zero at the λ-point, reaches a maximum of 20.46 m/sec. at 1.7°K and decreases to 19.80 m/sec. at 1.42°K. The accuracy of the measurements is at least ±0.5 percent. The results are in good agreement with the theoretical predictions of both Tisza and Landau but tend to favor the former's theory over the latter's. The fact that second sound generated in the superfluid is able to register on a microphone diaphragm immersed in the fluid is discussed.

INTRODUCTION

IN an attempt to explain the many anomalous properties of liquid helium at temperatures below 2.19°K (liquid helium II), F. London has proposed a model for this fluid which is based on an ideal gas obeying Bose-Einstein statistics. In these statistics a peculiar "condensation" effect takes place at a certain critical temperature T_c whereby a certain fraction of the atoms go into a highly degenerate ground state, the remainder remaining in excited states. In particular the number of degenerate atoms N_0 is given by

$$N_0=N\left\{1-\left(\frac{T}{T_c}\right)^{\frac{3}{2}}\right\}, \quad T<T_c, \tag{1}$$

N being the total atoms present per unit volume and

$$T_c=\frac{h^2}{2\pi mk}\left(\frac{n}{2.6124}\right)^{\frac{2}{3}}. \tag{2}$$

By putting the appropriate values for helium into Eq. (2) London finds $T_c=3.14$°K which is surprisingly close to the λ-point (2.19°K) considering that we are dealing with an ideal gas and not a liquid. Below T_c the entropy of the system is caused solely by excited atoms, the degenerate ones have zero entropy.

Using this admittedly rough model, London has been able to show that a number of known properties of liquid helium II are theoretically derivable, at least qualitatively. L. Tisza has improved the London model in a number of particulars. He supposes liquid helium II to be a "mixture" of two kinds of atoms, superfluid of density ρ_s and normal of density ρ_n. These correspond to the degenerate and excited atoms in London's Bose-Einstein gas and again the entropy of ρ_s is zero. A further assumption made by Tisza, which appears somewhat difficult to justify, is that the interaction between ρ_s and ρ_n is negligible and indeed ρ_s atoms do not exchange momentum with either ρ_n or other atoms. Tisza further supposes that the density function for degenerate atoms is

$$\rho_s=\rho\left\{1-\left(\frac{T}{T_c}\right)^{\sigma}\right\}, \quad T<T_c,$$

$$\rho=\rho_s+\rho_n, \quad T_c=2.19°K,$$

and $\sigma\simeq 5$ to 6 as against $\frac{3}{2}$ in the ideal Bose gas. The justification for this latter modification lies partly in the better fit obtained with the experimental results for the specific heat discontinuity at the λ-point and partly because of the fact that, as London had observed, it is probable that the introduction of interaction between the atoms would modify the density function in this direction.

From this modified theory and a consideration of the hydrodynamical equations of the two phases, Tisza in 1940[1] predicted that temperature differences in liquid helium II should be propagated as a wave motion with a characteristic, temperature dependent velocity.

The experimental proof of this prediction was made in 1944 by V. Peshkov,[2] and these temperature waves were named "second sound."

[1] L. Tisza, J. de phys. et rad. [8] 1, 164, 350 (1940).
[2] V. Peshkov, J. phys. et rad. U.S.S.R. 8, 381 (1944).

Peshkov generated these waves by means of a wire resistance coil in which a variable temperature was maintained by means of an alternating current, and detected them from the indications of a small phosphor bronze resistance thermometer. By measuring the wave-length of running or standing waves (produced by reflection from the liquid surface) and knowing the heat waves to be double the frequency of the exciting a.c. he could determine the velocity which turned out to be of the order of 20 m/sec., i.e., around 10 times less than the velocity of ordinary sonic waves.

In Tisza's theory the velocity of second sound is given by

$$c=\left[-\frac{\rho_n}{\rho_s}\frac{\partial}{\partial T}\left(\frac{1}{S}\right)\right]^{-\frac{1}{2}}$$

where S is the entropy of helium II, which has been accurately determined as a function of temperature from measurements on the specific heat. Accordingly measurements of C as a function of temperature would yield information on the temperature variation of the important ratio ρ_s/ρ_n. The purpose of the following experiment is therefore clear. In addition to this we must mention that the existence of second sound was predicted independently by L. Landau,[3] somewhat later than Tisza, by use of an entirely different kind of theory. We shall discuss the bearing of the experimental results on the two theories at the end of this paper.

EXPERIMENTAL DETAILS

Following discussions with L. Onsager, of this laboratory, we decided to attempt to measure second sound velocities with the following kind of arrangement. The second sound would be generated by an a.c. heater of the same general type as that used by Peshkov, and standing waves would be produced in a column of liquid helium by reflections from the free surface. If this free surface were an anti-node, the temperature of this surface would fluctuate at double the frequency of the a.c. source, giving rise to a fluctuating evaporation of the liquid at this surface. In consequence small periodic fluctuations in the pressure of the vapor above the liquid surface would occur (first sound). These fluctuations of pressure would register on a microphone immersed in the helium vapor, and hence second sound resonances in the liquid would be detectable.

Figure 1 is a schematic diagram of our apparatus. He and Ni are, respectively, the liquid helium and liquid nitrogen Dewars. The latter is of Pyrex with a highly evacuated interspace. The helium Dewar, on the other hand, is of soft glass and the interspace is filled with air at a pressure of about 2 millimeters mercury. This has the following purpose. Before liquid helium is admitted, the apparatus in this Dewar is cooled to the temperature of liquid nitrogen, the air in its interspace acting as the heat transfer medium. A large fraction of the heat content of this apparatus is thereby removed and the load

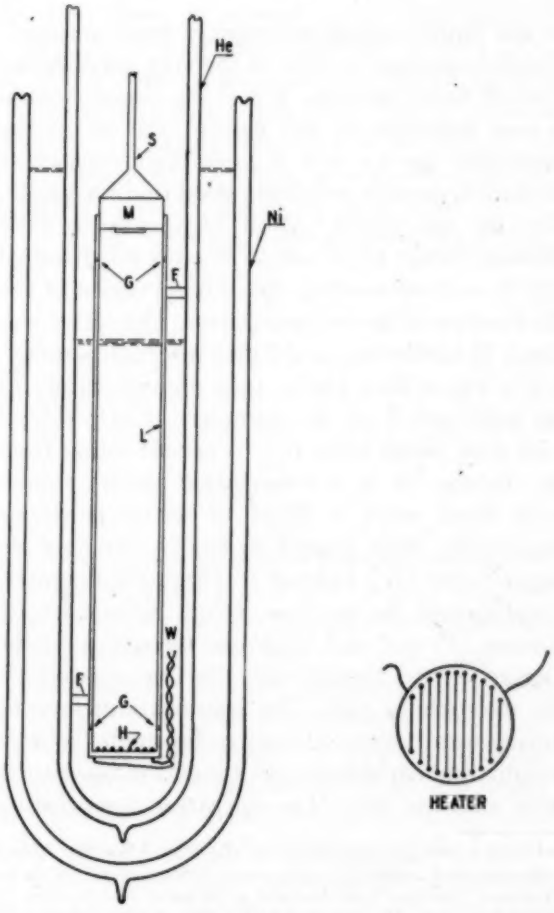

FIG. 1. Schematic drawing of the apparatus.

[3] L. Landau, J. Phys. U.S.S.R. 5, 71 (1941).

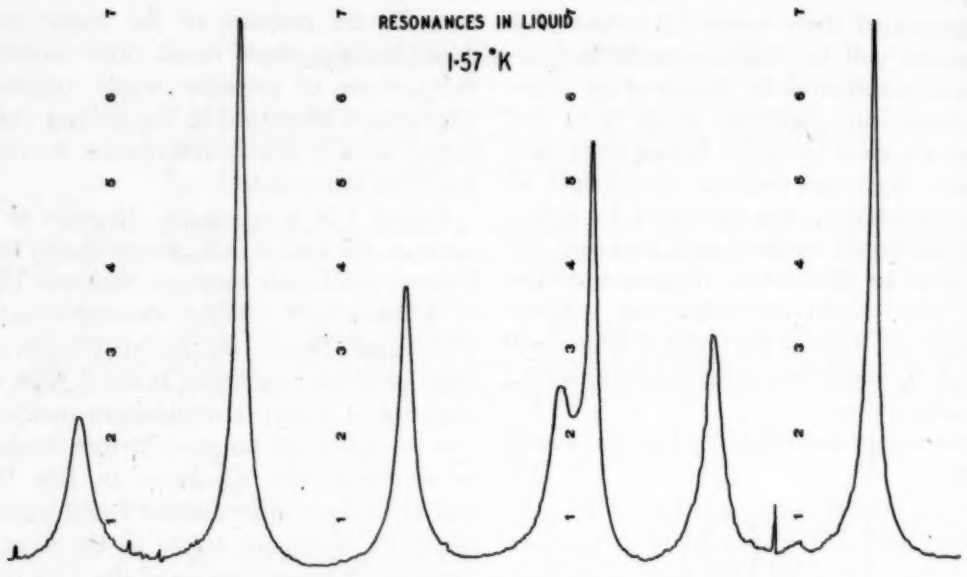

FIG. 2. Second sound resonances as registered on recording potentiometer at 1.57°K. The microphone is in the vapor above the liquid surface.

on the liquid helium accordingly much reduced. This is important in view of the very small latent heat of liquid helium. When the liquid helium is now admitted to the Dewar, the air in the interspace freezes and a very high vacuum is produced, thereby providing good thermal insulation for the liquid.[4] Both Dewars were fully silvered except for a pair of narrow longitudinal slits in each permitting visual observation of the the interior of the helium Dewar. The latter was about 18 inches long and 1 inch internal diameter. *L* is a thin walled Lucite tube approximately 15 cm long and 2 cm in diameter. It is provided with four small holes (*G*) to permit filling from the Dewar. *H* is a constantan heater, wound with 3-mil wire, a detail of which is shown separately. This heater is fed by number 40 copper wire (*W*) twisted to eliminate magnetic coupling into the receiver circuit. Several Lucite spacers (*F*) are used to center the cavity in the Dewar. Fitted tightly into the Lucite cavity is the microphone (*M*). The specifications for this device were severe. It had to be small, light in weight, and capable of operating at temperatures near absolute zero. The operating temperature ruled out the usual Rochelle salt-crystal type and we finally made use of the receiver of a Sonotone hearing aid used in "reverse" which is a magnetic type[5] instrument. The whole assembly is supported from the top of the Dewar by a small, thin-walled, stainless steel tube (*S*). This tube contains an insulated inner conductor and the pair form the shielded microphone leads.

The heater is fed continuously with 1000-cycle a.c., of good wave form, from a stable tuning fork oscillator. The power fed into the heater, which had a resistance of about 60 ohms at liquid helium temperature, was roughly 1/25 watt. The microphone output was amplified by an amplifier roughly tuned to 2000 cycles. This latter was provided with both a.c. and rectified output. The rectified output was fed into a Brown high speed recording potentiometer with a chart speed of 2 inches per minute. The Lucite cavity was illuminated through the slits in the Dewars by means of an external fluorescent lamp and the liquid helium level in the cavity was observed with a cathetometer. The vapor pressure in the cryostat was read on an absolute manometer filled with diffusion pump oil and was controlled manually by means of a needle valve. The 1937

[4] This technique originated at the Royal Society Mond Laboratory, Cambridge, and was communicated to us by Professor Onsager who learned of it on a recent visit to that laboratory. We found it to be immensely useful in all sorts of work with liquid helium and also liquid hydrogen.

[5] We are indebted to Dr. L. Grant Hector of Sonotone Corporation for his gift of several of these devices.

Leiden Scale was used in computing the corresponding absolute temperatures.

The procedure in taking data was as follows. As the liquid helium slowly evaporated and the level in the cavity fell, cathetometer readings were taken as a function of time. This clock was synchronized with the recorder chart, which recorded a series of resonance peaks. By plotting the liquid level as a function of time (this was always a straight line when the temperature was steady) the height of the liquid column in the cavity at each resonance was known. The difference in height between two successive resonance peaks being, of course, one-half wave-length. Usually about 6 to 8 peaks were taken at each temperature. Figure 2 shows a typical series of such resonance peaks at 1.57°K. One pair of plates of an oscilloscope were connected to the heater oscillator, the other pair to the a.c. output of the microphone amplifier. The resulting Lissajous figure confirmed that the sound frequency was double the electrical heater frequency.

RESULTS

Using the previously described method we determined the second sound velocity at a number of temperatures from about 1.4°K to the λ-point. Since we believe our accuracy is better than ±0.5 percent we present the data in both tabular (Table I) and graphical (Fig. 3) form. It will be noticed that the velocity extrapolates to zero, very accurately, at the λ-point as the theory requires.

It is apparent from our data that the liquid column, at resonance, is probably oscillating with a temperature anti-node at both the free surface and the heater surface. This fact enables us to compute the wave-length with great accuracy. Thus, at a given temperature, having roughly determined the half-wave-length from the distance between successive resonance peaks it is possible to assign a definite number of half-wave-lengths (n) to the whole liquid column at each resonance. If then successive resonant lengths of liquid column be designated by L_0, $L_1, \cdots L_s$ we found the following very accurately true:

$$\frac{L_0}{n}=\frac{L_1}{n-1}=\frac{L_2}{n-2}=\cdots=\frac{L_s}{n-s}$$

and therefore

$$\frac{\lambda}{2}=\frac{\sum_0^s L_i}{(s+1)(n-s/2)}.$$

In most of our velocity determinations S was of the order of 6 or 7 and n was usually about 30 or so and hence a very accurate determination of λ was possible.

In one run we held the temperature constant for about 23 successive resonances. The resonance peaks varied widely in height and width and appeared to be modulated by a much longer wave-length. We were able to determine this modulating wave-length roughly and the resulting velocity was of the order of the velocity of normal sound in helium vapor at the prevailing pressure and temperature in the vapor space of

TABLE I. Second sound velocity *versus* temperature.

°K	meters/sec.
1.425	19.80
1.453	19.86
1.570	20.23
1.607	20.38
1.685	20.46
1.780	20.16
1.795	20.08
1.994	17.12
2.074	14.13
2.150	9.40

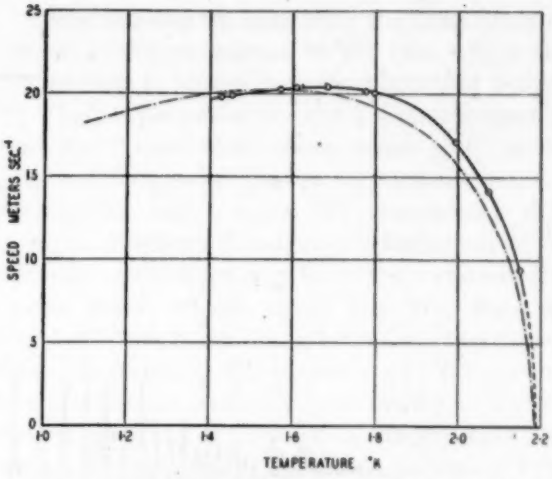

FIG. 3. Second sound velocity as a function of temperature. The heavy line with circles is the experimental curve. The lighter broken line is the theoretical curve computed from Tisza's theory of liquid helium II.

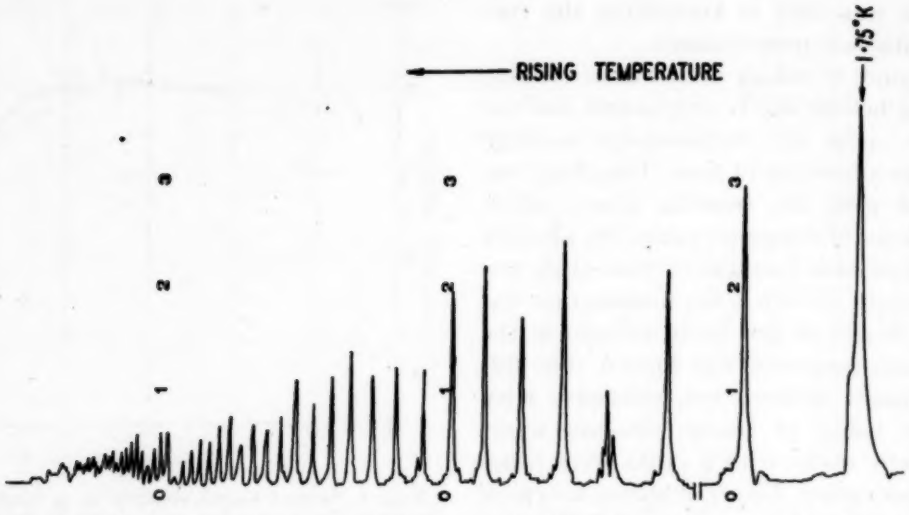

FIG. 4. Second sound resonances as registered on recording potentiometer with the microphone completely immersed in the liquid.

the Lucite cavity. All our runs showed this modulating feature to a greater or lesser extent.

Much more rarely we observed a double resonance peak. Such a one is shown on the *third peak* from the left in Fig. 2. We only observed two such twin peaks in all our work. In both cases only one of the twins fitted our second sound data. Assuming the spurious peak was resonance of ordinary sound in the liquid we could show that it was in accord with the known value of this velocity.

A rather curious effect was invariably observed when the liquid surface in the cavity was about even with the top of the heater wires. We always obtained a pair of second sound resonance peaks close together at this stage.

One run was made which was a departure from our standard technique. In this case the microphone was completely immersed in the liquid helium II and there was no observable vapor space in the Lucite cavity as observed by the cathetometer telescope.* The temperature was set at about 1.75°K and allowed to rise slowly and steadily up to the λ-point. Figure 4 shows the recorder chart record in this case. Examination of these data, with the curve of Fig. 3, leaves little doubt but that we are observing true second sound resonances in this case. Here, of course, both the frequency and the length of the resonant cavity are constant and a peak will be obtained whenever the temperature is such that the second sound velocity has a value capable of rendering this fixed system resonant. If L is the length of the cavity and f_0 the steady heater current frequency, then we shall observe a resonance peak when the second sound velocity $V(T)$ is given by

$$V(T)=\frac{4f_0L}{n},$$

where n is a whole number. Accordingly, starting at some known temperature (and velocity), near the maximum in the curve, and proceeding to the λ-point we should get a large number (theoretically an infinite number) of resonance peaks corresponding to velocities given by n, $n+1$, $n+2$, $\cdots$ in the above formula. As the temperature approaches the λ-point the peaks will be closer together due to the steepness of the velocity-temperature curve in this region until the speed of the recorder is no longer sufficient to record all the peaks. This is approximately what we observe.

DISCUSSION

As mentioned previously, a theoretical relation for the second sound velocity *versus* temperature curve has been deduced by Tisza depending on (1) the experimentally determined relationship

* In view of the enormous heat conductivity of liquid helium II no "vapor lock" would be expected. Vapor locks in liquid helium I and liquid hydrogen always occurred in similar circumstances.

between the entropy and the temperature, (2) ρ_s/ρ_n as a function of temperature. If one takes, following London,[6] as an average in the range from 1°K to the λ-point,

$$S=2.1\times10^{3}T^{5.6}\ \text{erg/°K g},$$

$$\rho_n=\rho\left(\frac{T}{2.19}\right)^{5.6},$$

then we obtain

$$c=2.6\times10^{3}\left[\frac{T}{2.19}\left[1-\left(\frac{T}{2.19}\right)^{5.6}\right]\right]^{\frac{1}{2}}\ \text{cm/sec.}$$

This function is plotted as a broken line in Fig. 3 and the agreement is seen to be very good. As mentioned in the introduction, the Landau theory predicts that the temperature variation of velocity shall follow a somewhat different course than that predicted by the Tisza theory. Thus at absolute zero the velocity according to Tisza should be zero, according to Landau it should be finite. The two theories, therefore, diverge in the neighborhood of 1°K, Landau showing a rising velocity, Tisza a falling one as the temperature decreases. Unfortunately we are unable to achieve a temperature below 1.4°K with our set-up but in view of the accuracy of our measurements and the fact of a distinct maximum in our curve, Tisza's theory seems to be somewhat favored over Landau's.

There remains the reason for the observance of second sound resonances in the case where the microphone is totally immersed in liquid helium II. There is no reason to expect, from the theory, that the temperature waves could give rise to pressure fluctuations in the liquid and therefore register an effect upon the microphone diaphragm. Professor Onsager has suggested to us that the mechanism may lie in the nature of the cavity which we are using. Referring back to Fig. 1 the four small filling holes *G* will be noted. The temperature fluctuations of the second sound inside the cavity will, according to Tisza's theory, produce a flow of ρ_s atoms into the cavity through the holes and a balancing flow of ρ_n atoms out through the holes. The flow of ρ_s atoms will be frictionless, but the ρ_n atoms, possessing viscosity, will probably experience a pressure drop in their passage through the holes. Since the flow of the ρ_s and ρ_n will be fluctuating we could by this mechanism have fluctuations of pressure in the cavity, induced by the second sound, which would be capable of registering on our microphone diaphragm.

It will be observed from Fig. 2 that many of the resonance peaks are extremely sharp, indicating a high "*Q*". This suggests that both the transmission coefficient across the liquid surface, and the dissipation in the liquid, are small. The absence of end effects in the resonant column also confirms the low transmission coefficient.

Finally we should like to express our thanks to Professor Lars Onsager for his many valuable discussions throughout the course of this work. We are also indebted to Mr. Robert T. Webber for his aid in taking data. This work was financially supported by the U. S. Navy under contract N6ori-44, Task Order III.

[6] We are greatly indebted to Professor Tisza for drawing our attention to his articles in *Journal de Physique*, copies of which had not reached us, and for making available to us an advance copy of F. London's paper before the Cambridge conference in 1946. The above formulas are drawn from this latter source. Mr. Tisza also communicated to us Peshkov's results, given at the same conference, which are in good agreement with ours.

Theory of the Propagation of Shock Waves*

STUART R. BRINKLEY, JR.** AND JOHN G. KIRKWOOD
Department of Chemistry, Cornell University, Ithaca, New York

(Received January 22, 1947)

A new theory of propagation of one-dimensional shock waves is described. The partial differential equations of hydrodynamics and the Hugoniot relation between pressure and particle velocity are used to provide three relations between the four partial derivatives of pressure and particle velocity, with respect to time and distance from the source, at the shock front. An approximate fourth relation is set up by imposing a similarity restraint on the shape of the energy-time curve of the shock wave and by utilizing the second law of thermodynamics to determine, at an arbitrary distance, the distribution of the initial energy input between dissipated energy residual in the fluid already traversed by the shock wave and energy available for further propagation. The four relations are used to formulate a pair of ordinary differential equations for peak pressure and shock wave energy as functions of distance from the source. The theory takes proper account of the finite entropy increment of the fluid produced by the passage of the shock and permits the use of the exact Hugoniot curve of the fluid in the numerical integration of the basic equations.

INTRODUCTION

IN discussing earlier work by Poisson,[1] Stokes[2] appears to have first suggested the possibility of the propagation at greater than acoustic velocity of discontinuous pressure waves. Earnshaw[3] and Riemann[4] have discussed the laws of propagation of waves of finite amplitude and the building up of the discontinuity. The conditions for a wave of permanent type have been investigated by Rankine[5] and Hugoniot[6] who have provided statements of the conditions for the continuity of mass, momentum, and energy across the moving discontinuity. Rayleigh[7] has shown how to solve the hydrodynamic equations for plane shock waves when the pressure and density are connected by the adiabatic law.

An exact solution for the cases of spherical and cylindrical shock waves cannot be given, due to the spherical and cylindrical divergence terms of the equation of motion. A straight forward attack on the mathematical problem may be based upon the numerical integration of the partial differential equations of hydrodynamics. However, the labor involved in this approach is so great as to limit it to special applications. The need for a more flexible and rapid theoretical method, based if necessary on well-defined approximations, is therefore clear. Such a method has been previously developed for shock waves in water from spherical charges of explosive.[8] Underwater explosion waves are simpler to treat than blast waves in air, since the relatively small entropy increment produced at the shock front permits the use of the approximation of adiabatic flow. Failure of this approximation in air has until now prevented the formulation of an adequate theory of blast waves in air.

A theory of underwater shock waves has recently been presented by Osborne and Taylor.[9] Their theory is based upon the acoustic approximation and is therefore strictly valid only for small excess pressures at large distances from the source.

In the present communication, we describe a a theory of the propagation of one-dimensional —that is, plane, cylindrical, and spherical— shock waves which is valid both in air and water. The theory takes account of the finite entropy increment in the fluid resulting from the passage of the shock wave. It also permits the use of the

* This paper is a report on a portion of work done at Cornell University under Contract OEMsr-121 with the office of Scientific Research and Development.

** Present address: Central Experiment Station, U. S. Bureau of Mines, Pittsburgh, Pennsylvania.

[1] M. Poisson, J. de l'école polyt. **7**, 319 (1808).
[2] G. G. Stokes, Phil. Mag. **33**, 349 (1848).
[3] S. Earnshaw, Phil. Trans. **A150**, 133 (1850).
[4] B. Riemann, Nachr. Ges. Wiss. Göttingen **8**, 43 (1860).
[5] W. J. M. Rankine, Phil. Trans. **A160**, 277 (1870).
[6] H. Hugoniot, J. de l'école polyt. **57**, 3 (1887); **58**, 1 (1888).
[7] Lord Rayleigh, Proc. Roy. Soc. **A84**, 247 (1910). This paper gives a full discussion of earlier work.
[8] J. G. Kirkwood and H. A. Bethe (1941).
[9] F. M. Osborne and A. H. Taylor, Phys. Rev. **70**, 322 (1946).

exact Hugoniot curve for the fluid and in this respect is superior to previous treatments of the shock wave in air which have been based upon ideal gas adiabatics with constant heat capacity,[10] an approximation which fails badly near the explosive source.

THE PROPAGATION EQUATIONS

In discussing the propagation of one-dimensional shock waves, it is convenient to write the equations of hydrodynamics in the form,

$$\frac{\rho r^\alpha}{\rho_0 R^\alpha}\frac{\partial u}{\partial R}+\frac{\alpha u}{r}=-\frac{1}{\rho c^2}\frac{\partial p}{\partial t},$$

$$\frac{R^\alpha}{r^\alpha}\frac{\partial u}{\partial t}=-\frac{1}{\rho_0}\frac{\partial p}{\partial R}, \tag{1}$$

$$u=\left(\frac{\partial r}{\partial t}\right)_R,$$

where u is the particle velocity, p the pressure in excess of the pressure p_0 of the undisturbed fluid, ρ the density, ρ_0 the density of the undisturbed fluid, t the time, and r the Euler coordinate at time t of an element of fluid with Lagrange coordinate R. The Euler sound velocity c is equal to $[(\partial p/\partial\rho)_S]^{\frac{1}{2}}$. The coefficient α takes on the values,

$\alpha=0$ for a plane wave,
$\alpha=1$ for a cylindrical wave,
$\alpha=2$ for a spherical wave.

Equations (1) are supplemented by the equation of state of the fluid and the entropy transport equation $\partial S/\partial t=0$, the latter of which we shall not explicitly use. Equations (1) are of a hybrid form in that we use the Lagrange coordinates R and t as independent variables but retain the Euler equation of continuity. Equations (1) are to be solved subject to initial conditions specified on a curve in the R, t-plane and to the Rankine[5]-Hugoniot[6] conditions at the shock front,

$$\begin{aligned} p&=\rho_0 u U,\\ \rho(U-u)&=\rho_0 U,\\ \Delta H&=(p/2)(1/\rho_0+1/\rho),\end{aligned} \tag{2}$$

where ΔH is the specific enthalpy increment experienced by the fluid in traversing the shock front and U is the velocity of the shock front. Equations (2) constitute supernumerary boundary conditions which are compatible with the differential equations and specified initial conditions only if the shock front follows an implicitly prescribed curve $R_0(t)$ in the R, t-plane.

We denote a derivative in which the shock front is stationary by

$$\frac{d}{dR}=\frac{\partial}{\partial R}+\frac{1}{U}\frac{\partial}{\partial t}. \tag{3}$$

If the operator d/dR is applied to the first of Eqs. (2) and if Eqs. (1) are specialized for the shock front, $r=R$, three relations are obtained between the four partial derivatives $\partial p/\partial t$, $\partial p/\partial R$, $\partial u/\partial t$, $\partial u/\partial R$.

$$\begin{aligned} \frac{\rho}{\rho_0}\frac{\partial u}{\partial R}+\frac{1}{\rho c^2}\frac{\partial p}{\partial t}+\frac{\alpha u}{R}&=0,\\ \frac{\partial u}{\partial t}+\frac{1}{\rho_0}\frac{\partial p}{\partial R}&=0,\\ \frac{\partial u}{\partial t}+U\frac{\partial u}{\partial R}-\frac{g}{\rho_0}\frac{\partial p}{\partial R}-\frac{g}{\rho_0 U}\frac{\partial p}{\partial t}&=0,\end{aligned} \tag{4}$$

where

$$g=\rho_0 U\frac{du}{dp}=1-\frac{p}{U}\frac{dU}{dp}.$$

All of the coefficients in Eqs. (4) can be expressed as functions of pressure alone by means of the Hugoniot conditions, Eqs. (2), and the equation of state of the fluid. If Eqs. (4) can be supplemented by a fourth relation between the partial derivatives, it would be possible to solve for each of the four derivatives as a function of p and R, and with the aid of Eqs. (3) to formulate an ordinary differential equation,

$$\frac{dp}{dR}=\frac{\partial p}{\partial R}+\frac{1}{U}\frac{\partial p}{\partial t}=F(p,R), \tag{5}$$

for the peak pressure p of the shock wave as a function of the distance R, and in addition to obtain the initial slope, $-1/\theta$, of the Euler

[10] G. I. Taylor, Proc. Roy. Soc. **A186**, 273 (1946).

pressure-time curve of the wave,

$$\frac{1}{\theta}=\frac{1}{p}\frac{\partial p}{\partial t}\frac{a}{p}\frac{\rho}{\rho_0}\frac{\partial p}{\partial R}. \tag{6}$$

The physical basis for the supplementary relation to be established lies in the fact that the non-acoustical decay of waves of finite amplitude is closely associated with the entropy increment experienced by the fluid in passing through the shock front and the accompanying dissipation of energy. As a shock wave passes through a fluid, it leaves in its path a residual internal energy increment in each element of fluid determined by the entropy increment produced in it by the passage of the shock front. As a result, the energy propagated ahead by the shock wave decreases with the distance it has traveled from the source.

The adiabatic work w_0 per unit area of initial generating surface done on the fluid exterior to the surface is given by

$$w_0 a_0{}^\alpha=\int_{a_0}^{R}\rho_0 r_0{}^\alpha E[p(r_0)]dr_0+\int_{t_0(R)}^{\infty}r^\alpha u'(p'+p_0)dt, \tag{7}$$

where u' and p' denote particle velocity and excess pressure behind the shock front (the unprimed quantities being reserved henceforth for quantities at the shock front), $t_0(R)$ is the time of arrival of the shock front at R, $E(p)$ is the specific energy increment of the fluid at pressure p_0 and for an entropy increment corresponding to shock front pressure p, and a_0 is the Lagrange coordinate of the generating surface of the shock wave. Now,

$$\int_{t_0(R)}^{\infty}p_0 r^\alpha u'dt=p_0\Delta V+p_0\int_{a_0}^{R}\left(\frac{\rho_0}{\rho}-1\right)r_0{}^\alpha dr_0, \tag{8}$$

where ρ is the final density of the fluid and ΔV is the volume swept out by the generating surface per unit area of initial generating surface. Combining Eqs. (7) and (8) and introducing $h(p)=E+p_0\Delta(1/\rho)$, the specific enthalpy increment of an element of fluid traversed by a shock wave of peak pressure p after return to pressure p_0 along its new adiabatic, one obtains

$$w_0 a_0{}^\alpha=p_0\Delta V+\int_{a_0}^{R}\rho_0 r_0{}^\alpha h[p(r_0)]dr_0+\int_{t_0(R)}^{\infty}r^\alpha u'p'dt. \tag{9}$$

The time integral may be assumed to vanish at $R=\infty$. If one subtracts from Eq. (9) the expression obtained from that equation at $R=\infty$, there results the relation,

$$D(R)=\int_{t_0(R)}^{\infty}r^\alpha u'p'dt, \tag{10}$$

where

$$D(R)=\int_{R}^{\infty}\rho_0 r_0{}^\alpha h[p(r_0)]dr_0. \tag{11}$$

The energy of the shock wave at the point R is by definition the work done on the fluid exterior to R. Thus, the shock wave energy at R per unit area of initial generating surface is given by the quantity $a_0{}^{-\alpha}D(R)$.

Our dissipation assumption breaks down if the first shock wave can be overtaken by second shocks built up in its rear. This will not be the case if the pressure-time curve is initially monotone, decreasing with asymptotic value p_0. If the excess pressure p' has a negative phase, a second shock will develop in the negative part of the pressure-time curve but cannot overtake the initial positive shock. In this case, our theory will apply to the positive phase if the time integrals of Eqs. (7) to (10) are extended not to infinity but to the time at which the excess pressure in the positive phase vanishes. The general theory of shock waves is not sufficiently developed to permit one to say that there is proof for these statements, but they can nevertheless be accepted with some assurance as plausible.

The energy-time integral can be expressed in reduced form,

$$D(R)=R^\alpha p u\mu\nu,$$

$$\frac{1}{\mu}=-\left(\frac{\partial\log p'u'r^\alpha}{\partial t}\right)_{t=t_0(R)}=\frac{1}{p}\frac{\partial p}{\partial t}\frac{1}{u}\frac{\partial u}{\partial t}\frac{\alpha u}{R}, \tag{12}$$

$$\nu=\int_0^{\infty}f(R,\tau)d\tau,\quad \tau=\frac{t-t_0(R)}{\mu},$$

$$f(R,\tau)=r^\alpha p'u'/R^\alpha p u.$$

The function $f(R, \tau)$ is the energy-time integrand, normalized by its peak value $R^{\alpha}pu$ at the shock front, expressed as a function of R and a reduced time τ which normalizes its initial slope to -1 if μ does not vanish. We also assume f to be a monotone decreasing function of τ. Elimination of μ between the first two of Eqs. (12) yields the desired fourth relation supplementing Eqs. (4) between the partial derivatives at the shock front. This set is exact, involving integrals of Eqs. (1) for the knowledge of the reduced energy-time function $f(R, \tau)$. However, if $f(a_0, \tau)$ is initially a monotone decreasing function of τ, $f(R, \tau)$ will remain so, and in fact will at large R become asymptotically a quadratic function of τ corresponding to the linear form of the pressure-time curve that has been shown[8] to be stable at large distances. This means that ν is a very slowly varying function of R, for which sufficiently accurate estimates for many purposes can be made without explicit integration of the hydrodynamic equations. The assignment of a value independent of R to ν is equivalent to imposing a similarity restraint on the energy-time curve. This type of approximation is equivalent in principle to that underlying the Rayleigh-Ritz method, although we do not include a variational procedure to carry the result to any desired degree of approximation.

The initial pressure-time and energy-time curves of an explosion wave are rapidly decreasing. An expansion of the logarithm of the function in a Taylor series in the time, the well-known peak approximation, is appropriate for an initial estimate of ν. This corresponds to an exponential $f(\tau)$,

$$f(\tau) = e^{-\tau},$$

and results in the value, $\nu = 1$. For the asymptotic quadratic energy-time curve, corresponding to a linear pressure-time curve of the positive phase of the wave,

$$f(\tau) = (1-\tau/2)^2, \quad \tau \leqslant 2,$$
$$f(\tau) = 0, \quad \tau > 2,$$

which leads to the value, $\nu = \frac{2}{3}$. As a convenient empirical interpolation formula between the two extreme values, we have employed the relation,

$$\nu = 1 - \tfrac{1}{3} \exp -[p'/p_0] \qquad (13)$$

in a series of calculations[11] of the peak pressure distance curves of shock waves from explosive sources.

Elimination of μ between the first two of Eqs. (12) and combination with Eq. (4) yields a set of four equations which may be solved for the four partial derivatives, and an ordinary differential equation for the peak pressure p as a function of the distance R may be formulated with the aid of Eq. (5). A second ordinary differential equation relating D to R may be obtained by differentiation of Eq. (11). The resulting expressions may be written in the form,

$$\frac{dD}{dR} = -R^{\alpha}L(p),$$
$$\frac{dp}{dR} = -\nu\frac{R^{\alpha}p^2}{D}M(p) - \frac{\alpha p}{2R}N(p), \qquad (14)$$

where

$$L(p) = \rho_0 h(p),$$
$$M(p) = \frac{1}{\rho_0 U^2}\frac{G}{2(1+g)-G},$$
$$N(p) = \frac{4(\rho_0/\rho)+2(1-\rho_0/\rho)G}{2(1+g)-G},$$
$$G = 1-(\rho_0 U/\rho c)^2, \quad g = 1-\frac{p}{U}\frac{dU}{dp}.$$

The functions $L(p)$, $M(p)$, and $N(p)$ can be evaluated as functions of the pressure by means of the equation of state of the fluid and the Hugoniot relations, Eqs. (2). It may be remarked that Eqs. (14) are independent of any assumption regarding the equation of state of the fluid and that they take proper account of the finite entropy increment of the fluid produced by the passage of the shock.

The functions $L(p)$, $M(p)$, and $N(p)$ are most conveniently expressed as functions of the pressure in tabular form, and they may be evaluated by numerical methods from a tabular presentation of the exact Hugoniot curves for the fluid. Equations (14) can then be integrated numerically by the use of standard methods.[12]

[11] J. G. Kirkwood and S. R. Brinkley, Jr. (1945).

[12] See, for example, J. B. Scarborough, *Numerical Mathematical Analysis* (Johns Hopkins Press, Baltimore, 1930), pp. 218 ff.

THE ASYMPTOTIC PROPAGATION EQUATIONS

It is of interest to examine the asymptotic form of the solutions of Eqs. (14) for small excess pressure p. If the exterior medium is air, the ideal adiabatic equation of state, $p=p_0[(\rho/\rho_0)^\gamma-1]$, may be employed in the limit of small excess pressure, where γ is the ratio of the heat capacities of p_0 and at the temperature of the undisturbed fluid. Employing the acoustic approximation in the evaluation of the limiting shock wave velocity, it is easy to show that

$$\begin{aligned}
&\mathrm{Lim}(p\to 0)L(p)=\frac{\gamma+1}{12\gamma^2}\frac{p^3}{{p_0}^2},\\
&\mathrm{Lim}(p\to 0)M(p)=\frac{\gamma+1}{8\gamma^2}\frac{p}{{p_0}^2},\\
&\mathrm{Lim}(p\to 0)N(p)=1,\\
&\mathrm{Lim}(p\to 0)\nu=\tfrac{2}{3},
\end{aligned}\tag{15}$$

and the asymptotic equations are

$$\begin{aligned}
&\frac{dD}{dR}=-\frac{\gamma+1}{12\gamma^2}\frac{R^\alpha p^3}{{p_0}^2},\\
&\frac{dp}{dR}+\frac{\alpha p}{2R}=-\frac{\gamma+1}{12\gamma^2}\frac{R^\alpha p^4}{D{p_0}^2}.
\end{aligned}\tag{16}$$

Equations (16) have the solutions,

$$\begin{aligned}
&Rp=P_1(\log R/R_1)^{-\frac{1}{4}},\\
&D=[(\gamma+1)/6\gamma^2{p_0}^2]{P_1}^2Rp,
\end{aligned}\tag{17a}$$

for the spherical wave, $\alpha=2$,

$$\begin{aligned}
&\sqrt{R}p=P_1[2(\sqrt{R}-\sqrt{R_1})]^{-\frac{1}{4}}\\
&D=[(\gamma+1)/6\gamma^2{p_0}^2]{P_1}^2\sqrt{R}p,
\end{aligned}\tag{17b}$$

for the cylindrical wave, $\alpha=1$, and

$$\begin{aligned}
&p=P_1(R-R_1)^{-\frac{1}{4}},\\
&D=[(\gamma+1)/6\gamma^2{p_0}^2]{P_1}^2p,
\end{aligned}\tag{17c}$$

for the plane wave, $\alpha=0$, where P_1 and R_1 are constants. Equations (15) to (17) are valid when the exterior medium is water if, in these expressions, the pressure p_0 is replaced by the characteristic pressure B of the Tait[13] equation of state, which may be written for use along an adiabatic in the form $p=B[(\rho/\rho_0)^\gamma-1]$, and γ is interpreted not as the heat capacity ratio but as the exponent of ρ/ρ_0 in the Tait equation. The asymptotic form for the peak pressure of the shock wave with spherical symmetry is in agreement with the results of the theories of Kirkwood and Bethe[8] and with the limiting theory of Osborne and Taylor.[9] The pressure, in this case, decays non-acoustically as the slowly varying factor $(\log R/R_1)^{-\frac{1}{4}}$.

[13] R. E. Gibson, J. Am. Chem. Soc. **56**, 4 (1934); **57**, 284 (1935). See also A. Wohl, Zeits. f. physik. Chemie **99**, 234 (1921), and H. Carl, *ibid.* **101**, 238 (1922).

THE IMPULSE

The impulse I delivered by the shock wave at a point of fixed Euler coordinate r is

$$I=\int_{t_0(R)}^{\infty}p'dt \tag{18}$$

along a path of constant r. If the excess pressure p' has a negative phase, the positive impulse is obtained if the time integral is extended not to infinity but to the time at which the excess pressure vanishes. The pressure-time integral can be expressed in reduced form in a manner analogous to the reduction of Eq. (10).

$$\begin{aligned}
&I=\nu^*p\theta,\\
&\frac{1}{\theta}=-\left(\frac{\partial\log p'}{\partial t}\right)_{r,\,t=t_0(R)},\\
&\nu^*=\int_0^{\infty}(p'/p)d\tau^*,\quad \tau^*=\frac{t-t_0(R)}{\theta}.
\end{aligned}\tag{19}$$

The initial slope, $-1/\theta$, of the Euler pressure-time curve is expressed in terms of the Lagrange partial derivatives at the shock front by Eq. (6), and these partial derivatives were obtained as functions of peak pressure by the solution of Eqs. (4) and (12). The following expression is obtained for θ:

$$-\frac{1}{\theta}=\frac{U}{G}\left\{\frac{\alpha}{R}+\left[\frac{\rho}{\rho_0}(1+g)+\left(1-\frac{\rho}{\rho_0}\right)G\right]\frac{1}{p}\frac{dp}{dR}\right\}. \tag{20}$$

For an exponential pressure-time curve, consistent with the peak approximation and the exponential energy-time curve, the reduced

pressure-time integral ν^* is equal to 1. For the asymptotic linear pressure-time curve, consistent with the asymptotic quadratic energy-time curve, we have $\nu^* = \frac{1}{2}$ for the positive phase of the wave. As an empirical interpolation formula between the two values, we have employed the relation,[11]

$$\nu^* = 1 - \tfrac{1}{2} \exp - [p/p_0]^{\frac{1}{2}}. \tag{21}$$

We have found that Eq. (21) leads to satisfactory agreement between calculated and experimental values of the positive impulse when used in conjunction with Eq. (13) for the reduced energy-time integral. A more detailed analysis of the relation between ν and ν^* does not seem justified in view of the empirical nature of Eq. (13).

INITIAL CONDITIONS FOR SHOCK WAVES FROM EXPLOSIVE SOURCES

The two constants of integration may be determined from the thermodynamic properties of the explosive and those of its products, either in the Chapman-Fouget detonation state or in the instantaneous detonation state corresponding to adiabatic isometric conversion of the entire explosive charge to its decomposition products. Since the instantaneous detonation state may be expected to give the better average representation of the behavior of the detonation products in the generation of a shock wave in an exterior medium, we shall employ it in the discussion of the initial conditions for the shock wave.

If at the initial instant of time, a charge of explosive has been converted to products at a uniform pressure p_s, a shock wave will advance into the exterior medium and a rarefaction wave will recede into the detonation products. The initial excess pressure p_1, and particle velocity u_1, continuous at the boundary, are related by

$$\sigma^*(p_1) + u_1 = 0, \quad u = p/\rho_0 U(p), \qquad \sigma^*(p) = (s^*) \int_{p_e}^{p+p_0} \frac{dp}{\rho^* c^*}, \tag{22}$$

where σ^* is the Riemann[4] function in the explosion products and U, the shock velocity in the exterior medium, is determined as a function of the pressure by the Hugoniot conditions, Eqs. (2). The asterisked quantities refer to the explosion products. The first of Eqs. (22) expresses the fact that the Riemann r-function[4] initially vanishes in the receding rarefaction wave. In order to solve Eqs. (22), it is necessary to use the Hugoniot tables for the exterior medium, the energy of explosion, and the heat capacities and equilibrium constants for the substances making up the explosion products; and to evaluate σ^* it is necessary to use an equation of state for those products.

In the development of the propagation equations, the rate of energy delivery has been approximated by an exponential function of time. For shock waves in air, it may be assumed that the integral of this exponential function is equal to the total energy of explosion, since experimental evidence suggests that there is little residual energy available for second shocks. For shock waves in water, experimental evidence suggests that approximately one-half of the energy of explosion is delivered to the first shock. The initial value of the quantity D is readily estimated from these considerations, and the disadvantages of the approximate nature of this procedure are minimized by the circumstance that except in the immediate vicinity of the explosive charge, the shock wave parameters are not very sensitive to the initial energy.

A Method for Obtaining Electronic Eigenfunctions and Eigenvalues in Solids with An Application to Sodium*

FRED C. VON DER LAGE** AND H. A. BETHE
Cornell University, Ithaca, New York

(Received January 13, 1947)

As in the Wigner-Seitz and Slater cellular approximation it is assumed that the valence electron potential is spherically symmetrical within a lattice cell. Then the Schrödinger equation becomes separable in spherical coordinates so that the eigenfunction can be expanded in terms which are products of spherical harmonics and solutions to the radial equation. The method differs from the previous ones in that: (1) eigenfunctions belonging to special wave vectors are first constructed by suitable linear combinations of spherical harmonics so as to satisfy symmetry requirements and thus, essentially, including more terms in the expansion without increase in labor and (2) surface boundary conditions are satisfied exactly, in effect, at points which are more representative of the cell surface. The method was tested by applying it to the Shockley empty lattice (body centered cubic) for which the eigenvalues are known exactly. The lowest four eigenvalues belonging to the reduced wave vector (0,0,0) and the lowest three belonging to $(0,0,\pi/a)$ showed errors of one percent or less in energy using from two to four terms in the eigenfunction expansion. When applied to sodium results showed that electrons in the first few Brillouin zones are indeed very nearly free, having free electron energies within a few percent even at points near the center and corners of reduced wave vector space. Furthermore on the boundary of reduced wave vector space in the (0,0,1) direction there is no energy gap between the first and second Brillouin zone eigenvalues since they "stick together" at that and equivalent points.

INTRODUCTION

IN the W–S[1,2] cellular method because of the periodicity of the electron-potential it suffices to focus attention upon a single cell of the crystal lattice. Schrödinger one-electron solutions for the valence electrons are sought satisfying the *BC* (cell boundary conditions) imposed by symmetry and periodicity. The interactions of valence electrons with nuclei and core electrons of the cell are represented in this approximation by an ordinary, appropriately chosen, potential V. Because of high symmetry and the essentially neutral electrical nature of surrounding cells, their contribution to this potential is assumed to be zero.

In the interest of mathematical simplicity and justified[1,2] on grounds of high symmetry the potential, V, is assumed to have spherical symmetry within a cell. The Schrödinger equation then becomes separable in polar coordinates and the one-electron eigenfunction, ψ, can be expressed as

$$\psi=\Sigma_l A_l[\Sigma_m C_{lm} Y_l^m(\phi,\theta)]R_l(E,\rho) \qquad (1)$$

where the Y_l^m are *SH* (surface spherical harmonics), and the $R_l(E,\rho)$ are the solutions to the radial equation with an energy parameter, E. The constant coefficients A_l, C_{lm} and the energy parameter E can all be chosen in principle so as to fit the appropriate *BC* at the surface of the cell. (The split between A_l and C_{lm} is of course largely arbitrary but convenient for some of the following.)

The labor without limit implied in (1) was reduced by Slater[3] to practical limits by the approximation of assuming all C_{lm}'s to be zero for l greater than a certain fixed value. Then, of course, the *BC* cannot be fitted over the entire surface of the *LC*. Slater therefore selects certain points on the surface of the *LC* at which he satisfies the *BC* by appropriate choice of the C_{lm}'s which are not assumed zero. The fitting is done in this way for any arbitrary wave vector[4] $\mathbf{k}$. However, Shockley[5] has shown that Slater's procedure leads to large errors for an empty

* The method and results were presented in condensed form at the New York Meeting of the American Physical Society, January 14–15, 1944.

** Now at the Clinton Laboratories, Oak Ridge, Tennessee.

[1] A. Sommerfeld and H. Bethe, "Electronentheorie der Metalle," *Handbuch der Physik* (Verlagsbuchhandlung, Julius Springer, Berlin, 1933), Vol. 24/2; F. Seitz, *Modern Theory of Solids* (McGraw-Hill Book Company, Inc., New York, 1940); N. F. Mott and H. Jones, *Theory of Properties of Metals and Alloys* (Oxford Press, New York, 1936).

[2] E. Wigner and F. Seitz, Phys. Rev. **43**, 804 (1933) and **46**, 509 (1934).

[3] J. C. Slater, Phys. Rev. **45**, 794 (1934).

[4] It is assumed that these eigenfunctions, ψ, have been brought into the Bloch form *viz.* $\psi=u_{\mathbf{k}}(\varrho)\exp i\mathbf{k}\cdot\varrho$ where $\mathbf{k}$ is a reduced wave vector and $u_{\mathbf{k}}(\varrho)$ is periodic with the period of the crystal lattice.

[5] W. Shockley, Phys. Rev. **52**, 866 (1937).

lattice for which the value of the energy E as a function of $\mathbf{k}$ is known. He concluded that a much larger number of C_{lm}'s will have to be used than was done in Slater's calculations.

It is the aim of this paper to include C_{lm}'s up to much larger l's without increasing the labor. This can be done for eigenfunctions belonging to certain points in $\mathbf{k}$ space (reduced wave vector space) of especially high symmetry, i.e., points having the complete symmetry of the cubic lattice, or lying on symmetry lines or planes. The symmetry of the wave functions at such special points in $\mathbf{k}$ space was discussed by BSW.[6] Our method consists now of constructing, once and for all, combinations $\Sigma_m C_{lm} Y_l^m$ which have the correct symmetry required according to BSW; these we call Kubic Harmonics (KH). Then choice of the A_l in (1) serves to fit the BC; note that the BC need to be fitted only on a few of the surfaces of the LC, symmetry then makes them automatically satisfied on a number of other surfaces. By using only 3 or 4 different A_l's we can generally include values of l up to 6 which would require 49 coefficients C_{lm} in Slater's method.

Actual calculations in the present work were confined to the specially symmetrical points $\mathbf{k}=(0,0,0)$ and $\mathbf{k}=(0,0,\pi/a)$ of $\mathbf{k}$-space belonging to the body centered cubic lattice. The method was tested by applying it to the limiting concept of Shockley's[5] empty lattice for which the value of the energy E is known. For the eigenfunctions tested, the results of the ELT (empty lattice test) were encouraging beyond expectation; the corresponding eigenfunctions and energies were therefore obtained for sodium.

METHOD OF CONSTRUCTING EIGENFUNCTIONS: KUBIC HARMONICS

For any distinct wave vector[7] $\mathbf{k}$, there is a certain group of symmetry operations on the coordinates which do not change $\mathbf{k}$. This "group of $\mathbf{k}$" is the full cubic symmetry group for the two values of $\mathbf{k}$ here considered, (0,0,0) and $(0,0,\pi/a)$. The eigenfunctions can then be classified according to the irreducible representation of the group of $\mathbf{k}$ which describes their transformation under the symmetry operations of the group; each irreducible representation represents a "type." For the cubic group, for instance, there are 10 different types (see below). For each type, we can find various "sets" of KH which transform according to the representation characteristic of the type. By a set we mean functions which transform into each other by the symmetry operations of the group of $\mathbf{k}$. A set will contain only functions of the same order l, and of course of the same type. Not all types occur for a given l, nor all l's for a given type.

It is the aim now to show how each correct linear combination of spherical harmonics $\Sigma_m C_{lm} Y_l^m$ belonging to a type, for each order l in which the type occurs, may be constructed. This construction proceeds in three steps: (1) constructing a "group table" showing the behavior of each type under transformation of each element of the group of $\mathbf{k}$, i.e., whether the element of the type is unchanged, designated by $+$, or changed in sign only, $-$, or whether it is transformed into a linear combination of other members of its type, 0. (2) constructing "characteristic polynomials," CP, in x, y, z for each type and order l which have the transformation properties of the group table constructed above, and (3) deriving the correct linear combinations of the SH by dividing the CP by $\rho^l=(x^2+y^2+z^2)^{l/2}$ and orthonormalizing. This process is carried out below for the types belonging to wave vectors (0,0,0) and $(0,0,\pi/a)$ of the body-centered cubic lattice. These correct linear combinations for these wave vectors are the KH sought.

The group of these wave vectors is the full cubic symmetry group.[6] It consists of 48 elements, 24 rotations forming a normal divisor, N, and these 24 rotations followed by inversion about the center forming a coset, JN. N and JN each contain five classes and, therefore, there are 10 irreducible representations and ten types of KH α, β, γ, δ, ϵ, and α', β', γ', δ', ϵ' corresponding to the five "positive" irreducible representations Γ_1, Γ_2, Γ_3, Γ_4, Γ_5, and the five "negative" irreducible representations Γ_1', Γ_2', Γ_3', Γ_4', Γ_5', with dimensions 1, 1, 2, 3, 3, respectively.

It is useful to know the type of KH and the number of sets of a type that can be constructed

[6] L. Bouchaert, R. Smoluchowski and E. Wigner, Phys. Rev. **50**, 58 (1936).

[7] For the meanings of "distinct $\mathbf{k}$" and "group of $\mathbf{k}$" the reader is referred to BSW, reference 6.

TABLE I. Group Table. Behavior of Kubic Harmonic types under operations of the Cubic Symmetry Group. Plus indicates invariance under the element; minus means change of sign only; zero indicates change to one of the other functions with which the given function is degenerate. If the type is degenerate the behavior of that function is listed which has the z axis as a unique axis.

1 Class	2 Operation	3 Rotation	4 α	5 α'	6 β	7 β'	8 γ	9 γ'	10 δ	11 δ'	12 ϵ	13 ϵ'
E	$x\ y\ z$	none	+	+	+	+	+	+	+	+	+	+
C_2	$-x\ -y\ z$	z through π	+	+	+	+	+	+	+	+	+	+
	$x\ -y\ -z$	x through π	+	+	+	+	+	+	−	−	−	−
	$-x\ y\ -z$	y through π	+	+	+	+	+	+	−	−	−	−
C_3	$-y\ x\ z$	z through $+\pi/2$	+	+	−	−	+	+	+	+	−	−
	$y\ -x\ z$	z through $-\pi/2$	+	+	−	−	+	+	+	+	−	−
	$x\ -z\ y$	x through $\pi/2$	+	+	−	−	0	0	0	0	0	0
	$x\ z\ -y$	x through $-\pi/2$	+	+	−	−	0	0	0	0	0	0
	$z\ y\ -x$	y through $\pi/2$	+	+	−	−	0	0	0	0	0	0
	$-z\ y\ x$	y through $-\pi/2$	+	+	−	−	0	0	0	0	0	0
C_4	$y\ x\ -z$	$x=y$ through π	+	+	−	−	+	+	−	−	+	+
	$z\ -y\ x$	$x=z$ through π	+	+	−	−	0	0	0	0	0	0
	$-x\ z\ y$	$y=z$ through π	+	+	−	−	0	0	0	0	0	0
	$-y\ -x\ -z$	$x=-y$ through π	+	+	−	−	+	+	−	−	+	+
	$-z\ -y\ -x$	$x=-z$ through π	+	+	−	−	0	0	0	0	0	0
	$-x\ -z\ -y$	$y=-z$ through π	+	+	−	−	0	0	0	0	0	0
C_5	$z\ x\ y$	$x=y=z$ through $+2\pi/3$	+	+	+	+	0	0	0	0	0	0
	$y\ z\ x$	$x=y=z$ through $-2\pi/3$	+	+	+	+	0	0	0	0	0	0
	$z\ -x\ -y$	$x=-y=z$ through $+2\pi/3$	+	+	+	+	0	0	0	0	0	0
	$-y\ -z\ x$	$x=-y=z$ through $-2\pi/3$	+	+	+	+	0	0	0	0	0	0
	$-z\ -x\ y$	$x=-y=-z$ through $2\pi/3$	+	+	+	+	0	0	0	0	0	0
	$-y\ z\ -x$	$x=-y=-z$ through $-2\pi/3$	+	+	+	+	0	0	0	0	0	0
	$-z\ x\ -y$	$x=y=-z$ through $2\pi/3$	+	+	+	+	0	0	0	0	0	0
	$y\ -z\ -x$	$x=y=-z$ through $-2\pi/3$	+	+	+	+	0	0	0	0	0	0
J	$-x\ -y\ -z$	none	+	−	−	+	+	−	−	+	+	−
JC_2	$x\ y\ -z$	z through π	+	−	−	+	+	−	−	+	+	−
	$-x\ y\ z$	x through π	+	−	−	+	+	−	+	−	−	+
JC_3	$y\ -x\ -z$	z through $\pm\pi/2$	+	−	+	−	+	−	+	−	−	+
	$-x\ z\ -y$	x through $\pm\pi/2$	+	−	+	−	0	0	0	0	0	0
JC_4	$-y\ -x\ z$	$x=y$ through π	+	−	+	−	+	−	+	−	+	−
	$-z\ y\ -x$	$x=z$ through π	+	−	+	−	0	0	0	0	0	0
JC_5	$-z\ -x\ -y$	$x=y=z$ through $2\pi/3$	+	−	−	+	0	0	0	0	0	0

for each order l. One of us[8] has derived this and the results are: for: $l=0$, one α type; $l=1$, one δ; $l=2$, one each of γ and ϵ; $l=3$, one each of β, δ, ϵ'; $l=4$, one each of α, γ, ϵ, δ'; $l=5$, one each of γ', ϵ' and two δ; $l=6$, one each of α, γ, β', δ' and two ϵ.

Construction of the Group Table

The behavior of each type of KH under the transformations of the crystal group is shown (for one function of a set of each type) in Table I. This is obtained by a study of the lower order SH using the above results as a guide. For $l=0$ there is the non-degenerate type α and there is one SH which is spherically symmetrical and remains invariant under all transformations. The behavior of this type is shown in column 4. For $l=1$ there is the triply-degenerate δ type. The three SH are x/ρ, y/ρ, z/ρ. The latter one transforms according to column 10, and only into either itself or one of the remaining two SH. For $l=2$ there are the doubly degenerate γ type and the triply degenerate ϵ type. The SH are $[z^2-1/2(x^2+y^2)]/\rho^2$; $(y^2-x^2)/\rho^2$; zx/ρ^2, zy/ρ^2 and xy/ρ^2. The behavior of the first of these is shown in column 8. In those cases in which it does not transform into itself it transforms only into a linear combination of itself and the second listed

[8] H. Bethe, Ann. d. Physik **3**, 133 (1929).

above. It is therefore double degenerate and is identified with the γ type. The behavior of xy/ρ^2 is shown in column 12; it is degenerate with the remaining two, and is identified with the ϵ type. For $l=3$, there is among others the non-degenerate β type. Among the *SH* of $l=3$ there is found the function xyz/ρ^3. This obviously satisfies the requirements for a non-degenerate function and its behavior is listed in column 6. The remainder of the table corresponding to the behavior of the α', β', γ', δ', ϵ' types can now be determined with ease by observing that their behavior differs only in sign from corresponding unprimed types whenever an inversion is involved.

Construction of Characteristic Polynomials

For this purpose it is noted that any power of ρ is invariant under the transformation of each element of the cubic group. Thus not only the *SH* x/ρ, y/ρ, z/ρ form functions of type δ but also the first order polynomials x, y, z or the third order polynomials $x\rho^2$, $y\rho^2$, $z\rho^2$. All sets which differ only by a power of ρ are therefore considered "identical" for the present purposes.

The problem of constructing *CP* is the problem of finding linear combinations of terms of the form $x^py^qz^r$ $(l=p+q+r)$ which are linearly independent of other chosen polynomials of the same order (or identical polynomials of lower order) and which behave according to their type (Table I). The results of reference 8 quoted above aids in pointing out types for which a search is instituted.

As an example, the procedure for obtaining the *CP* of order four is briefly outlined, assuming *CP* of lower order have already been obtained. This order contains one set each of types α, γ, ϵ and δ'. These are nine linearly independent functions to be constructed from the fifteen linearly independent polynomials: three of form x^4, six of form xy^3, three of form x^2yz, and three of form x^2y^2. However, these fifteen are effectively reduced to nine because of the six fourth order polynomials obtained by multiplying identical lower order polynomials by powers of ρ^2 *viz*:

α type, P_1: ρ^4,
γ type, P_2: $\rho^2(x^2-y^2)$, $\rho^2(y^2-z^2)$,
ϵ type, P_3: ρ^2xy, ρ^2yz, ρ^2zx.

With an eye on the Table I there are constructed the following:

Polynomials obviously of the α type

P_4: $x^4+y^4+z^4$
P_5: $x^2y^2+y^2z^2+z^2x^2$ is not new but is equal to $\frac{1}{2}(P_1-P_4)$

Polynomials of γ type

P_6: x^4-y^4, y^4-z^4
P_7: $(x^2-y^2)z^2$, $(y^2-z^2)x^2$ not new *viz*. P_2-P_6

Polynomials of ϵ type

P_8: xyz^2, yzx^2, zxy^2
P_9: x^3y+xy^3, y^3z+yz^3, z^3x+zx^3 not new *viz*. P_3-P_8

Polynomials of the δ' type

P_{10}: x^3y-xy^3, y^3z-yz^3, z^3x-zx^3

These exhaust the possible number of fourth order linearly independent functions. The three fourth powers are exhausted in the three function P_4 and P_6, the six of form x^3y in P_9 and P_{10}, the three of form x^2yz in P_8, and the three of form x^2y^2 in P_5 and P_7.

Construction of Kubic Harmonics from the Characteristic Polynomials

Dividing the *CP* of order l by ρ^l yields functions of the angles alone. These functions, F_{ls}, have the correct symmetry properties of type s but do not obey Legendre's differential equation of order l. However, from their nature it follows that they are linear combinations of *SH* of order l and lower. In order to eliminate all lower order harmonics F_{ls} can be made orthogonal to all *SH* of order less than l. Because of the orthogonality of functions belonging to different irreducible representations, it is only necessary to make F_{ls} orthogonal to all *KH* of type s and lower l. This is done by expanding F_{ls} in terms of *KH* of the same type and orders l and lower, and obtaining the *KH*, K_{ls}, in the usual way. One of us[9] has obtained all the *KH* up to $l=6$; these are listed in Table II.

[9] H. A. Bethe, unpublished paper (1935).

TABLE II. List of the Kubic Harmonics classified according to symmetry properties. All functions normalized to 4π. Factors of ρ^{-l} are omitted throughout, i.e., x, y, z are written for x/ρ, y/ρ, z/ρ. Functions in square brackets indicate functions with normalization factors omitted.

type α

$$\alpha_0 = 1$$

$$\alpha_4 = \frac{5(3\cdot 7)^{\frac{1}{2}}}{4}\left(x^4+y^4+z^4-\frac{3}{5}\rho^4\right)$$

$$\alpha_6 = \frac{3\cdot 7\cdot 11(2\cdot 13)^{\frac{1}{2}}}{8}\left(x^2y^2z^2+\frac{1}{22}[\alpha_4]\rho^2-\frac{1}{105}\rho^6\right)$$

$$\alpha_8 = \frac{5\cdot 13(3\cdot 11\cdot 17)^{\frac{1}{2}}}{16}\left(x^8+y^8+z^8-\frac{28}{5}[\alpha_6]\rho^2-\frac{210}{143}[\alpha_4]\rho^4-\frac{1}{6}\rho^8\right)$$

type β

$$\beta_3 = (3\cdot 5\cdot 7)^{\frac{1}{2}}xyz$$

$$\beta_7 = \frac{11(3\cdot 5\cdot 7\cdot 13)^{\frac{1}{2}}}{4}xyz\left(x^4+y^4+z^4-\frac{5}{11}\rho^4\right)$$

type γ

$$(\gamma_2)_1 = 5^{\frac{1}{2}}(z^2-\tfrac{1}{2}(x^2+y^2)); \quad (\gamma_2)_2 = \frac{(3\cdot 5)^{\frac{1}{2}}}{2}(x^2-y^2)$$

$$(\gamma_4)_1 = \frac{7(3\cdot 5)^{\frac{1}{2}}}{2}\left(z^4-\tfrac{1}{2}\left(x^4+y^4\right)-\frac{6}{7}[\gamma_2]_1\rho^2\right); \quad (\gamma_4)_2 = \frac{3\cdot 7(5)^{\frac{1}{2}}}{4}\left(x^4-y^4-\frac{6}{7}[\gamma_2]_2\rho^2\right)$$

$$(\gamma_6)_1 = \frac{11(2\cdot 7\cdot 13)^{\frac{1}{2}}}{4}\left(z^6-\tfrac{1}{2}(x^6+y^6)-\frac{15}{11}[\gamma_4]_1\rho^2-\frac{5}{7}[\gamma_2]_1\rho^4\right);$$

$$(\gamma_6)_2 = \frac{11(2\cdot 3\cdot 7\cdot 13)^{\frac{1}{2}}}{8}\left(x^6-y^6-\frac{15}{11}[\gamma_4]_2\rho^2-\frac{5}{7}[\gamma_2]_2\rho^4\right)$$

type δ†

$$(\delta_1)_s = 3^{\frac{1}{2}}z$$

$$(\delta_3)_s = \frac{5(7)^{\frac{1}{2}}}{2}\left(z^3-\frac{3}{5}z\rho^2\right)$$

$$(\delta_5)_s = \frac{3^2\cdot 7(11)^{\frac{1}{2}}}{8}\left(z^5-\frac{10}{9}[\delta_3]_s\rho^2-\frac{3}{7}[\delta_1]_s\rho^4\right)$$

$$(\delta_5')_s = \frac{3(5\cdot 7\cdot 11)^{\frac{1}{2}}}{2}z\left(x^4+y^4-\frac{3}{4}(x^2+y^2)^2\right)$$

type ϵ

$$(\epsilon_2)_s = (3\cdot 5)^{\frac{1}{2}}xy$$

$$(\epsilon_4)_s = \frac{3\cdot 7(5)^{\frac{1}{2}}}{2}xy\left(z^2-\frac{1}{7}\rho^2\right)$$

$$(\epsilon_6)_s = \frac{3\cdot 11(2\cdot 3\cdot 5\cdot 7\cdot 13)^{\frac{1}{2}}}{16}xy\left(z^4-\frac{6}{11}z^2\rho^2+\frac{1}{33}\rho^4\right)$$

$$(\epsilon_6')_s = \frac{(2\cdot 3\cdot 7\cdot 11\cdot 13)^{\frac{1}{2}}}{2}xy(x^4+y^4-\frac{5}{8}(x^2+y^2)^2)$$

type α'

$$\alpha_9' = \frac{(6\cdot 5\cdot 7\cdot 11\cdot 13\cdot 17\cdot 19)^{\frac{1}{2}}}{8}xyz(x^4(y^2-z^2)+y^4(z^2-x^2)+z^4(x^2-y^2))$$

type β'

$$\beta_6' = \frac{(2\cdot 3\cdot 5\cdot 7\cdot 11\cdot 13)^{\frac{1}{2}}}{8}(x^4(y^2-z^2)+y^4(z^2-x^2)+z^4(x^2-y^2))$$

type γ'

$$(\gamma_5')_1 = (3\cdot 5\cdot 7\cdot 11)^{\frac{1}{2}}xyz(z^2-\tfrac{1}{2}(x^2+y^2)); \quad (\gamma_5')_2 = \frac{3(5\cdot 7\cdot 11)^{\frac{1}{2}}}{2}xyz(x^2-y^2)$$

$$(\gamma_7')_1 = \frac{13(3\cdot 5\cdot 7\cdot 11)^{\frac{1}{2}}}{2}xyz\left(z^4-\tfrac{1}{2}(x^4+y^4)-\frac{10}{13}(z^2-\tfrac{1}{2}(x^2+y^2))\rho^2\right)$$

$$(\gamma_7')_2 = \frac{3\cdot 13(5\cdot 7\cdot 11)^{\frac{1}{2}}}{4}xyz\left(x^4-y^4-\frac{10}{13}(x^2-y^2)\rho^2\right)$$

type δ'

$$(\delta_4')_s = \frac{3(5\cdot 7)^{\frac{1}{2}}}{2}xy(x^2-y^2)$$

$$(\delta_6')_s = \frac{3\cdot 11(7\cdot 13)^{\frac{1}{2}}}{4}xy(x^2-y^2)\left(z^2-\frac{1}{11}\rho^2\right)$$

type ϵ'

$$(\epsilon_3')_s = \frac{(3\cdot 5\cdot 7)^{\frac{1}{2}}}{2}z(x^2-y^2)$$

$$(\epsilon_5')_s = \frac{3(3\cdot 5\cdot 7\cdot 11)^{\frac{1}{2}}}{4}(z^3-\tfrac{1}{3}z\rho^2)(x^2-y^2)$$

† For types δ and ϵ, which are triply degenerate, the other two functions are found by cyclic interchange of coordinates.

BOUNDARY CONDITIONS AT THE SURFACE OF THE CRYSTAL CELL

The *BC* on the surfaces of the crystal cell are fixed by the periodicity of the eigenfunction which in turn is the property of its wave vector. A translation from a point A on one face to the point B perpendicularly opposite on a parallel second face is a translation of a lattice-point vector $\mathbf{T}$. It is well known[6] that $\psi(\rho+\mathbf{T}) = \psi(\rho)\exp i\mathbf{k}\cdot\mathbf{T}$ so that, in general

$$\psi_B = \psi_A \exp i\mathbf{k}\cdot\mathbf{T}. \tag{2}$$

These *BC* can be put into a generally more usable form by employing the symmetry properties (listed in a group table) of the eigenfunction type. For the *KH* this is now done.

The unit crystal cell for the body centered cubic lattice is shown in Fig. 1. It has two non-equivalent face forms: six square faces on planes $x=\pm a$, $y=\pm a$, $z=\pm a$; and eight hexagonal faces whose normal vectors are $(\pm a/2, \pm a/2, \pm a/2)$. The translations between pairs of square faces are $(0,0,2a)$, $(0,2a,0)$, and $(2a,0,0)$ and those between the hexagonal faces are $(\pm a,\pm a,a)$. For the wave vectors $(0,0,0)$ and $(0,0,\pi/a)$ (to which the *KH* belong) the periodicity conditions are particularly simple. From (2) they are:

for $k=0,0,0$ Eigenfunctions are periodic with the periods of all pairs of parallel faces of the cell (3a)

for $k=0,0,\pi/a$ Eigenfunctions are periodic with the period of pairs of square faces (3b)

Eigenfunctions are anti-periodic with the period of pairs of hexagonal faces (3c)

(By "anti-periodic" is here meant that the function changes sign only upon a displacement by the "period" stated.) Correspondingly, eigenfunctions belonging to $\mathbf{k}=0,0,0$ are here said to be periodic; those belonging to $\mathbf{k}=0,0,\pi/a$, anti-periodic.

As an example, the working *BC* are now derived for the anti-periodic δ-type function with z axis preferred. Non-equivalent pairs of faces are considered separately. For the square faces $z=\pm a$: Periodicity, (3a), and symmetry operator $x, y, -z$ (Table I), give successively

$$\psi(x,y,a) = \psi(x,y,-a) = -\psi(x,y,a)$$

so that the eigenfunction vanishes over this face. For the square faces $x=\pm a$ (or $y=\pm a$): Periodicity and symmetry operator $-x, y, z$ gives

$$\psi(a+\epsilon,y,z) = \psi(-a+\epsilon,y,z) = \psi(a-\epsilon,y,z)$$

so that the normal derivative $\partial\psi(a,y,z)/\partial x$, vanishes over this surface. For the hexagonal surfaces $\pm x\pm y+z=\pm(3/2)a$: Anti-periodicity, (3c), and symmetry operator $-y, -x, -z$ gives

$$\psi(x,y,z) = -\psi(x-a,y-a,z-a) = +\psi(a-y,a-x,a-z)$$

so that the function is symmetrical about the line $\zeta=0$ (Fig. 1). Similarly, the normal derivative is anti-symmetric about the same line. Table III lists working *BC* similarly obtained for all types of functions for that function of a type which has its z axis preferred.

Fitting of the Boundary Conditions—Empty Lattice Test

In the notation of Kubic Harmonics the candidates for eigenfunctions (1), have the form

$$\psi_s = \Sigma_{lu} A_{lu} K_{slu} R_l(E,\rho), \tag{4}$$

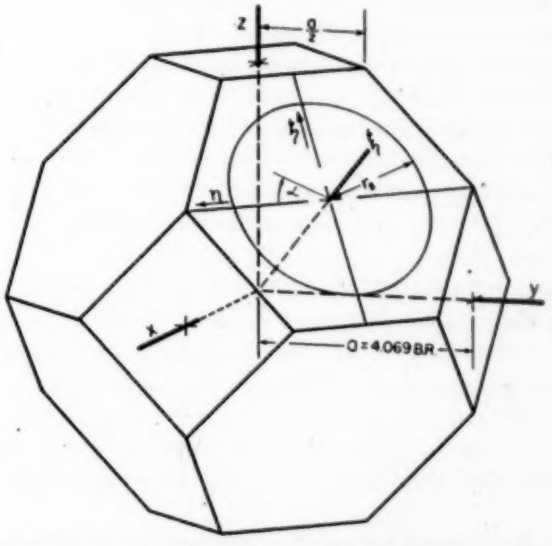

FIG. 1. Unit lattice cell for the cubic body centered crystal lattice. The lattice constant, $2a$, for sodium, is shown as 8.138 Bohr radii. The circle on the hexagonal face is the trace of an equal volume sphere and it was over this circle that the boundary conditions were approximately satisfied.

TABLE III. Boundary conditions on ψ and its normal derivative on the faces of the unit cell. For degenerate types the BC on that eigenfunction is listed which has its z axis preferred. 0 = function vanishes over surface; a = antisymmetric; s = symmetric.

Type	Square faces (Either periodic or antiperiodic functions) $x=\pm a$ (or $y=\pm a$)		$z=\pm a$		Hexagonal faces Symmetry about line $\xi=0$ Periodic		Antiperiodic	
	ψ	$\frac{\partial\psi}{\partial\eta}$	ψ	$\frac{\partial\psi}{\partial\eta}$	ψ	$\frac{\partial\psi}{\partial\xi}$	ψ	$\frac{\partial\psi}{\partial\xi}$
α		0		0	s	a	a	s
β	0		0		a	s	s	a
γ		0		0	s	a	a	s
δ		0	0		a	s	s	a
ϵ	0			0	s	a	a	s
α'	0		0		s	a	a	s
β'		0		0	a	s	s	a
γ'	0		0		s	a	a	s
δ'	0			0	a	s	s	a
ϵ'		0	0		s	a	a	s

where l is summed over those orders containing the type s, and t is summed over the multiple sets of a type which may occur for the higher orders of l. Because the Kubic Harmonics contain all the requirements imposed by the symmetry of the lattice, (4) already satisfy proper BC at many points on the surfaces of the cell. It remains to satisfy the remaining BC imposed by periodicity shown in Table III.

The radial functions R_l can in general only be obtained by numerical integration (see next section) and depend on the special potential V used in the Schrödinger equation. Obviously, the coefficients A_{lt} will also depend on the special problem and cannot be determined analytically. To keep the labor within limits, only a finite number of terms in (4) must be used. Actually at most, four terms were used in which case three[10] constant coefficients A_{lt} and the eigenvalue E can be determined. This allows, in principle, the BC on at most[11] four distinct (not symmetrically equivalent) points to be satisfied, aside from those points whose BC are automatically satisfied by the KH. Eigenvalues obtained by various choices of sets of points yielded results 10–100 percent in error[12] for an empty lattice. It became evident that some method must be developed to produce a better "average" fit. This is now described.

To simplify arithmetic and to put (4) in a generally more convenient form, polynomials related to the Kubic Harmonics are defined

$$P_{lt}=\rho^l K_{lt}$$

so that (4) becomes

$$\psi=\Sigma_{lt}A_{lt}P_{lt}(x, y, z)S_l(E, \rho), \tag{5}$$

with

$$S_l=R_l\rho^{-l}. \tag{5a}$$

The functions S_l are obtained by mechanical integration. The form (5) or its normal derivative is used directly to fit BC on chosen points of a square face (actually at most only one point on squares, a central point, was fitted).

On the hexagonal surfaces an "average" fit was desired. For this purpose, a more complicated method had to be used: Eq. (5) was transformed to cylindrical coordinates, r, α, ξ ($\alpha=0$ in direction $+\eta$, Fig. 1, and ξ normal to the surface). Each polynomial, P_{lt}, was expressed as a Fourier series in α whose coefficients, P_{ltn}, are homogeneous polynomials in ξ and r of order l. The result is

$$\psi=[\Sigma_{lt}A_{lt}S_l(E, \rho)\Sigma_n P_{ltn}\cos n\alpha] + [\Sigma_{lt}A_{lt}S_l\Sigma_m P_{ltm}\sin m\alpha] \tag{6}$$

wherein either n is summed over zero, and all positive even integers, and m over all positive odd integers or the reverse, depending upon the type. In either case, the first term in (6) is symmetrical, the second is anti-symmetrical about the axis $\alpha=0$ and correspondingly ψ is said to be composed of an even part, ψ_+, and an odd part, ψ_-, respectively. The BC on the hexagonal surfaces are completely satisfied when ψ_+ (or ψ_-) and the normal derivative of ψ_- (or ψ_+) vanish over the hexagonal surfaces corresponding to the BC (Table III) that ψ is antisymmetric (or symmetric).

For a symmetrical eigenfunction the exact boundary conditions on the hexagonal surfaces may be stated in the form.

[10] The fourth coefficient is determined by normalization.

[11] Most points on the hexagonal faces have BC on both ψ and its normal derivative so that if such a point were included the number of points that can be fitted would be reduced.

[12] It is noteworthy that choices including the central point of the hexagonal faces used by Slater gave results which were particularly bad. This is understandable because the central point has a much smaller distance from the origin than an average point, and also has a much higher symmetry which makes the BC degenerate.

$$\text{For all } m \quad \Sigma_{lu} A_{lu} S_l(E, \rho) P_{lum}(r, \xi) = 0 \qquad (7)$$
$$\text{and for all } n \quad (\partial/\partial\xi)[\Sigma_{lu} A_{lu} S_l P_{lun}] = 0,$$

respectively. (When ψ is anti-symmetric m and n are interchanged in (7).) For fitting with the limited number of A_{lu} it was assumed, as an approximation that the radius, r_s, of the trace of the equal volume sphere on the hexagonal surface was a good "average" radius and that boundary requirements (7) corresponding to the higher harmonics in the expansion (6) could be neglected. The actual numerical procedure was, using the experimental lattice constant, Fig. 1, to make a likely choice of E and determine the disposable constant coefficients, A_{lu}, with a compatible number of BC, (7), of lowest m and n. The choice of E is then tested by use of a BC on a square surface, and then the procedure is repeated until the consistent value for E is found.

The method was tested using the ELT for each of the solutions carried out. In the limit of vanishing potential V, the radial functions S_l are functions akin to the Bessel's functions $J_{l+\frac{1}{2}}(K, \rho)/\rho^{\frac{1}{2}}$. Using these functions, the eigenvalues E are obtained from the above procedure of fitting the BC, and can then be compared with their known true values, $\mathbf{K}^2$. ($\mathbf{K}$ is the "free electron" wave vector which depends on $\mathbf{k}$ and on the number of the Brillouin zone.) The results are given in Table IV.

Discussion of the Method

Table IV lists the error in the computed empty lattice eigenvalues belonging to $\mathbf{k}=0,0,0$ and $0,0,\pi/a$ as a percentage of their true values for the lowest lying levels (not including the ground state for which the test is not applicable since $\psi=$constant is an exact solution). The number of terms used in the expansion of each of the eigenfunctions is also listed. This was arbitrarily limited by including Kubic Harmonics only up to $l=6$.

The results of the empty lattice test are most gratifying. At the upper end of the first Brillouin zone ($\mathbf{k}=0,0,\pi/a$), the error in the energy is one quarter of a percent or less, as compared with errors up to 40 percent in Slater's method (see Fig. 2, reference 5). Even at the upper end of the second zone, the error does not exceed 1 percent (Slater's method 35 percent). This improvement has been achieved while taking, in each individual case, only 2 to 4 terms in the expansion while Shockley took 8 terms in testing Slater's method. Even considering the greater complication of our Kubic Harmonics as compared with Legendre polynomials, and of our average fitting of the BC as compared with Slater's fitting at a point, the total labor in our method is probably no greater than in his. In fact, it would not involve excessive labor to include a considerably greater number of terms in our expansion. This would permit an extension of the method to higher Brillouin zones.

Since the eigenvalues for the empty lattice are in error by one percent or less it seems likely that the accuracy for filled cubic lattices will be limited by the accuracy of the potential, V. It is believed, therefore, that, at least for the wave vectors here considered, this is a one-electron approximation for cubic solids which compares favorably with methods for treating atoms.

The method is not confined to the investigation of one-electron states belonging to $\mathbf{k}=0,0,0$ and $0,0,\pi/a$. It appears to be a straightforward problem to obtain the energy spectrum for other symmetrical wave vectors without recalculation of the radial functions. This would involve constructing appropriate harmonics corresponding to the new irreducible representations and applying the more general periodicity boundary conditions compatible with the new wave vectors. Once the energy spectra of a number of symmetrical wave vectors has been determined the eigenvalue hypersurfaces can be traced out by interpolation guided by the BSW compatibility tables.[6] Behavior near wave vectors of symmetry

TABLE IV. Percent error in eigenvalues for the empty lattice and eigenvalues for sodium belonging to the lowest lying levels for $\mathbf{k}=0,0,0$ and $0,0,\pi/a$. Fitting for α and δ types belonging to $\mathbf{k}=0,0,\pi/a$ by the authors; remainder by Bowers (see reference 13).

Type	No. of terms used in eigenfunction expansion	k	K	E in Ry for sodium	ELT error in E
α_1	3	0,0,0	0	−0.608	——
γ	3	$0,0,\pi/a$	π/a	−0.036	0.16%
δ	4	$0,0,\pi/a$	π/a	−0.0135	0.07%
α	3	$0,0,\pi/a$	π/a	+0.0935	0.26%
γ	3	0,0,0	$2\pi/a$	+0.525	0.8%
δ	4	0,0,0	$2\pi/a$	+0.563	0.6%
ϵ'	2	0,0,0	$2\pi/a$	+0.600	1.0%

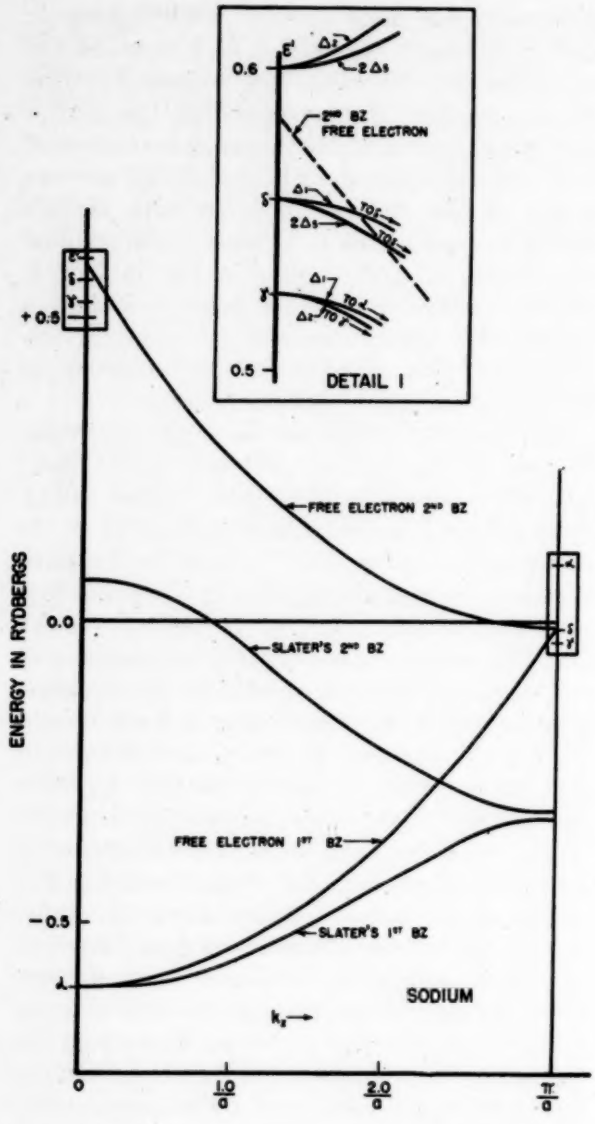

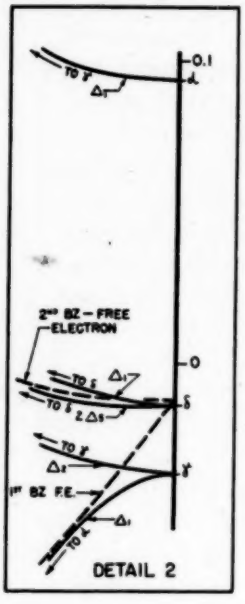

FIG. 2. This shows the eigenvalues at $\mathbf{k}=(0,0,0)$ and $(0,0,\pi/a)$ as computed for sodium by the present method. For comparison the eigenvalues in the 0,0,1 direction of the first two Brillouin zones for sodium as computed by Slater and for the free electron are shown. Detail 1 and Detail 2 sketch the BZ in the (0,0,1) direction which join up with the computed values (see BSW compatibility tables). Note that due to the degeneracy of the γ type at $\mathbf{k}=(0,0,\pi/a)$ there is no gap in the (0,0,1) direction between the first and second BZ.

can be investigated by perturbation methods with eigenfunctions obtained above; this has been done by Bowers.[13]

On the other hand, the harmonics and working relations are the same for all crystals having the same space group. Thus, having done the work for one substance, the problem for a substance having an identical lattice structure becomes one only of obtaining new radial functions and solving elementary sets of simultaneous algebraic equation. It must be admitted that thus far the method has been tested only for wave vectors of high symmetry. Accuracy of the method in general for crystals having a cell shape and symmetry departing widely from that of a sphere remains at present in doubt because of the basic approximation of separability of variables in the Schrödinger Equation.

RESULTS OF THE METHOD AS APPLIED TO SODIUM

When the method is to be applied to any problem other than the empty lattice, the potential V must be appropriately chosen. We have used the same potential[14] energy function

[13] W. Bowers, Doctoral Thesis, Cornell University (1943).

[14] W. Prokofjew, Zeits. f. Physik **58**, 255 (1929).

V as W-S[2] and Slater.[3] The radial functions, R_l, were obtained by mechanical integration†† and checked by numerical integration using I.B.M. machines. The agreement was satisfactorily within the expected limits of error of the differential analyzer. Radial wave functions were obtained for $l=0$ to 6, and for energies $E=+0.6$, $+0.3$, $+0.1$, 0, -0.1, -0.3, and -0.6 Rydbergs. The eigenvalues were obtained by interpolation.

Table IV lists the seven lowest lying eigenvalues for $\mathbf{k}=0,0,0$ and $0,0,\pi/a$ as computed for sodium. For comparison Fig. 2 shows in addition the eigenvalues of the first and second Brillouin zones along the line 0,0,1 in $\mathbf{k}$ space, for the case of the free electron and that of sodium according to Slater's Fig. 3. Detailed sketches in Fig. 2 exhibit (for sodium) the variation from free electron eigenvalues near the center and boundary of the Brillouin zones. They also show the "sticking together" of the eigenvalue hypersurfaces at these points which was pointed out by BSW, and indicate the extremity eigenvalues to which the lower hypersurfaces join as determined by the BSW compatibility tables. The notations Δ_1, Δ_2, etc., indicate that the given eigenvalue belongs to the respective representation of the group of $\mathbf{k}$ (notation of BSW).

A very significant result of the present calculation is that for sodium in the 0,0,1 direction the electrons are essentially free. If the electrons were in fact free, the eigenvalue at the corner $(0,0,\pi/a)$ of the first Brillouin zone would be $-0.608+(\pi/a)^2=-0.012$ rydberg which is very close to the eigenvalue for the δ-type (-0.0135) actually found there and is in between the other two types. However, there is a slight deviation from freeness very close to this corner since the lowest lying energy hypersurface joins with the γ type with energy -0.036 rydberg. (The total width of the first Brillouin zone in the 0,0,1 direction is thus 4 percent less than for free electrons.) Bowers[13] has shown that this deviation extends only a very short distance from the corner. This essential freeness of the electron up to a point close to the corner of the first Brillouin zone is in agreement with the calculations of Bardeen,[15] wherein he obtained (near $\mathbf{k}=0,0,0$) the ratio of electronic mass to effective mass of 1.069 indicating a deviation in eigenvalues of 7 percent from those of the free electron.

Actually, as shown in Fig. 2, the eigenvalues of the higher Brillouin zones also remain close to those for the free electron. However, there can be little doubt that the gap between the δ and γ states amounting to 0.022 rydberg is real because the empty lattice test indicates an uncertainty in calculated energies of only 0.26 percent of 0.6 Ry, that is, 0.0016 Ry, about 7 percent of the calculated difference between δ and γ states.

Figure 2 shows poor agreement with Slater's calculations for the 0,0,1 direction. It is suspected that these markedly different results are, in part, because of his choice of the centers of hexagons as fitting points. Experience gained in the present work indicates that these points were far from average points yielding particularly poor results in the case of the empty lattice.[12]

At $\mathbf{k}=0,0,\pi/a$ the lowest lying eigenvalue is the γ type ($E_\gamma=-0.036$ Ry) considerably below the lowest α type ($E_\alpha=+0.094$ Ry). The type Δ_1 (notation is that of BSW), belonging to the wave vectors lying on the line 0,0,1 is compatible with both the α and γ types at the line extremities. Thus, as we go along the line 0,0,1 in $\mathbf{k}$ space, the eigenvalues of the first Brillouin zone start at the α type ground state and end on this γ type at $\mathbf{k}=0,0,\pi/a$. Since the γ type is doubly degenerate it is also the lowest eigenvalue of the second Brillouin zone; if we then proceed again along the line 0,0,1 this eigenvalue emerges as a Δ_2 type from this γ type and ends on the low lying γ type at $\mathbf{k}=0,0,0$. Therefore, due to the "sticking together" effect of BSW, there is actually no gap in energy at all in the direction 0,0,1 between the eigenvalues of the first and second Brillouin zones. This condition of course does allow a change in density of states near the corner, and probably also gaps in other direction of $\mathbf{k}$ space, but at the corner of the first Brillouin zone there is no actual discontinuity.

No experimental verification of sufficient resolving power exists to support these results.

†† In this connection the authors are indebted to Professor S. H. Caldwell of M.I.T. in making available the use of the mechanical Bush Differential Analyzer; to Mr. P. O. Crawford who as a graduate assistant (1940) made the work possible by operating the machine; to Dr. Martin Schwarzschild who ran an independent check on two of the functions at the Thomas Watson Computing Bureau at Columbia University.

[15] J. Bardeen, J. Chem. Phys. 6, 367 (1938).

X-ray absorption measurements of high resolving power for potassium, which is expected to show wider departure from free electrons, have been carried out by Platt.[16] The K edge investigated shows quite close agreement with his theoretically predicted absorption which was based on the assumption that the electrons are free. No evidence existed to show an energy gap. This, of course, is at best supporting evidence of the non-existence of a gap in potassium since gaps may exist which could be completely masked by the eigenvalue dependence upon wave vector direction.

[16] J. B. Platt, Phys. Rev. 69, 337 (1946).

ACKNOWLEDGMENTS

The authors are indebted to Dr. W. A. Bowers for permission to publish his results on the five additional states shown in Table IV and also wish to thank Dr. Bowers for continuing the application of the method when the war interrupted the work.

PHYSICAL REVIEW VOLUME 71, NUMBER 9 MAY 1, 1947

The Band Theory of Graphite

P. R. WALLACE*
National Research Council of Canada, Chalk River Laboratory, Chalk River, Ontario
(Received December 19, 1946)

The structure of the electronic energy bands and Brillouin zones for graphite is developed using the "tight binding" approximation. Graphite is found to be a semi-conductor with zero activation energy, i.e., there are no free electrons at zero temperature, but they are created at higher temperatures by excitation to a band contiguous to the highest one which is normally filled. The electrical conductivity is treated with assumptions about the mean free path. It is found to be about 100 times as great parallel to as across crystal planes. A large and anisotropic diamagnetic susceptibility is predicted for the conduction electrons; this is greatest for fields across the layers. The volume optical absorption is accounted for.

1. INTRODUCTION

THE purpose of this paper is to develop a basis for the explanation of some of the physical properties of graphite through the band theory of solids. We shall be concerned primarily with a discussion of its electrical conductivity, but the treatment given makes possible the explanation not only of the electrical conductivity and its anisotropy but also the thermal conductivity, diamagnetic susceptibility, and optical absorption.

The electrical resistivity of single crystals of graphite is about 4 to 6×10^{-5} ohm-cm.[1] This corresponds to a conductivity of the order of that of a poor metal. The temperature coefficient of the conductivity is negative, as in the case of a metal. Polycrystalline graphite, on the other hand, has a much higher resistivity which varies very strongly according to the type of graphite used, and has a *positive* temperature coefficient of conductivity[2] to about 1400°C, and negative thereafter. Since the crystals of commercial graphites tend to be of the order of 10^{-6} cm, and it is quite porous (density $\sim$1.6 as against 2.25 for single crystals), it seems reasonable to attribute the high resistivity of polycrystalline graphite to the crystal boundaries, on which may be lodged impurity atoms. The latter would tend to be driven off on heating, thus accounting for the observed temperature dependence. We shall show, however, that the band theory would seem to make possible the explanation of the conductivity properties of single crystals.

* Now at McGill University.

[1] Given by E. Ryschewitsch, Zeits. f. Elektrochem. ang. physik. Chemie 29, 474 (1923), as $3.9–6\times10^{-5}$ ohm-cm.

[2] C. A. Hansen, Trans. Am. Electrochem. Soc. 16, 329 (1909) gives 137.5×10^{-5} at 0°C 82.5×10^{-5} at 1400°C.

2. ZONE STRUCTURE OF A SINGLE HEXAGONAL LAYER

Since the spacing of the lattice planes of graphite is large (3.37A) compared with the hexagonal spacing in the layer (1.42A), a first approximation in the treatment of graphite may be obtained by neglecting the interactions between planes, and supposing that conduction takes place only in layers.

Graphite possesses four valence electrons. Three of these form tight bonds with neighboring atoms in the plane. Their wave functions are of the form

$$\frac{1}{\sqrt{3}}(\psi_c(2s)+\sqrt{2}\psi_c(\sigma_i 2p)) \quad (i=1, 2, 3),$$

where $\psi_c(2s)$ is the $(2s)$ wave function for carbon and $\psi_c(\sigma_i 2p)$ are the $(2p)$ wave functions whose axes are in the directions σ_i joining the graphite atom to its three neighbors in the plane. The fourth electron is considered to be in the $2p_z$ state, its nodal plane being the lattice plane and its axis of symmetry perpendicular to it. The three electrons forming co-planar bonds will not play a part in the conductivity; we shall therefore treat graphite as having one conduction electron, in the $2p_z$ state.

For the hexagonal layer the unit cell, which is designated by $WXYZ$ in Fig. 1, contains two atoms, A and B. The fundamental lattice displacements are $a_1=\mathbf{AA}'$ and $a_2=\mathbf{AA}''$; their magnitude is $1.42\times\sqrt{3}=2.46\text{A}=a$. The reciprocal lattice vectors have magnitude $2/\sqrt{3}a$, and are in the direction AB and AZ, respectively. From this it follows that the first Brillouin zone is a

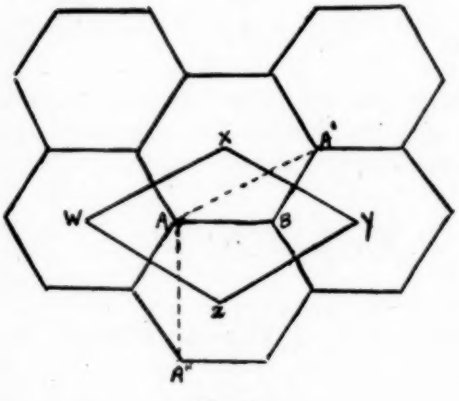

FIG. 1.

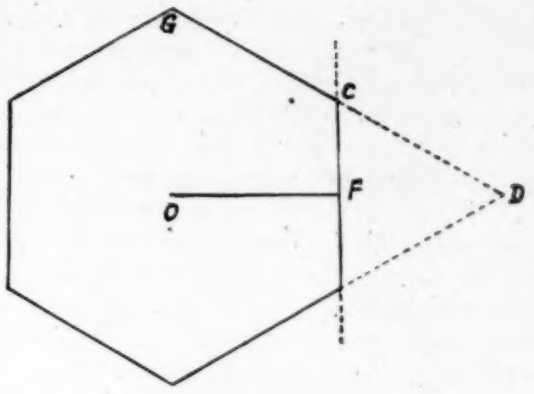

FIG. 2.

hexagon (Fig. 2) whose sides are distant $1/\sqrt{3}a$ from its center. It is easily shown that this zone contains one electron per atom, for the density of electron states in k-space is $2A$, where A is the area of the crystal. The zone in question therefore contains $2A\times 2/(\sqrt{3}a^2)$ electron states. But the atomic area (area per atom in the layer) is $\sqrt{3}a^2/4$, and the number of atoms is $4A/\sqrt{3}a^2$, which is exactly equal to the number of electrons in the zone.

The zone containing two states per atom is obtained by extending the sides of the hexagon to form a six pointed star.

Let us now consider the problem from the viewpoint of the "tight binding approximation." If $X(r)$ is the normalized orbital $2p_z$ wave function for an isolated atom, then the wave function in the tight binding approximation has the form:

$$\psi=\varphi_1+\lambda\varphi_2 \tag{2.1}$$

where

$$\left.\begin{aligned}\varphi_1&=\textstyle\sum_A \exp[2\pi i\mathbf{k}\cdot\mathbf{r}_A]X(\mathbf{r}-\mathbf{r}_A)\\ \text{and}\quad \varphi_2&=\textstyle\sum_B \exp[2\pi i\mathbf{k}\cdot\mathbf{r}_B]X(\mathbf{r}-\mathbf{r}_B)\end{aligned}\right\}. \tag{2.2}$$

The first sum is taken over A and all the lattice points generated from it by primitive lattice translations; the second sum is similarly over the points generated from B.

From variational principles it is known that to get the best value of E for this approximation we substitute in the wave equation from (2.1), multiply by φ_1 and φ_2, respectively, integrate, and then eliminate λ from the resulting two equations.

Let us neglect the overlap of the p_z wave functions centered on different atoms, i.e., let us

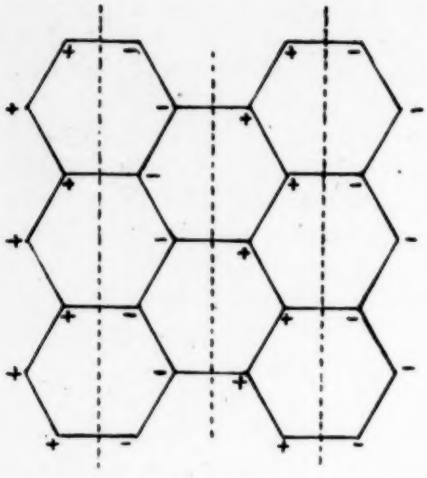

FIG. 3.

assume

$$\int X(\mathbf{r}-\mathbf{r}_A)X(\mathbf{r}-\mathbf{r}_B)d\tau=0. \qquad (2.3)$$

Then, substituting (2.1) in

$$H\psi=E\psi \qquad (2.4)$$

and proceeding as outlined, we get

$$H_{11}+\lambda H_{12}=ES,$$
$$H_{21}+\lambda H_{22}=\lambda ES,$$

where

$$H_{11}=\int \phi_1^* H\phi_1 d\tau, \quad H_{12}=H_{21}^*=\int \phi_1^* H\phi_2 d\tau,$$

$$H_{22}=\int \phi_2^* H\phi_2 d\tau$$

and

$$S=\int \phi_1^*\phi_1 d\tau=\int \phi_2^*\phi_2 d\tau.$$

Eliminating λ we obtain the secular equation

$$\begin{vmatrix} H_{11}-ES & H_{12} \\ H_{21} & H_{22}-ES \end{vmatrix}=0,$$

from which it is found that

$$E=\frac{1}{2S}\{H_{11}+H_{22} \pm((H_{11}-H_{22})^2+4|H_{12}|^2)^{\frac{1}{2}}\}. \qquad (2.5)$$

Now by virtue of the neglect of the overlap integrals, $S=N$, the number of unit cells in the crystal, and by symmetry $H_{11}=H_{22}$. Introducing

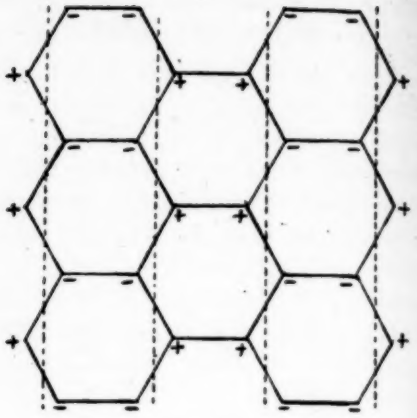

FIG. 4.

$$H_{11}'=H_{22}'=\frac{1}{N}H_{11}=\frac{1}{N}H_{22}, \qquad (2.6)$$

$$H_{12}'=\frac{1}{N}H_{12}$$

we have, finally

$$E=H_{11}'\pm|H_{12}'|. \qquad (2.7)$$

The positive sign will apply to the outside of the hexagonal zone, the negative sign to the inside. The discontinuity of energy across the zone boundary is then

$$\Delta E=2|H_{12}'|. \qquad (2.8)$$

Let us now calculate $H_{11}'=H_{22}'$ and H_{12}'.

$$H_{11}'=\frac{1}{N}\sum_{A,A'}\exp[-2\pi i\mathbf{k}\cdot(\mathbf{r}_A-\mathbf{r}_{A'})] \times\int X^*(\mathbf{r}-\mathbf{r}_A)HX(\mathbf{r}-\mathbf{r}_{A'})d\tau.$$

Omitting the exchange integrals over atoms more distant than nearest neighbors amongst the atoms A, and writing

$$E_0=\int X^*(\mathbf{r})HX(\mathbf{r})d\tau,$$

$$\gamma_0'=-\int X^*(\mathbf{r}-\boldsymbol{\rho}')HX(\mathbf{r})d\tau,$$

where $\boldsymbol{\rho}'=\mathbf{a}_1$ (say) is a vector joining nearest

neighbors among the atoms A, we get

$$H_{11}'=E_0-2\gamma_0'(\cos 2\pi k_y a+2\cos\pi k_x a\sqrt{3}\cos\pi k_y a).$$

If we write

$$H=H_0+(H-H_0),$$

where H_0 is the Hamiltonian for an isolated carbon atom, and put

$$H-H_0=V-U<0,$$

where V is the periodic potential of the lattice and U is the potential field for an isolated atom, we may write, since $H_0X=E_0X$,

$$E_0=\bar{E}-\int X^*(\mathbf{r})(U-V)X(\mathbf{r})d\tau, \quad (2.9)$$

and

$$\gamma_0'=\int X^*(\mathbf{r}-\boldsymbol{\varrho}')(U-V)X(\mathbf{r})d\tau>0. \quad (2.10)$$

E_0 is the energy of an electron on the $2p_z$ state in carbon.

Let us next calculate H_{12}. For this, we shall consider only interactions between nearest neighbors in the lattice, the nearest neighbors of atoms of type A being always atoms of type B and *vice versa*. Writing

$$\gamma_0=\int X^*(\mathbf{r}-\boldsymbol{\varrho})(U-V)X(\mathbf{r})d\tau>0, \quad (2.11)$$

where $\boldsymbol{\varrho}=\mathbf{AB}$, we obtain

$$H_{12}'=-\gamma_0(\exp[-2\pi i k_x(a/\sqrt{3})]+2\cos\pi k_y a\cdot\exp[2\pi i k_x(a/2\sqrt{3})]),$$

so that

$$|H_{12}|^2=\gamma_0^2(1+4\cos^2\pi k_y a+4\cos\pi k_y a\cos\pi k_x\sqrt{3}a).$$

The energies at various points may now be written down:

at O: $E=E_0-3\gamma_0-6\gamma_0'$,
at D: $E=E_0+3\gamma_0-6\gamma_0'$,
at C: $E=E_0+3\gamma_0'$;
at F, inside: $E=E_0-\gamma_0+2\gamma_0'$,
outside: $E=E_0+\gamma_0+2\gamma_0'$.

Over a side of the zone there is across the boundary at any point a discontinuity of energy of amount

$$2\gamma_0(2\cos\pi k_y a-1) \quad (2.12)$$

which is greatest at the center and decreases to zero at the corners.

The degeneracy at C and similar points, and the zero-energy gap at these points, are presumably consequences of the symmetry of the lattice, and are independent of the approximations considered.

It is easy to determine the form of the wave functions corresponding to different k. Consider, for example, the point F. Inside the zone boundary $\lambda=-1$, and consequently the nodes of the wave functions bisect the lines joining A and B atoms: the sign of the wave function at lattice points is designated by + or − signs in Fig. 3. It is readily seen how the expression for the energy arises. Since an atom has two nearest neighbors of the same sign, and one opposite, and since $(V-U)$ is negative, there will be a contribution to the energy from exchange between nearest neighbors of $-2\gamma_0+\gamma_0=-\gamma_0$. Of second neighbors, we have two of the same sign and four opposite, giving us $2\gamma_0'$.

In Fig. 4 are represented the nodes of the wave function corresponding to a point *outside* the zone boundary at A. Since here $\lambda=1$, the maxima and minima correspond to the nodes of the previous case. The expression for the energy can be verified in the same way. Similar arguments may be carried out for other points in k-space.

Consider next the energy contours. Near the bottom of the band they are circular:

$$E=E_0-3\gamma_0-6\gamma_0'+\pi^2(\gamma_0+6\gamma_0')(k_x^2+k_y^2)a^2. \quad (2.13)$$

The hexagon whose sides are distant $1/2a$ from the center of the Brillouin zone is a surface of constant energy. (This conclusion is, of course, true only in the approximation which we are

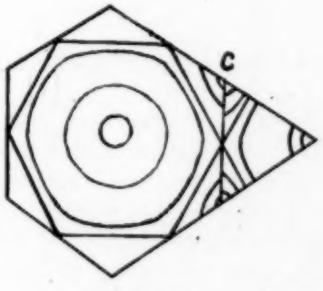

FIG. 5.

here considering.) Curves of constant energy are indicated in Fig. 5. Near the corner C

$$E=E_0+3\gamma_0'\pm\sqrt{3}\pi\gamma_0|\mathbf{k}-\mathbf{k}_c|a-3\pi^2\gamma_0'|\mathbf{k}-\mathbf{k}_c|^2a^2, \tag{2.14}$$

and the surfaces of constant energy are again circular.

It should be noted that, when the reduced zone scheme is used, the energy contours have the same shape for the second zone as for the first.

3. NUMBER OF FREE ELECTRONS AND CONDUCTIVITY OF A SINGLE HEXAGONAL LAYER

In this section we shall neglect γ_0' relative to γ_0. We then have

$$|E-E_c|\approx\sqrt{3}\pi\gamma_0 a|\mathbf{k}-\mathbf{k}_c| \tag{3.1}$$

near the corners of the Brillouin zone. At the absolute zero of temperature, the hexagonal zone will be completely filled, and the next zone will be completely empty. At higher temperatures, there will be some thermal "overflow" into the outer zone. The extent of this overflow will be (in energy) of amount comparable to kT. The energy contour $E=E_c+kT$ is approximately circular with radius $kT/(\pi\sqrt{3}\gamma_0 a)$ provided $kT\gg\gamma_0$, which is certainly the case at ordinary temperatures.

Now if $N(E)dE$ is the number of electronic energy states in the energy interval dE,

$$N(E)=2A\int\frac{d\sigma}{|\mathrm{grad}_k E|}, \tag{3.2}$$

where A is the area of the lattice, and the integral is taken over the curve on which the energy is E. This gives, since $|\mathrm{grad}_k E|$ is constant,

$$N(E)=\frac{4A|E-E_c|}{3\pi\gamma_0^2a^2}, \tag{3.3}$$

or, since the area per atom is $\sqrt{3}a^2/4$,

$$N(E)/N_a=\frac{1}{\pi\sqrt{3}\gamma_0^2}|E-E_c|=\frac{|\epsilon|}{\pi\sqrt{3}\gamma_0^2}, \tag{3.4}$$

where N_a is the number of atoms in the lattice. The form of $N(E)$ near E_c is illustrated in Fig. 6.

Conduction will take place through the electrons excited into the upper band, and through the positive holes (equal in number) created in the lower band.

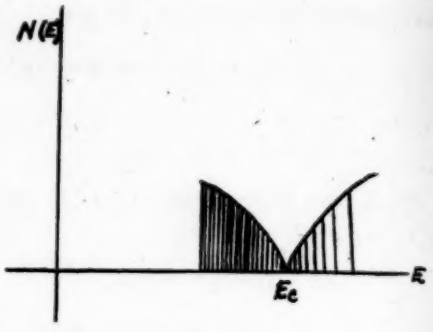

FIG. 6.

To calculate the number of these, we must know the Fermi distribution. For moderate temperatures, $N(E)$ is even in $\epsilon=|E-E_c|$ over the whole range in which the Fermi distribution is different from its value at absolute zero. Therefore, in the Fermi distribution function

$$f(E)=\frac{1}{\exp[(E-\zeta)/kT]+1},$$

we shall have $\zeta=E_c$; in other words, we may write

$$f(E)=f(\epsilon)=1/(e^{\epsilon/kT}+1). \tag{3.5}$$

It follows that the number of free electrons plus positive holes per atom is

$$2\int_0^\infty\frac{N(E)}{N_a}f(E)dE=\frac{\pi}{6\sqrt{3}}\left(\frac{kT}{\gamma_0}\right)^2. \tag{3.6}$$

Now C. A. Coulson[3] has estimated that γ_0 is about 20 kcal./mole, or about 0.9 ev. At room temperature $kT=0.025$ ev. Therefore the "effective number of free electrons" n_{ett}, per atom, is

$$n_{ett}=2.3\times10^{-4}.$$

To determine the conductivity of our graphite layer, let us calculate directly the current in the presence of a given external field. Explicitly, this is given by

$$\mathbf{j}=2\int ev f(\mathbf{k})d\tau_k\cdot(2/c), \tag{3.7}$$

where $f(\mathbf{k})$ is the Fermi distribution in the presence of the field, and $\frac{1}{2}c=3.37$A is the dis-

[3] Private communication to the author.

tance between graphite layers. $f(\mathbf{k})$ is given by

$$f(\mathbf{k})=f_0\left(\mathbf{k}-\frac{e\tau}{h}\mathbf{F}\right), \tag{3.8}$$

where f_0 is the undisturbed Fermi function (3.5), and τ is the inverse of the probability of scattering per unit time. For moderate fields we may expand this

$$f(\mathbf{k})=f_0(\mathbf{k})+g(\mathbf{k}) \tag{3.9}$$

where

$$g(\mathbf{k})=-\frac{e\tau}{h}\mathbf{F}\cdot\mathrm{grad}f_0. \tag{3.10}$$

Writing

$$\mathbf{v}=\frac{1}{h}\mathrm{grad}_k E,\quad \mathrm{grad}f_0=\frac{df_0}{dE}\mathrm{grad}_k E,$$

$$d\tau_k=d\sigma_k\frac{dE}{|\mathrm{grad}E|},$$

$d\sigma_k$ being element of length on the curve $E=$constant, we have

$$\mathbf{j}=-\frac{4e^2\tau}{h^2c}\int\frac{df_0}{dE}\left[\int(\mathbf{F}\cdot\mathrm{grad}E)\frac{\mathrm{grad}E}{|\mathrm{grad}E|}d\sigma_k\right]dE,$$

where the inner integral is over the surface of constant energy E. The component of current $\mathbf{j}_F$ in the direction of the field is

$$\mathbf{j}_F=-\frac{4e^2\tau}{h^2c}\int\frac{df_0}{dE}\left[\frac{1}{F}\int\frac{(F\cdot\mathrm{grad}E)^2}{|\mathrm{grad}E|}d\sigma_k\right]dE.$$

Averaging over all directions of the field in the plane of the layer we get

$$\sigma_{\|}=-\frac{2e^2\tau}{h^2c}\int\frac{df_0}{dE}\left[\int|\mathrm{grad}E|\,d\sigma_k\right]dE. \tag{3.11}$$

By virtue of (3.1) this is

$$\sigma_{\|}=-\frac{8\pi e^2\tau}{h^2c}\int|\epsilon|\frac{\partial f_0}{\partial\epsilon}d\epsilon$$
$$=\frac{16\pi e^2\tau}{h^2c}kT\log 2. \tag{3.12}$$

To get a numerical value of the conductivity it is necessary to know something about τ, or alternatively about the mean free path $l=v\tau$. We will not attempt to calculate this quantity in the present paper. Let us note, however, that experimental evidence requires that the mean free path decrease with temperature faster than T^{-1}. In this connection, one might call attention to the sharply increased mobility found in polar salts at low temperatures for thermal electrons. The mean free path has the form

$$l=C\left(\frac{T}{\theta}\right)^{\frac{1}{4}}(e^{\theta/T}-1),^{4} \tag{3.13}$$

where θ is the Debye temperature and C is a constant of the order of one atomic distance. The conductivity electrons in graphite are also essentially thermal. If the mean free path is assumed to be of the same order of magnitude as given by (3.13), with $C=2\times10^{-8}$ cm and θ estimated from specific heat evidence as about 2000°C we will get

$$l\approx3\times10^{-6}\text{ cm}. \tag{3.14}$$

This gives rise to a resistivity

$$\rho\approx5\times10^{-5}\text{ ohm-cm}.$$

It seems therefore, that (3.14) gives at least the right order of magnitude for l. This point, and the temperature dependence of l, seem worth further investigation.

From the formula

$$\sigma=N_{\mathrm{eff}}e^2\tau/m_{\mathrm{eff}}, \tag{3.15}$$

we can calculate the "mean effective mass," m_{eff}, of our conductivity electrons. This is found to be

$$m_{\mathrm{eff}}=\frac{h^2kT}{36\log 2\cdot a^2\gamma_0^2} \tag{3.16}$$

which yields, on numerical evaluation, at room temperature

$$m_{\mathrm{eff}}=1/18\text{ electron mass}. \tag{3.17}$$

4. THE BRILLOUIN ZONES OF GRAPHITE

The graphite lattice is built up of hexagonal layers whose relation to each other is indicated in Fig. 7. Dotted lines indicate one layer, and

[4] N. F. Mott and R. A. Gurney, *Electronic Processes in Ionic Crystals* (Oxford University Press, Oxford, 1940), p. 107. Note also the increase of mobility with decreasing temperature in the semiconductor Cu_2O shown in Fig. 66, p. 168.

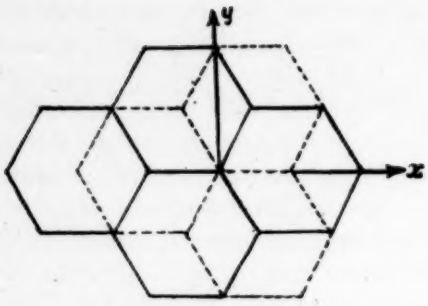

FIG. 7.

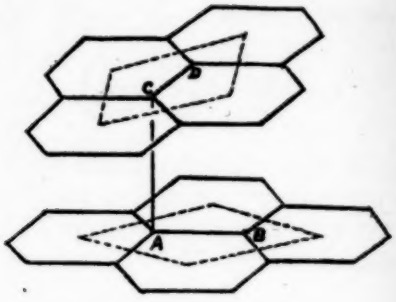

FIG. 8.

the full lines the one immediately above it. A set of basic displacement vectors of the lattice is

$$\mathbf{a}_1=[\tfrac{1}{2}\sqrt{3}a,\ -\tfrac{1}{2}a,\ 0],\quad \mathbf{a}_2=[0,\ a,\ 0],$$
$$\mathbf{a}_3=[0,\ 0,\ c],\quad (4.1)$$

c being twice the distance between layers of the lattice. In Fig. 8 the relation between the layers is shown in perspective. The points A, B, C, D are the four atoms of a unit cell.

The volume of the unit cell is

$$V_{\text{cell}}=\mathbf{a}_1\cdot(\mathbf{a}_2\times\mathbf{a}_3)=\frac{\sqrt{3}}{2}a^2c,$$

so that the atomic volume is

$$V_{\text{atomic}}=\frac{\sqrt{3}a^2c}{8}.\quad (4.2)$$

The intercepts of a possible unit cell on adjacent planes are shown in Fig. 8. The cell would extend beyond these two planes on each side halfway to the next planes, which are not shown.

Reciprocal lattice vectors corresponding to (4.1) are

$$\mathbf{b}_1=\left[\frac{2}{\sqrt{3}a},\ 0,\ 0\right],$$
$$\mathbf{b}_2=\left[\frac{1}{\sqrt{3}a},\ \frac{1}{a},\ 0\right],$$
$$\mathbf{b}_3=\left[0,\ 0,\ \frac{1}{c}\right].$$

It follows that the lowest Brillouin zone is bounded by six vertical planes forming a right hexagonal cylinder whose sides are distant $1/\sqrt{3}a$ from its axis. It appears at first that the height of the lowest zone is $1/c$. This is, however, not the case, for the plane at height $1/2c$ corresponds to Bragg reflection of waves whose wave-length is $2c$. Thus reflections from successive planes (distance $c/2$) differ in phase by π, and therefore destroy each other. The structure factor therefore vanishes on the planes $k_z=\pm(1/2c)$, and there is no energy discontinuity over them. The horizontal boundaries of the first zone are therefore at $k_z=\pm(1/c)$. The lowest Brillouin zone so described has the volume $4/\sqrt{3}a^2c$. But the density of states is twice the volume of the crystal, that is,

$$2\times(\text{number } N \text{ of cells})\times(\text{volume of cell})=\sqrt{3}a^2cN.$$

Thus there are 4 N electron states in the lowest Brillouin zone, or one per atom. Since as in the case of a single layer, there is just one "conductivity" electron per atom, the lowest Brillouin zone will be just filled at the absolute zero of temperature.

In Fig. 9 we indicate the *upper half* of the zone in question.

Let us now consider the problem from the viewpoint of the "tight binding approximation." As in the case of a single layer, let $X(r)$ be the $2p_z$ wave function of an isolated C atom. Then we assume for the collective wave function of the crystal

$$\Psi=\sum_{i=1\cdots4}\lambda_i\Psi_i$$
$$=\sum_{i=1\cdots4}\lambda_i\left(\sum_\alpha \exp[2\pi i\mathbf{k}\cdot\mathbf{r}_i^\alpha]X(\mathbf{r}-\mathbf{r}_i^\alpha)\right),\quad (4.3)$$

where $i=1, 2, 3, 4$ correspond to atoms of the type A, B, C, D, respectively, and α enumerates the different atoms of a given type in the crystal.

Proceeding exactly as in the case of the hexagonal layer, we are led to a secular equation for the energy

$$\|H_{ij}'-E\delta_{ij}\|=0. \tag{4.4}$$

Now the diagonal elements are

$$H_{11}'=H_{22}'=H_{33}'=H_{44}'=E_0'-2\gamma_0'(\cos 2\pi k_y a + 2\cos\pi\sqrt{3}k_y a\cos\pi k_y a)=H_0. \tag{4.5}$$

E_0' is not quite the same as the E_0 in the previous section, due to a difference in the potential; we shall, however, subsequently drop the prime for convenience.

In calculating the non-diagonal terms, we shall at first consider first and second neighbors *in* the planes, and also first and second neighbors *between* planes.

The elements may now be calculated:

H_{12}. This is equal to

$$-\gamma_0(\exp[-2\pi ik_x(a/\sqrt{3})] + 2\cos\pi k_y a\cdot\exp[\pi ik_x(a/\sqrt{3})])$$

where

$$\gamma_0=\int X^*(\mathbf{r}-\varrho_{AB})(U-V)X(\mathbf{r})d\tau>0.$$

H_{13}. This is equal to

$$2\gamma_1\cos\pi k_z c$$

where

$$\gamma_1=\int X^*(\mathbf{r}-\varrho_{AC})(V-U)X(\mathbf{r})d\tau.$$

$\gamma_1>0$ because $(V-U)$ is negative, and

$$X^*(\mathbf{r}-\varrho_{AC}),$$

$X(\mathbf{r})$ have opposite signs between the planes, where the contribution to the integral is greatest.

H_{14}. This is equal to

$$2\gamma_1'\cos\pi k_z c(\exp[2\pi ik_x(a/\sqrt{3})] + 2\cos\pi k_y a\cdot\exp[-\pi ik_x(a/\sqrt{3})]),$$

where

$$\gamma_1'=\int X^*(\mathbf{r}-\varrho_{AD})(V-U)X(\mathbf{r})d\tau,$$

and is almost certainly positive, though it has not been evaluated.

The other elements may be written in terms of the above. It may easily be verified that

$$H_{23}=H_{14},\quad H_{24}=H_{23}^*,\quad H_{34}=H_{12}^*.$$

If we put the diagonal elements equal to H_0, $2\cos\pi k_z c=\Gamma$ and

$$\exp[-2\pi ik_x(a/\sqrt{3})]+2\cos\pi k_y a\cdot\exp[\pi ik_x(a/\sqrt{3})]=S, \tag{4.5}$$

the secular equation becomes

$$\begin{vmatrix} E-H_0 & -\gamma_0 S & \gamma_1\Gamma & \gamma_1'\Gamma S \\ -\gamma_0 S^* & E-H_0 & \gamma_1'\Gamma S & \gamma_1'\Gamma S \\ \gamma_1\Gamma & \gamma_1'\Gamma S & E-H_0 & -\gamma_0 S^* \\ \gamma_1'\Gamma S^* & \gamma_1'\Gamma S & -\gamma_0 S & E-H_0 \end{vmatrix}=0. \tag{4.6}$$

The exact solution of this equation presents some difficulty. We shall neglect γ_1' at first, and later treat it as a perturbation. In the lowest approximation, then, we get on solving,

$$E=H_0\pm\tfrac{1}{2}\gamma_1\Gamma\pm[\tfrac{1}{4}\gamma_1^2\Gamma^2+\gamma_0^2|S|^2]^{\frac{1}{2}}.$$

With regard to the sign in front of the $\frac{1}{2}\gamma_1\Gamma$ term, the choice here is immaterial, a change of sign merely corresponding to reflection in the plane $k_z=1/2c$ of the two halves of the upper half-zone, and similarly in the lower half-zone. By choosing the negative sign, we adhere to the convention that the bottom of the zone (point of lowest energy) should be at the center.

The signs $\pm$ in front of the square root correspond to the outside and inside of the lowest zone, respectively, i.e. inside

$$E=H_0-\tfrac{1}{2}\gamma_1\Gamma-[\tfrac{1}{4}\gamma_1^2\Gamma^2+\gamma_0^2|S|^2]^{\frac{1}{2}}, \tag{4.7a}$$

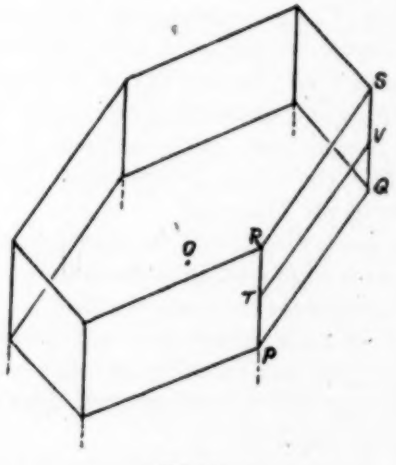

FIG. 9.

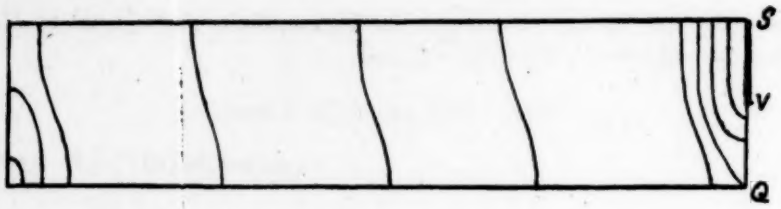

FIG. 10. Energy contours on the inside of the zone.

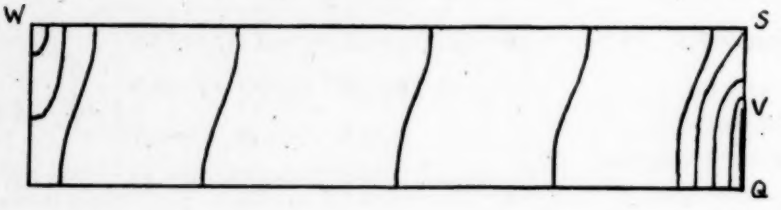

FIG. 11. Energy contours on the outside of the zone.

and outside

$$E=H_0-\tfrac{1}{2}\gamma_1\Gamma+[\tfrac{1}{4}\gamma_1^2\Gamma^2+\gamma_0^2|S|^2]^{\frac{1}{2}}. \quad (4.7b)$$

The energy inside is always $\leqslant H_0=E_0$; it has the latter value for $|S|^2=0$ and $\Gamma<0$ (i.e., $k_z\geqslant 1/2c$). Now

$$|S|^2=(1-2\cos\pi k_y a)^2 \quad (4.8)$$

on the sides of the zone, and is zero at the vertical edges. Thus the maximum energy inside (E_0) is attained on the upper (and lower) quarter of the vertical edges of the zone.

By a similar argument, the energy outside has its *minimum* value, (which is also E_0) on the middle half of the vertical edges of the zone. The energy gap is therefore zero only at twelve points; two on each vertical edge.

In Fig. 10 we indicate the form of the sections of surfaces of constant energy by a plane such as that through *OSVQ* in Fig. 9.

In Fig. 11 we represent the cross sections of the energy contours by a plane such as the extension of *PQRS* beyond *QS*. *W* is at a tip of the six-pointed star which forms the upper boundary of the second zone, this zone being obtained by extending the vertical sides and the top and bottom of the first zone.

The energy contours in planes $k_z=$constant will have a form similar to those shown in Fig. 5. The hexagonal lines of constant energy will appear in each plane, but will correspond to different energies in different planes. The zero energy gap will of course only appear in the planes $k_z=\pm(1/2c)$.

The strong anisotropy in some of the properties of graphite (electrical and thermal conductivity, magnetic susceptibility) is caused by the very anisotropic form of the energy surfaces near the corner of the zone. These anisotropies will become greater as the temperature is lowered, and the surfaces of energy ($E_0\pm kT$) approach segments of lines.

Let us now see how this picture is altered if we take account of γ_1', the exchange integral between atoms such as *A* and *D* in Fig. 8. If we expand (4.6) to terms of the first order in γ_1' and solve, using the relation (4.7), we find that the energy is increased by an amount

$$\epsilon=\gamma_0\gamma_1'\Gamma\frac{\gamma_0|S|^2(S+S^*)-2E_{un}(S^2+S^{*2})}{2E_{un}\gamma_1\Gamma\pm 4\gamma_0^2|S|^2}, \quad (4.9)$$

where E_{un} is the "unperturbed" energy given by (4.7). Since in the vertical edges $S=0$, $\epsilon=0$ there both inside and out, and consequently there is no overlap on these edges. Also, ϵ vanishes identically in the planes $k_z=\pm 1/2c$. Thus, at the only points at which the energy is continuous on crossing the boundary of the zone, $\epsilon=0$, and it is also identically zero in two directions at right angles through this point. This alone makes it seem likely that the addition of ϵ will not give rise to any overlapping of the zones. More detailed consideration shows that such is in fact the case.

It should be noted finally that the two energy bands corresponding to the zones considered above arise from the same energy level (corresponding to the $2p$-state for *C*). The "splitting" of the energy level into *two* bands when the C

atoms are brought together to form the crystal is caused by the fact that the graphite crystallizes in a form having more than one atom per unit cell. Thus, the general properties of the zones (and in particular their touching) does not depend on the details of the potential field, but rather on the geometrical form of the lattice.

5. NUMBER OF FREE ELECTRONS IN GRAPHITE

The first problem is to find $N(E)$, the distribution of energy levels. The well-known formula for this is

$$N(E)=2V\int\frac{d\sigma}{|\mathrm{grad}_k E|},$$

where V is the volume of the crystal, and the integral is taken over the surface on which the energy has the constant value E. The formula may be readily transformed to

$$N(E)=2V\int\frac{dk_x dk_y}{(\partial E/\partial k_z)_{\text{surface}}}, \qquad (5.1)$$

the integral now being taken over the projection of the surface $E=$constant on the (k_x-k_y) plane.

Throughout this and the subsequent sections we shall consider only the exchange integrals γ_0 and γ_1 (nearest neighbors in and between planes).

Let us write (4.7)

$$\epsilon=E-E_0=-\gamma_1\cos\pi k_z c \pm(\gamma_1^2\cos^2\pi k_z c+\gamma_0^2|S|^2)^{\frac{1}{2}}. \qquad (5.2)$$

Calculating $\partial\epsilon/\partial k_z$ and eliminating k_z we get, for $2\gamma_1>\epsilon>0$,

$$\left(\frac{\partial\epsilon}{\partial k_z}\right)_{\text{surface}}=\frac{1}{2}\frac{\epsilon c}{\gamma_0^2|S|^2+\epsilon^2}\times(4\gamma_1^2\epsilon^2-(\gamma_0^2|S|^2-\epsilon^2)^2)^{\frac{1}{2}}. \qquad (5.3)$$

Now we shall be interested in $\epsilon\approx kT\ll\gamma_0$. In this case we may write

$$|S|^2=3\pi^2(k_x^2+k_y^2)a^2=u.$$

The integral (5.1) may be transformed to an integral over u:

$$N(E)=\frac{4V}{3\pi a^2 c\epsilon}\int_0^{(\epsilon^2+2\epsilon\gamma_1)/\gamma_0^2}\frac{(\gamma_0^2u+\epsilon^2)du}{(\gamma_1^2\epsilon^2-\frac{1}{4}(\gamma_0^2u-\epsilon^2)^2)^{\frac{1}{2}}}$$

which yields, on evaluation

$$N(E)=\frac{8V}{3\pi a^2 c\gamma_0^2}\left[(4\gamma_1^2-\epsilon^2)^{\frac{1}{2}}+|\epsilon|\pi+2\epsilon\sin^{-1}\frac{\epsilon}{2\gamma_1}\right]; \qquad (5.4)$$

the result has been extended to the case $\epsilon<0$ by observing that it is, for $\epsilon\ll\gamma_0$, *even* in ϵ.

The result (5.4) holds only for $\epsilon<2\gamma_1$. Coulson[3] has estimated that $\gamma_1\approx\frac{1}{10}\gamma_0=0.09$ ev. This corresponds to a temperature of nearly 1000°C, so that, insofar as calculations of the properties of graphite near room temperature are concerned, the expression (5.4) will be adequate.

It should be noticed that $N(E)$ does not go to zero when $\epsilon\to0$, but approaches a finite value proportional to γ_1 (see Fig. 12). Nevertheless, as can easily be seen, at the absolute zero of temperature the number of free electrons is zero.

The number of free electrons is in fact approximately

$$N_{\text{eff}}=2\int_0^{2\gamma_1}N(E)f(E)dE,$$

where

$$f(E)=\frac{1}{e^{\epsilon/kT}+1},$$

as in the case of the plane layer. Now with small error we may expand $N(E)$:

$$N(E)=\frac{8V\gamma_1}{3\pi a^2 c\gamma_0^2}\left[2+\frac{|\epsilon|}{\gamma_1}\pi+\frac{3}{4}\frac{\epsilon^2}{\gamma_1^2}+O\left(\frac{\epsilon^4}{\gamma_1^4}\right)+\cdots\right]$$

and extend the integral from 0 to ∞. Doing

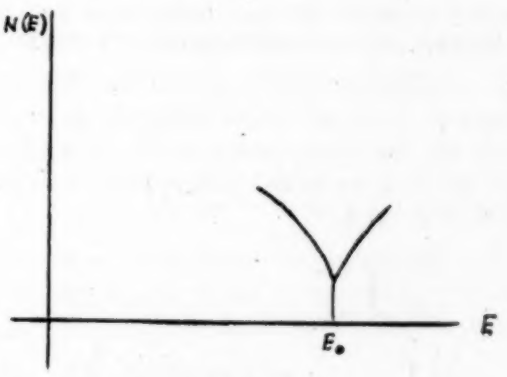

FIG. 12.

this we obtain

$$N_{eff}=\frac{32V}{3\pi a^2c}\frac{kT\gamma_1}{\gamma_0^2}\left[s_1+\frac{\pi}{2}\frac{kT}{\gamma_1}s_2+\frac{3}{4}\left(\frac{kT}{\gamma_1}\right)^2 s_3+O\left(\left(\frac{kT}{\gamma_1}\right)^3\right)+\cdots\right] \quad (5.5)$$

where

$$s_n=\sum_{m=0}(-1)^m\frac{1}{(m+1)^n}; \quad (5.6)$$

$s_1=\log 2$, $s_2=\pi^2/12$, etc., the s_n's being tabulated in Dale's *Mathematical Tables*.

Now the number of free electrons per atom is $n_{eff}=N_{eff}/N_a$, N_a being the number of atoms. Since the atomic volume is $\sqrt{3}a^2c/8$,

$$N_a=8V/\sqrt{3}a^2c.$$

So

$$n_{eff}=\frac{4}{\sqrt{3}\pi}\frac{kT\gamma_1}{\gamma_0^2}\left[s_1+\frac{\pi}{2}\frac{kT}{\gamma_1}s_2+\frac{3}{2}\left(\frac{kT}{\gamma_1}\right)^2 s_3+O\left(\left(\frac{kT}{\gamma_1}\right)^3\right)+\cdots\right] \quad (5.7)$$

$$=2.25\times10^{-3}$$

at room temperature. This is not at all in agreement with the value of 2.3×10^{-4} obtained by treating a single hexagonal layer; in fact, the dependence of n_{eff} on T is quite different in the two cases. On the other hand, as we shall see in the next section, the conductivities in the plane agree to the first order. Thus the discrepancy is merely caused by our definition of n_{eff}, and is compensated by a corresponding change in m_{eff}, the effective mass.

6. CONDUCTIVITY IN THE DIRECTION OF THE LAYERS AND PERPENDICULAR TO THEM

By a procedure closely parallelling that used in Section 3 for the single hexagonal layer, we obtain for the conductivity in the direction of the vector $\mathbf{u}$, if we assume that τ does not depend significantly on k,

$$\sigma(\mathbf{u})=-\frac{2e^2\tau}{h^2}\int\frac{df_0}{dE}\times\left[\int_{E=\text{const}}(\mathbf{u},\mathbf{n})^2|\text{grad}_k E|\,dS_k\right]dE, \quad (6.1)$$

where $\mathbf{n}$ is the normal to the surface $E=$constant and dS_k is the element of area in this surface. Averaging over-all directions in the plane and putting $dS_k=8\pi\kappa d\kappa/v_z$, where $\kappa^2=\kappa_x^2+\kappa_y^2$,

$$\sigma_{11}=-\frac{e^2\tau}{h^2}\int\frac{df_0}{dE}\left[\int_{(E)}\frac{(\partial E/\partial\kappa)^2}{\partial E/\partial k_z}8\pi\kappa d\kappa\right]dE. \quad (6.2)$$

On the other hand, the conductivity perpendicular to the layers is

$$\sigma_\perp=-\frac{2e^2\tau}{h^2}\int\frac{df_0}{dE}\left[\int_{(E)}\frac{\partial E}{\partial k_z}8\pi\kappa d\kappa\right]dE. \quad (6.3)$$

On the surface $\epsilon=$constant,

$$\frac{\partial\epsilon}{\partial\kappa}=\frac{2\epsilon\gamma_0^2(3\pi^2a^2y)^{\frac{1}{2}}}{\gamma_0^2y+\epsilon^2}, \quad (6.4)$$

where $3\pi^2(k_x^2+k_y^2)a^2=y$.

Now in the Eq. (5.2), if we remain within the limit $|\epsilon|<\gamma_1$, $|S|^2$ may be replaced by y with an error of order $(\gamma_1/\gamma_0)^2\approx1$ percent. In terms of y, the integral in the square bracket of (6.2) may be written

$$\frac{16\epsilon\gamma_0^4}{c}\int_0^{(\epsilon^2+2\epsilon\gamma_1)/\gamma_0^2}\frac{ydy}{(\gamma_0^2y+\epsilon^2)[4\epsilon^2\gamma_1^2-(\gamma_0^2y-\epsilon^2)^2]^{\frac{1}{2}}}.$$

On evaluation this yields

$$\frac{8\epsilon}{c}\left\{\pi+2\sin^{-1}\frac{\epsilon}{2\gamma_1}-\frac{\epsilon}{[\gamma_1^2-\epsilon^2]^{\frac{1}{2}}}\times\left[\log\frac{\epsilon+\gamma_1-[\gamma_1^2-\epsilon^2]^{\frac{1}{2}}}{\epsilon+\gamma_1+[\gamma_1^2+\epsilon^2]^{\frac{1}{2}}}-\log\frac{[4\gamma_1^2-\epsilon^2]^{\frac{1}{2}}-[\gamma_1^2-\epsilon^2]^{\frac{1}{2}}-\gamma_1}{[4\gamma_1^2-\epsilon^2]^{\frac{1}{2}}+[\gamma_1^2-\epsilon^2]^{\frac{1}{2}}-\gamma_1}\right]\right\}. \quad (6.4a)$$

Let us note first that if we take only the leading term in this expression, we get

$$\sigma_{11}\doteq-\frac{8\pi e^2\tau}{h^2c}\int\frac{df_0}{dE}\epsilon dE=\frac{16\pi e^2\tau}{h^2c}kT\log 2 \quad (6.5)$$

which is precisely what we obtained in (3.12) for the case of a single plane layer. It follows from

this and (5.7) that to the first order the effective mass for electrons in motion parallel to the layers is independent of temperature. Taking account of the higher terms does not change the result drastically for moderate temperatures; at room temperature ($T=293°$C) we get, using the numerical values already indicated (including the value for l assumed in Section 3),

$$\sigma_{\parallel}^{-1}=\rho_{\parallel}=5.3\times10^{-5}\text{ ohm-cm.}$$

Turning now to $\sigma_{\perp}$, we get for the integral in the square bracket in (6.3)

$$\frac{8}{3}\frac{\epsilon^2\gamma_1 c}{\gamma_0^2a^2}\Big[\frac{\epsilon}{\gamma_1}\Big(\frac{\pi}{2}+\sin^{-1}\frac{\epsilon}{2\gamma_1}\Big)-\Big[1-\frac{\epsilon^2}{4\gamma_1^2}\Big]^{\frac{1}{2}}+\Big[1-\frac{\epsilon^2}{\gamma_1^2}\Big]^{\frac{1}{2}}\Big(\log\frac{\epsilon+\gamma_1-[\gamma_1^2-\epsilon^2]^{\frac{1}{2}}}{\epsilon+\gamma_1+[\gamma_1^2-\epsilon^2]^{\frac{1}{2}}}-\log\frac{[4\gamma_1^2-\epsilon^2]^{\frac{1}{2}}-[\gamma_1^2-\epsilon^2]^{\frac{1}{2}}-\gamma_1}{[4\gamma_1^2-\epsilon^2]^{\frac{1}{2}}+[\gamma_1^2-\epsilon^2]^{\frac{1}{2}}-\gamma_1}\Big)\Big] \tag{6.6}$$

valid up to $\epsilon=\gamma_1$. We shall neglect the contribution to (6.3) from beyond this point. To determine first the order of magnitude of the result, consider the leading term only under the bracket; this is $\log\gamma_1/\epsilon$. Then we get

$$\sigma_{\perp}\approx-\frac{16}{3}\frac{e^2\tau}{h^2}\frac{\gamma_1 c}{\gamma_0^2a^2}\int_{-\gamma_1}^{\gamma_1}\epsilon^2\log\frac{\gamma_1}{|\epsilon|}\frac{\partial f_0}{\partial\epsilon}d\epsilon \approx\frac{16\pi^2}{9}\frac{e^2\tau}{h^2}\frac{c}{a^2}\frac{\gamma_1(kT)^2}{\gamma_0^2}\log\frac{\gamma_1}{kT}. \tag{6.6}$$

This expression will give a good approximation only at temperatures somewhat below room temperature. We will use it, however, to indicate orders of magnitude. It gives for the anisotropy factor

$$\frac{\sigma_{\perp}}{\sigma_{\parallel}}\doteqdot\frac{\pi}{9\log2}\frac{c^2}{a^2}\frac{\gamma_1 kT}{\gamma_0^2}\log\frac{\gamma_1}{kT} \approx0.01\text{ at room temperature.} \tag{6.7}$$

Since this does not involve τ it is completely calculable without assumptions about mean free path.

A comparison of the formulas (5.5) and (6.5) gives

$$m_{\text{eff}}^{\parallel}=2h^2\gamma_1/3\pi^2a^2\gamma_0^2$$

for the "mean effective mass" of electrons moving parallel to the graphite planes. This is valid so long as $kT\ll\gamma_1$, and is equal to $\approx\frac{1}{3}$. Similarly, from (5.5) and (6.6) we obtain for the mean effective mass for motion across the graphite planes

$$m_{\text{eff}}^{\perp}=\frac{24\log2\cdot h^2}{\pi c^2kT\log\gamma_1/kT}.$$

With decreasing temperature this increases as $1/T|\log T|$, becoming infinite as $T\to0$. At room temperature its value is ≈25 to 30 electron masses.

More accurate calculation of $\sigma_{\perp}$ by numerical integration at room temperature gives

$$\sigma_{\perp}^{-1}=\rho_{\perp}=4.8\times10^{-3}\text{ ohm-cm,}$$

and therefore

$$\frac{\sigma_{\perp}}{\sigma_{\parallel}}=\frac{\rho_{\parallel}}{\rho_{\perp}}=1.1\times10^{-2}.$$

It is of interest to note that the anisotropy depends on temperature, the ratio $\rho_{\perp}/\rho_{\parallel}$ becoming larger, i.e., the anisotropy becoming greater, with decreasing temperature. An attempt to confirm this prediction experimentally would be interesting; the measurement of $\sigma_{\perp}$ would, however, necessarily be difficult.

In Fig. 13 is plotted a graph of the ratio $\sigma_{\perp}/\sigma_{\parallel}$ for temperatures up to room temperature.

7. REMARKS ON OTHER PROPERTIES

Several qualitative remarks can be made about the magnetic susceptibility and the volume absorption properties of graphite. Graphite is strongly diamagnetic, and the diamagnetic susceptibility of single crystals can be expected to show marked anisotropy. For a field in the z-direction, the susceptibility depends on the value of the quantity

$$\frac{\partial^2\epsilon}{\partial k_z^2}\frac{\partial^2\epsilon}{\partial k_y^2}-\Big(\frac{\partial^2\epsilon}{\partial k_x\partial k_y}\Big)^2$$

over energy surfaces in the neighborhood of the boundary of the Fermi distribution, that is to say, near the zone boundary.[5] This is a large

[5] See Seitz, *Modern Theory of Solids*, pp. 594–595.

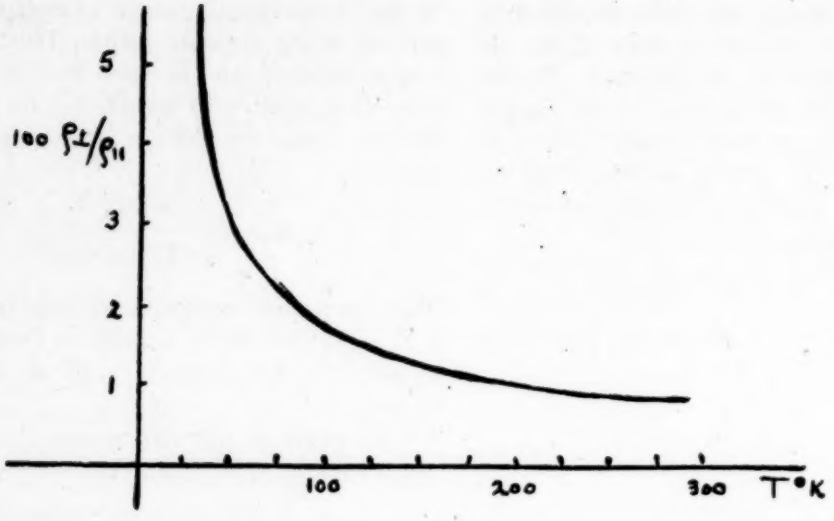

FIG. 13.

quantity, of order of magnitude $9\pi^4a^4\gamma_0^4/\gamma_1^2$, or about 6×10^4 times its value, $\hbar^4/m^2$, for free electrons. On the other hand, if the field is in the k_z-direction, say, the susceptibility depends on

$$\frac{\partial^2\epsilon}{\partial k_y^2}\frac{\partial^2\epsilon}{\partial k_z^2}-\left(\frac{\partial^2\epsilon}{\partial k_y\partial k_z}\right)^2.$$

Unlike the preceding case, this depends on T. It is, in fact, $\approx 3\pi^4a^2c^2kT\gamma_0^2/\gamma_1$, or $\approx kT\gamma_1/\gamma_0^2$ times the value for the field across the graphite planes. The difference may be ascribed to the difference in effective masses in the quantized orbits perpendicular to the field. The anisotropy is, therefore of the same order of magnitude as that of the conductivity.

Our other remark concerns the "optical" absorption spectrum. It is well known[6] that electrons may under the influence of radiation make only "vertical" transitions in the reduced-zone scheme, that is, transitions in which the wave vector changes by one of the vectors of the inverse lattice. Let us then consider extreme cases. A transition from a point such as V (Fig. 9) involves zero-energy change. The greatest energy jump is from the center of the zone (O in Fig. 9) to a point at the middle of a vertical edge defining a "corner" of the star-shaped second zone. This is of amount $2[\gamma_1^2+9\gamma_0^2]^{\frac{1}{2}}\approx 6\gamma_0$. Transitions involving all intermediate energies are possible.

An energy jump of $6\gamma_0$ corresponds to a frequency of 1.31×10^{15} or a wave-length of about 2300A, fairly deep in the ultraviolet. Thus, there is absorption from the longest wave-lengths through the visible spectrum and a substantial part of the ultraviolet. At the extreme limits absorption will be weak, however, due to the small number of states involved. The greatest number of states will correspond to energies such as those at the mid-points of the sides of the zone, which will give rise to transitions with energy jumps of the order of $2\gamma_0$. Thus we should expect the strongest absorption to be in the neighborhood of 6900A, i.e., in the red end of the spectrum.

[6] Reference 5, Section 71, pp. 326–8.

ACKNOWLEDGMENTS

I wish to thank Professor N. F. Mott of Bristol University for valuable discussions, and Professor C. A. Coulson of Oxford University for communicating to me some preliminary results of as yet unpublished work.

Two Applications of the Variational Method to Quantum Mechanics

WALTER KOHN
*Department of Applied Mathematics, University of Toronto, Toronto, Canada**
(Received September 23, 1946)

By using the unperturbed wave function with a variable scale factor as trial-function for a perturbed Schroedinger equation, a lower bound for the second-order perturbation energy of the ground state in terms of the unperturbed and first-order perturbation energy is obtained. A minimum property of the sum of the n lowest proper values is utilized in a new method for obtaining higher proper values and functions.

1. INTRODUCTION

IN most practical problems of quantum mechanics the Schroedinger equation,

$$H\psi = E\psi, \tag{1}$$

cannot be solved explicitly, and one must take recourse to approximation methods.

The present note, which is based on the method of Ritz, contains (1) an estimate of the second-order perturbation energy in terms of the unperturbed and first-order perturbation energy; and (2) a new approach to the evaluation of the proper values and functions of higher energy states.

2. SCALE FACTOR AND SECOND-ORDER PERTURBATION ENERGY

We write the Hamiltonian of a perturbed system as

$$H = T(x) + V(x) + kv(x), \tag{2}$$

where

x represents the coordinates of the system;

$T(x) = -\Sigma \frac{\hbar^2}{2m}\frac{\partial^2}{\partial x^2}$ is the kinetic energy operator, m representing the masses of the particles;

$V(x)$ is the potential energy operator of the unperturbed system; and

$kv(x)$ is the perturbing potential energy operator.

It follows from the definition of $T(x)$ that

$$T(x/\lambda) = \lambda^2 T(x), \tag{3}$$

and if we confine ourselves to electrostatic potentials, then

$$V(x/\lambda) = \lambda V(x), \quad v(x/\lambda) = \lambda v(x). \tag{4}$$

The first-order perturbation energy, ϵ_1, of the ground state is obtained by substituting its unperturbed, normalized wave function, ψ_0, into the expression

$$E = \int \psi^* H \psi dx.^1 \tag{5}$$

Thus, if we denote the unperturbed energy by E_0, we have

$$\int \psi_0^* H \psi_0 dx = E_0 + k\epsilon_1, \tag{6}$$

where

$$\epsilon_1 = \int \psi_0^* v(x) \psi_0 dx. \tag{7}$$

Now let us take as trial-function the (normalized) function $\lambda^{3n/2}\psi_0(\lambda x)$, where $3n$ is the dimension of the configuration space and λ is to be adjusted to minimize E. Making use of (3) and (4) we obtain

$$E = \int \psi_0^*(\lambda x)[T(x) + V(x) + kv(z)]\psi_0(\lambda x) d(\lambda x)$$

$$= \int \psi_0^*(x)\left[T\left(\frac{x}{\lambda}\right) + V\left(\frac{x}{\lambda}\right) + kv\left(\frac{x}{\lambda}\right)\right]\psi_0(x)dx \tag{8a}$$

or

$$E = \lambda^2 \int \psi_0^*(x) T(x) \psi_0(x) dx + \lambda \int \psi_0^*(x) V(x) \psi_0(x) dx + \lambda k \int \psi_0^*(x) v(x) \psi_0(x) dx. \tag{8b}$$

* At present in the Department of Physics, Harvard University, Cambridge, Massachusetts.

[1] The integral to be taken over the configuration space.

The first and second integrals in (8b) represent, respectively, the average kinetic and potential energy of the unperturbed system. According to the Virial theorem in quantum-mechanics,[2] these are equal to $-E_0$ and $2E_0$, respectively. Thus (8b) may be rewritten as

$$E=-E_0\lambda^2+(2E_0+k\epsilon_1)\lambda. \tag{9}$$

Minimizing with respect to λ we obtain

$$\lambda=1+k\epsilon_1/2E_0, \quad E=E_0+k\epsilon_1+k^2\epsilon_2', \tag{10}$$

where

$$\epsilon_2'=\epsilon_1^2/4E_0. \tag{11}$$

The term $k\epsilon_1$ is just the first-order perturbation energy. The next term, $k^2\epsilon_2'$, is negative and therefore improves our estimate of E.

Furthermore, ϵ_2' is (in absolute value) a lower bound of the second-order perturbation energy, ϵ_2. For, if we subtract the true perturbed energy,

$$E_p=E_0+k\epsilon_1+k^2\epsilon_2+k^3\epsilon_3+\cdots \tag{12}$$

from E, as given by (10), we find

$$E-E_p=k^2(\epsilon_2'-\epsilon_2)-k^3\epsilon_3-\cdots, \tag{13}$$

and remembering now that E is an upper bound of E_p we obtain, on letting k tend to 0, $\epsilon_2'\geqslant\epsilon_2$. Since ϵ_2' is negative this proves our statement.

In summary we may say that if one chooses as trial-function for a perturbed system the unperturbed wave function of the normal state, but with an adjustable scale-factor, the variational method leads to an energy which agrees with the perturbed energy to the first order and in addition contains a correction in terms of the first order and unperturbed energy (see (11)), which is a lower bound of the second-order perturbation energy.

Example: The Helium 1^1S Term

Hylleraas[3] derived the expression

$$E_p=-2Z^2+1.25Z^2\left(\frac{1}{Z}\right)-0.3149Z^2\left(\frac{1}{Z^2}\right)+\cdots \tag{14}$$

for the normal state of a helium-like atom of nuclear charge Ze.

Here $1/Z$ corresponds to our k so that $E_0=-2Z^2$, $\epsilon_1=1.25Z^2$, and $\epsilon_2=-0.3149Z^2$. Our correction term,

$$\epsilon_2'=(1.25Z^2)^2/(-8Z^2)=-0.1953Z^2, \tag{15}$$

accounts for 62 percent of ϵ_2.

3. HIGHER ENERGY STATES

In applying the Ritz method to a higher energy state only functions orthogonal to all lower proper functions may be admitted for competition. Unfortunately, the task of assuring orthogonality is, in general, prohibitively complicated.

Hylleraas and Undheim[4] have used the fact that the nth root of a secular determinant is an upper bound of the nth proper value, to approximate the 2^1S term of helium. However, their method is in practice quite cumbersome and only slowly convergent.

As an alternative we shall derive an expression for the nth energy state whose properties are analogous to (5): Its minimum value is the nth proper value and the function which leads to this minimum gives us the nth proper function.

Our method is based on the following

Lemma[5]

Let $\psi_1, \psi_2, \cdots\psi_n$ be the n lowest normalized proper functions of (1) so that

$$E_i=\int\psi_i^*H\psi_i dx, \quad i=1, 2, \cdots n. \tag{16}$$

Further, let

$$H_{ii}=\int\varphi_i^*H\varphi_i dx, \quad i=1, 2, \cdots n, \tag{17}$$

where $\varphi_1, \varphi_2, \cdots\varphi_n$ are any normalized orthogonal functions. Then

$$E_1+E_2+\cdots E_n=\min.(H_{11}+H_{22}+\cdots H_{nn}), \tag{18}$$

where degenerate proper values are to be counted multiply. The minimum is attained whenever

[2] A. Sommerfeld, *Wave Mechanics* (Methuen and Company, London, 1930) p. 248.

[3] E. A. Hylleraas, Zeits. f. Physik 60, 624 (1930).

[4] E. A. Hylleraas and R. Undheim, Zeits. f. Physik 60, 759 (1930).

[5] Courant-Hilbert, *Meth. d. Math. Phys.* (Verlagsbuchhandlung, Julius Springer, Berlin, 1931), second edition, p. 399. No proof is given there but it can be easily supplied by expanding the $\varphi-s$ in terms of the $\psi-s$ and thence deriving expressions for H_{ii} in terms of the E_i.

$\varphi_1, \varphi_2, \cdots \varphi_n$ arise out of $\psi_1, \psi_2, \cdots \psi_n$ by an orthogonal transformation.

An application to the estimation of higher proper values suggests itself immediately.

Let φ_1 be a normalized approximation to the lowest proper function of (1) and let φ_2 be an arbitrary function. Then the functions φ_1 and

$$\bar{\varphi}_2 = (\varphi_2 - I_1\varphi_1)/(N^2 - I_1^2)^{\frac{1}{2}}, \tag{19}$$

with

$$N^2 = \int \varphi_2^* \varphi_2 dx, \quad I_1 = \int \varphi_1^* \varphi_2 dx \tag{20}$$

are normal and orthogonal. Consequently, by our lemma,

$$E_1 + E_2 = \min\left[\int \varphi_1^* H \varphi_1 dx + \int \bar{\varphi}_2^* H \bar{\varphi}_2 dx\right] \tag{21}$$

which leads to

$$E_2 = \min\left[H_{11} - E_1 + \frac{H_{22} - 2I_1H_{12} + I_1^2 H_{11}}{N^2 - I_1^2}\right], \tag{22}$$

where

$$H_{ij} = \int \varphi_i^* H \varphi_j dx. \tag{23}$$

We note that (22) does not involve the correct ψ_1 but only E_1 which can be easily and accurately estimated by the Ritz method.

The $\bar{\varphi}_2$'s for which the minimum is nearly reached are seen to be approximations to ψ_2.

For practical purposes (22) is rather complicated. It simplifies considerably when $\varphi_1 = \psi_1$, becoming

$$E_2 = \min\left[E + \frac{(E - E_1)I_1^2}{N^2 - I_1^2}\right], \text{ where } E = \frac{H_{22}}{N^2}. \tag{24}$$

Strictly speaking we are now obliged to use the exact wave function, ψ_1, for the computation of I_1. But fortunately, if φ_2 is well chosen, the "un-orthogonality integral" I_1 and consequently also the term following E in (24) are small. Therefore, to estimate E_2 great accuracy in the evaluation of I_1 is not necessary and a simple approximation of ψ_1 is quite sufficient.

For the nth energy state one obtains, in an analogous notation,

$$\bar{\varphi}_n = \left(\varphi_n - \sum_{i=1}^{n-1} I_i\varphi_i\right) \Big/ \left(N^2 - \sum_{i=1}^{n-1} I_i^2\right), \tag{25}$$

$$E_n = \min\left[\sum_{i=1}^{n-1}(H_{ii} - E_i) + \left(H_{nn} - 2\sum_{i=1}^{n-1} I_i H_{in} + \sum_{i=1}^{n-1}\sum_{j=1}^{n-1} I_i I_j H_{ij}\right) \Big/ \left(N^2 - \sum_{i=1}^{n-1} I_i^2\right)\right], \tag{26}$$

where $\varphi_1, \varphi_2 \cdots \varphi_{n-1}$ are any orthogonal functions and φ_n is arbitrary. In the special case when $\varphi_1 = \psi_1, \cdots \varphi_{n-1} = \psi_{n-1}$, we have

$$\bar{\varphi}_n = \left(\varphi_n - \sum_{i=1}^{n-1} I_i\psi_i\right) \Big/ \left(N^2 - \sum_{i=1}^{n-1} I_i^2\right), \tag{27}$$

$$E_n = \min\left[E + \left(\sum_{i=1}^{n-1}(E - E_i)I_i^2\right) \Big/ \left(N^2 - \sum_{i=1}^{n-1} I_i^2\right)\right]. \tag{28}$$

Example: The Helium 2^1S Term

To obtain an approximation to the wave function of the 2^1S state it was assumed that the "inner" and "outer" electrons move in coulomb fields corresponding, respectively, to $Z = 2$ and $Z = 1$. This led to the function

$$\varphi_2 = (\tfrac{1}{2}r_1 - 1)\exp - [\tfrac{1}{2}r_1] \exp - [2r_2] + (\tfrac{1}{2}r_2 - 1)\exp[\tfrac{1}{2}r_2] \exp - [2r_1], \tag{29}$$

where r_1 and r_2 denote distances from the nucleus. For the wave function of the ground state the approximation

$$\psi_1 \approx \frac{(27/16)^3}{\pi} \exp - \left[\frac{27}{16}(r_1 + r_2)\right] \tag{30}$$

was used.

Substitution of (29) and (30) into (24) gave -4.24 Ry as approximation to E_2. This is still considerably higher than the observed -4.29 Ry, but in view of the crudeness of our trial-function the improvement over the first-order perturbation value of -4.07 Ry may be considered satisfactory.

ACKNOWLEDGMENT

The author takes great pleasure in thanking Professor A. F. C. Stevenson for his kind advice and interest during the course of this investigation.

Letters to the Editor

PUBLICATION of brief reports of important discoveries in physics may be secured by addressing them to this department. The closing date for this department is, for the issue of the 1st of the month, the 8th of the preceding month and for the issue of the 15th, the 23rd of the preceding month. No proof will be sent to the authors. The Board of Editors does not hold itself responsible for the opinions expressed by the correspondents. Communications should not exceed 600 words in length.

Corona from Fine Positive Points

W. N. ENGLISH*
Department of Physics, University of California, Berkeley, California
April 8, 1947

THE work of A. F. Kip[1] has been extended to needle points of 0.002 mm radius of curvature. Three oscilloscopes were used to minimize the effect of amplifier pass band—a Navy type TS 28/UPN synchroscope and amplifier AM 73/UPA-1 (1000 cycles to 5 megacycles), a Dumont type 241 (20 cycles to 2 megacycles), and a Dumont type 171 (15 cycles to about 100 kilocycles) as used by Kip. Kip's observation of the degeneration of streamer pulses with decreasing point size, until indistinguishable from burst pulses, was found to be instrumental. Such pulses were clearly resolved on the synchroscope for the finest points, and very similar in duration and shape to streamer pulses for large points, when reduced to the same amplitude.

Dust-free points finer than about 0.01 mm radius of curvature gave no observable bursts or streamers. Corona onset was then evident on the oscilloscopes only by a slight and voltage-critical irregularity of the trace. Fine positive points dusted with MgO gave bursts and/or streamers at the onset voltage of the intermittent regime and above until steady corona occurred. The amplitude and frequency of the streamers varied somewhat from one dusting to another, and usually decreased with time, presumably because dust specks were removed from the critical region. This dust effect has been observed by Hudson[2] for smooth negative points as large as 0.25 mm radius.

Photographs of the discharge at the point were taken to establish a connection between the synchroscope pulses and "visible" (i.e., photographable) streamers. Some of these are shown in Fig. 1 while the corresponding synchroscope pulses are drawn to scale in Fig. 2. It is noteworthy

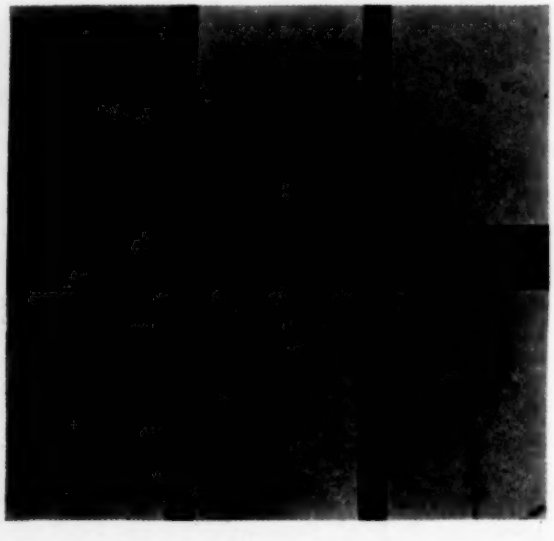

FIG. 1. Photographs of positive point streamers. Right to left, point radii of curvature: —0.002, 0.003, 0.003, 0.04, 0.1, 0.25 mm. Exposures 5 to 10 minutes at f:2.

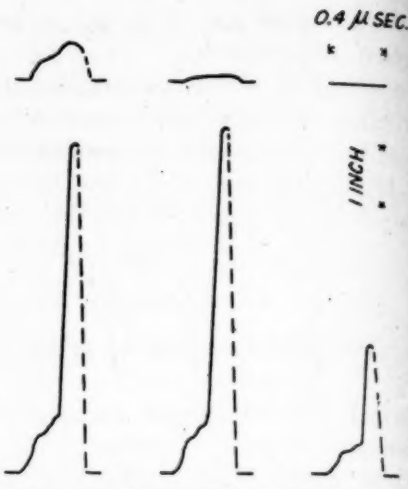

FIG. 2. Synchroscope pulses at 6000× amplification corresponding to photographs in Fig. 1. Sweep from right to left.

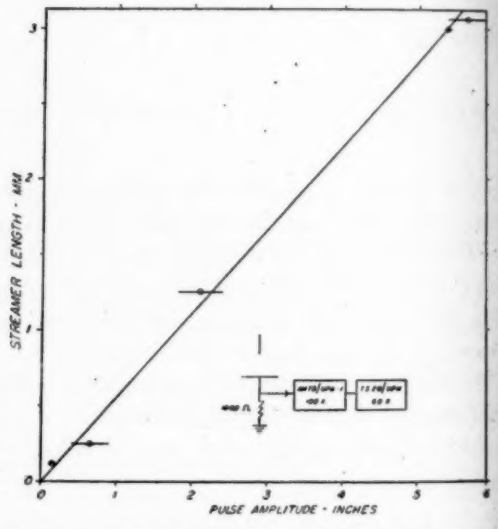

FIG. 3. Streamer length on photograph plotted against amplitude of synchronoscope pulse at 6000× amplification. Observed variation in pulse amplitude is indicated.

that all the streamer pulses are very closely of the same duration, 0.4 microsecond. A plot of pulse amplitude against "visible" streamer length, Fig. 3, shows that the charge per cm of streamer is essentially constant and independent of streamer length. Using an estimated pulse input impedance of 50 ohms, the slope of the curve gives a value of the charge per cm length of "visible" streamer of 10^{10} ions. This agrees well enough with the value found by Kip of 5×10^{9} ions per cm.

The radius of curvature of the steel needle points was measured from micro-photographs with up to 4500 times magnification. Values were checked among the points by plotting the onset voltages for intermittent corona. The experiments were done in room air at atmospheric pressure, with a 6-cm gap, and with 50 grams of thorianite ore at 12 cm from the point.

The results obtained indicate that streamers and bursts occur, and are clearly distinguishable for points down to 0.002 mm radius of curvature, provided dust specks are present on the point. With larger points the streamer pulses have much greater amplitude than the bursts (a factor of about 10, for 0.25 mm radius). Both streamer and burst pulses decrease in amplitude with decreasing point size until they are barely detected, but the streamer pulse maintains its form and 0.4 microsecond duration, while the burst pulse, which is a little bit of stable corona, can have any duration, usually 100 to 300 microseconds or greater.

The role of the MgO dust is not entirely clear. It may well be to provide triggering electrons, by the Paetow effect,[3] in the very small high field region. On the other hand, the variation of pulse size with different dustings suggests that the larger particles, which have a size comparable to the point size, may act to provide a less divergent field. This should cause a change in the intermittent regime onset, which has not been observed.

The writer is indebted to Professor L. B. Loeb for advice and encouragement.

* Eastman Kodak Fellow.
[1] A. F. Kip, Phys. Rev. 55, 549 (1939).
[2] L. B. Loeb, A. F. Kip, G. G. Hudson, and W. H. Bennett, Phys. Rev. 60, 714 (1941).
[3] L. B. Loeb, *Fundamental Processes of Electrical Discharge in Gases* (John Wiley and Sons, Inc., New York, 1939), p. 498

Inversion Spectrum of Ammonia

M. W. P. Strandberg, R. Kyhl, T. Wentink, Jr., and R. E. Hillger
Research Laboratory of Electronics, Massachusetts Institute of Technology, Cambridge, Massachusetts
April 5, 1947

COMPARISON of our[1] results on the frequencies of the lines in the $N^{14}H_3$ inversion spectrum, with those of Good and Coles,[2] show a discrepancy of 4.56 Mc/sec. in the $J=4$, $K=3$ line, which is well outside the experimental error. A study of our results has disclosed that a computational error was made in the reduction of the data, and our best value is 22,688.18 Mc/sec., which is in fair agreement with Good and Coles' value. This would change the value of the anomalous frequency shift for this line in Table II of reference 1, to +1.76 Mc/sec.

It is interesting to note that if the data for the $N^{15}H_3$ lines, given by Good and Coles, for the $K=3$ transitions, are analysed in a manner similar to that in reference 1 for the $N^{14}H_3$ lines, corresponding anomalous frequency shifts for the two isotopic molecules are obtained.

		$\nu_{measured}$	$\nu_{predicted}$
J	K	$N^{14}H_3$	$N^{15}H_3$
3	3	−0.32 Mc/sec.	−0.30 Mc/sec.
4	3	+1.76	+1.83
5	3	−6.96	−8.

[1] Strandberg, Kyhl, Wentink, and Hillger, Phys. Rev. 71, 326 (1947).
[2] W. E. Good and D. K. Coles, Phys. Rev. 71, 383 (1947).

Nuclear Quadrupole Moment Effects in the Microwave Spectrum of Ammonia

Richard J. Watts and Dudley Williams
The Ohio State University, Columbus, Ohio
March 27, 1947

THE hyperfine structure first observed in the inversion spectrum of ammonia by Good[1] has been the subject of much recent work. Coles and Good[2] have reported measuring the satellite separations for many of the lines and have published a formula which gives the expected separations of the satellite lines from the main lines. Professor Van Vleck[3] has also developed a theory of the hyperfine structure. According to these theories, the satellite lines can be explained in terms of the interaction between the electrical quadrupole of the N^{14} nucleus and the electrical field of the NH_3 molecule.

The intensity of the satellite lines decreases rapidly as the rotational quantum number J increases. Dailey *et al.*[3] have reported measurements of the satellites of lines with J values as high as 4 and find these to be in excellent agreement with Van Vleck's theory; but they have reported their inability to detect satellite lines for J values higher than 4.

Recently, we have made a study of the ammonia spectrum and have been able to observe and measure the relative separations of satellites from main lines with J as high as 7. The results for lines 11, 22, 33, and 44 are in agreement with Dailey's results and the relative separations of all lines observed agree with Van Vleck's theory. Our preliminary results are summarized in Table I. A more detailed account of this work will be published in the near future.*

Table I. Observed and calculated ratios of satellite displacements.

Line JK	Observed ratio $\Delta\nu'/\Delta\nu$	Calculated ratio $\Delta\nu'/\Delta\nu$
11	2.55	2.50
22	1.56	1.56
33	1.36	1.35
44	1.28	1.26
55	1.21	1.20
66	1.18	1.17
76	1.19	1.14

[1] W. E. Good, Phys. Rev. 70, 213 (1946).
[2] D. E. Coles and W. E. Good, Phys. Rev. 70, 979 (1946).
[3] Dailey, Kyhl, Strandberg, Van Vleck, and Wilson, Phys. Rev. 70, 984 (1946).
* This work is being done in connection with a research project sponsored by the Watson Laboratories of the Air Material Command, Red Bank, New Jersey.

Microwave Spectra: The Hyperfine Structure of Ammonia*

WALTER GORDY AND MYER KESSLER
Department of Physics, Duke University, Durham, North Carolina
April 2, 1947

USING a 12-meter wave-guide cell, a sensitive detecting system, and a pressure of approximately 10^{-3} mm Hg, we have re-examined[1] $N^{14}H_3$ spectra in the region of 1.25 cm, with the result that the small satellites of certain of the lines first detected by Good[1] are strikingly resolved. The upper curve in the accompanying photograph (Fig. 1) is a cathode-ray scope display of the 3,3 line[2] with its satellite pairs on opposite sides. These satellites are believed[3] to be a splitting of the center line by the nuclear quadrupole moment of N^{14}. The wide separation of the satellite pair which are only about 0.6 Mc apart, illustrates the remarkable resolution now obtainable with electronic techniques in the microwave region. We have also made photographs showing the similar splitting in the 1,1; 2,2; 4,4; 5,5; 6,6; and 8,8 lines.[3] The lower curve in the figure shows that obtained for the 6,6 line. The satellites are closest to the center line for the 1,1 case and move out from the center line as the quantum numbers of angular momenta increase. Accurate measurements of their positions[4] are being made and will be reported later. The intensity of the satellites, as compared with that of the center line, decreases with increasing quantum numbers of angular momenta. We have not yet photographed the fine structure of the 7,7 and 9,9 lines because our oscillator would not operate in their regions. We observed several strong lines for which J and K are unequal but did not detect any satellite structure.[3]

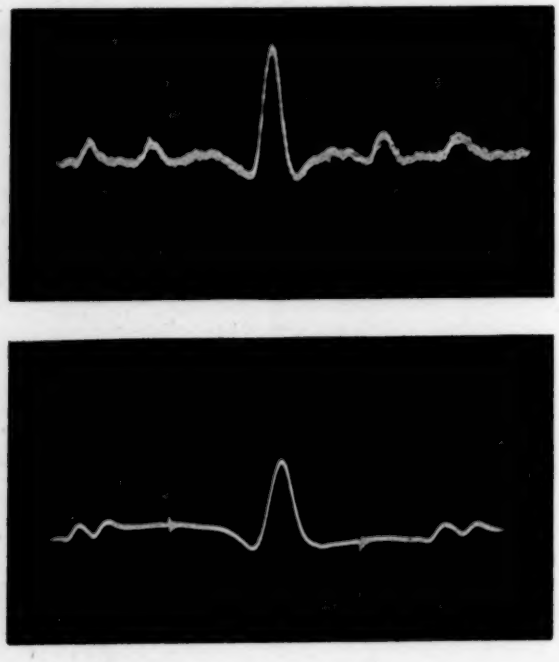

FIG. 1. Upper curve: 3,3 line of ammonia with satellite structure. Lower curve: 6,6 line, with satellite structure. Pressure $\approx 10^{-3}$ mm of Hg.

In this work we did not observe the broadening caused by saturation which was reported by Townes.[1] The sharp lines shown in the photographs were observed when approximately 10 milliwatts of power were flowing through the cell.

These results were obtained by a single crystal, unbalanced detecting system which we have evolved. In brief, we use a slowly changing reflector voltage to modulate the source and a low frequency filter in the amplifier so that the indicator does not respond to the gradual change of voltage over the envelope of the oscillator mode but is very sensitive to the abrupt changes in output caused by the sharp absorption lines. This system has the additional advantage that spurious signals caused by reflections are largely eliminated, since they are usually much broader than the absorption lines of a gas at low pressure. Our tests indicate that this system is superior to the balanced detectors which employ either two crystals and cancellation in the video stage or a single crystal and cancellation in the r-f stage.

* This research was supported by a Frederick Gardner Cottrell Special Grant from the Research Corporation and by a loan of equipment from the Office of Research and Invention, United States Navy.

[1] C. E. Cleeton and N. H. Williams, Phys. Rev. 45, 234 (1934); B. Bleamy and Penrose, Nature 157, 339 (1946); W. E. Good, Phys. Rev. 70, 213 (1946); C. H. Townes, Phys. Rev. 70, 665 (1946); M. W. P. Strandberg, R. Kyhl, T. Wentink, Jr., and R. E. Hillger, Phys. Rev. 71, 326 (1947).

[2] Strandberg, Kyhl, Wentink, and Hillger (reference 1) and W. E. Good and D. K. Coles (Phys. Rev. 71, 383 (1947)) have provided accurately measured frequencies of the centers of the first six of these lines.

[3] B. P. Dailey, R. L. Kyhl, M. W. P. Strandberg, J. H. Van Vleck, and E. B. Wilson, Jr., Phys. Rev. 70, 984 (1946); D. K. Coles and W. E. Good, Phys. Rev. 70, 979 (1946).

[4] Dailey, Kyhl, Strandberg, Van Vleck, and Wilson (reference 3) have measured the satellite separations for the 1,1; 2,2; 3,3; and 4,4 lines.

Bond Distances in OCS from Microwave Absorption Lines

T. W. DAKIN, W. E. GOOD, AND D. K. COLES
Westinghouse Research Laboratories, East Pittsburgh, Pennsylvania
April 8, 1947

THE rotational absorption line for the $J=1$ to $J=2$ rotational transition of the OCS linear molecule was reported by Dakin, Good, and Coles.[1] Absorption at higher pressures caused by the transition had been reported previously by Hershberger.[2] The absorption line reported above was caused by the molecule composed of the abundant isotopes: carbon 12, oxygen 16, and sulfur 32. Of these three elements, only sulfur has another isotope with an abundance of more than 1 percent of the total naturally occurring element. The sulfur isotope 34 has an abundance of about 3 percent. It was believed that the sensitivity of our microwave absorption apparatus described by Good,[3] with a wave-guide absorption cell 36 feet long, was just about enough to detect the absorption line caused by the OCS molecule with the sulfur 34 isotope, and after a preliminary calculation of the approximate frequency of this line, using the bond distances reported by Cross and Brockway,[4] it was searched for and eventually found. The resolution of this isotopic absorption line was

TABLE I. Data on bond distances in OCS.

Constant	Value	Effect of uncertainty on CO distance	Effect of uncertainty on CS distance
Atomic weight S^{32}	31.9823±0.00030	±0.00002 $\times10^{-8}$ cm	∓0.00002 $\times10^{-8}$ cm
Atomic weight C^{12}	12.003861±0.000024	±0.00005	∓0.00004
Atomic weight O^{16}	16.0000		
Atomic weight difference $S^{34}-S^{32}$	1.9957±0.002	±0.0047	∓0.0038
Mass of atom of unit atomic weight	(1.66035±0.00031) $\times10^{-24}$ g	∓0.00011	∓0.00015
Planck's Constant	(6.6242±0.0024) $\times10^{-27}$ erg sec.	±0.00022	±0.00030
Calculated values from the observed frequencies:			
Moment of inertia (S^{32} molecule)	(137.9540±0.0001) $\times10^{-40}$ g cm²	±0.000009	∓0.000005
Moment of inertia difference (S^{34} mole−S^{32} mole)	(3.4564±0.0003) $\times10^{-40}$ g cm²	∓0.00075	±0.00062
Probable error		±0.0058	±0.0049

first reported by us at the National Research Council Conference on Insulation in November, 1946.

The frequencies of these two absorption lines have since been measured more accurately by comparison with a harmonic of an oscillator which was heterodyned to zero beat with the 5-megacycle WWV National Bureau of Standards station as used by Good and Coles.[5] The frequencies of the absorption lines can thus be determined to about one part per million. They are $f(S^{32}\text{ line})=24{,}325.92\pm0.02$ Mc/sec., $f(S^{34}\text{ line})=23{,}731.33\pm0.03$ Mc/sec. Unfortunately, because the nature of the calculation and the uncertainty of other constants necessary, all of this accuracy is not available in the two bond distances which may be calculated from these two frequencies.

In Table I there is a list of all the constants used in the calculation of the bond distances from the frequencies. The values of these constants, together with their uncertainties are given, and the effect of these uncertainties on the calculated bond distances is given. It will be observed that in most cases the effect of the error is in the opposite direction on the two bond distances so that their sum can be calculated more accurately than either separately. It was hoped that this very accurate frequency measurement would give a much more accurate value of the bond distance. An examination of Table I shows that the principal uncertainty is the difference in atomic weight of the sulfur isotopes. This contributes by far the largest amount to the uncertainty of the bond distance. The possible error in the frequency difference between the absorption line of the two isotopic molecules is the next largest uncertainty.

The bond distances C−O, $(1.1612\pm0.0058)\times10^{-8}$ cm, and C−S, $(1.5604\pm0.0049)\times10^{-8}$ cm calculated here are the average interatomic distances in the lowest vibrational state. The atoms are assumed to be point masses and the centrifugal stretching has been approximated from the expressions given by Nielsen[6] and the vibrational frequencies of Penney and Sutherland[7] and found to be less than one part per million for the rotational levels involved here. The uncertainty in these bond distances can be reduced to about 0.1 percent when the difference in mass of the two sulfur isotopes is known to be better than ±0.0001 atomic weight units. The isotope atomic weight values used were obtained from the table of Evans.[8] The values of interatomic distances given here compare very well with the values obtained by Cross and Brockway from electron diffraction measurements: $C-O=1.16\pm0.02\times10^{-8}$ cm, $C-S=1.56\pm0.03\times10^{-8}$ cm.

[1] T. W. Dakin, W. E. Good, and D. K. Coles, Phys. Rev. 70, 560 (L) (1946).
[2] W. D. Hershberger, R.C.A. Review 7, 422 (1946); J. App. Phys. 17, 814 (1946).
[3] W. E. Good, Phys. Rev. 70, 213 (1946).
[4] P. C. Cross and L. O. Brockway, J. Chem. Phys. 3, 821 (1935).
[5] W. E. Good and D. K. Coles, Phys. Rev. 71, 383 (1947).
[6] A. H. Nielsen, J. Chem. Phys. 11, 160 (1943).
[7] W. G. Penney and G. B. B. M. Sutherland, Proc. Roy. Soc. 156, 654 (1936).
[8] R. D. Evans, *Introduction to the Atomic Nucleus* (M.I.T. 1944).

High Energy Ions in Crystal Lattices

A. H. W. ATEN, JR.
Natuurkundig Laboratorium der N. V. Philips Gloeilampenfabrieken, Eindhoven, Nederland
April 7, 1947

MANY complex anions are known to give rise to a Szilard-Chalmers effect when irradiated with slow neutrons.[1] In the case of a perchlorate, after neutron capture the activity is found entirely in the chloride fraction. This means more than the simple fact that the recoil separates the central chlorine from its surrounding oxygens. It is customary to consider the ClO_4^- ion as having a composition intermediate between the formulae Cl^-O_4 and $Cl^{7+}(O^{2-})_4$, but either all the activated chlorine is ejected as negative ions or, if part is ejected with a positive charge or as a neutral atom, it takes up electrons before it can react with any of the oxygen in the lattice. In other cases (e.g., arsenates and arsenites) the radioactivity is found entirely in ions of the same formula as those of which the crystal consists. Thus the capture of a neutron by a nucleus causes either a chemical reduction or it leaves the valency of the activated ion unchanged. Comparison between different reactions of this type is complicated by the fact that both the chemical conditions of atoms ejected by recoil and their chances of subsequent reactions depend on the crystal lattice.

In a note giving some preliminary figures,[2] it has been pointed out that the position is quite different in case the radioactive nucleus originates from an (n,p) or an (n,α) reaction. If fast neutrons of normal energy are used in such a process the kinetic energy of the recoil of the activated nucleus is very roughly 100 to 1000 times as large as the energy of a nucleus which has captured a neutron. Now this energy is not only sufficient to break the chemical bonds which connect the activated atom with the surrounding oxygens but even to strip it of many of its electrons during a series of collisions with neighboring particles. The highest positive charge which the activated atom attains will depend on the energy it has been given by the nuclear reaction and will be influenced very little by the composition of the lattice. In general, this highly charged ion will be very unstable chemically, and after

losing its excess energy it will settle down in the lowest energy state it can reach in the crystal. Which compound will be formed during this process will depend on the chemical composition of the lattice. This makes it possible to compare the fate of the same activated monatomic ion in different crystals. In general, we may expect to find the products of (n,p) and of (n,α) reactions in a highly oxidized state. Apart from this, a large concentration of oxygen in the lattice will favor the formation of oxygen-rich anions. On the whole, the results of the measurements in Table I are in agreement with these conclusions.

TABLE I. Valency of radiophosphorus from sulfur and chlorine with fast neutrons. Fraction of total radiophosphorus (in phosphate+phosphite+hypophosphite) found in phosphite+hypophosphite in different crystals.

Crystals irradiated	Fraction of P^{32} found in phosphite +hypophosphite
K_2SO_4	0.09; 0.10; 0.10
K_2SO_4, dissolved in sulfite solution	0.09; 0.10
$Na_2SO_4 \cdot 10$ aq.	0.02; 0.02
$Na_2SO_3 \cdot 7$ aq.	0.50; 0.56
Na_2S hydrate	0.64; 0.78; 0.93; 0.93
$KClO_4$	0.01; 0.01
$KClO_3$	−0.01; 0.01
$MgCl_2$ hydrate	0.07
$MgCl_2$ hydrate dissolved in sulfite solution	0.02
NaCl	0.62; 0.68; 0.69

A radium-beryllium neutron source was used, and the irradiated products were dissolved in water containing phosphate, phosphite, and hypophosphite ions, and, in the case of potassium chlorate, ammonia. Separations were carried out as described by Libby, hypophosphite following the phosphite fraction. Although it remains to be investigated in how far the results depend on the time elapsed between the irradiation and the separation and on the temperature of the experiment, the good agreement between duplicates is sufficient proof of the reliability of the figures for comparative purpose (the value −0.01 found for $KClO_3$ was included in the table to give an idea of the degree of experimental accuracy). It is at present an open question whether the phosphate and phosphite ions are formed inside the lattice or whether they adopt their final state at the moment the crystal is dissolved. In this connection it is of interest that the presence of reducing sulfite ions does not influence the result.

In the NaCl crystal the primary product will consist of chlorine-phosphorus complexes, which hydrolyze when dissolved in water. Evidently the presence of oxygen in the $MgCl_2$ hydrate crystal favors the phosphate formation. In the Na_2S hydrate crystal many different types of thiophosphates will be formed which do not hydrolyze as easily as the chloro compounds. Their fate during the chemical separations will depend on absorption processes and will be quite irreproducible, as is seen clearly in the table. These figures for Na_2S hydrate are, of course, without meaning.

[1] W. F. Libby, J. Am. Chem. Soc. 62, 1930 (1940).
[2] A. H. W. Aten, Jr., Rec. Trav. Chim. Pays-Bas. 61, 467 (1942). Analogous considerations concerning organic compounds have been published by Yankwitch, Rollefson, and Norwick, J. Chem. Phys. 14, 131 (1946).

A Note Concerning the Motion of Arc Cathode Spots in Magnetic Fields*

R. L. LONGINI
Westinghouse Research Laboratories, Pittsburgh, Pennsylvania
February 17, 1947

A NUMBER of observers[1–3] have reported that low pressure arc cathode spots, when in a magnetic field, move in a direction opposite from what one might expect by an application of Ampere's law to the interaction of the magnetic field and arc current. The following explanation is consistent with the field emission theory of cathode spots[4] which requires a strong electric field at the cathode. This field is due to an excess of ions over electrons in the space between the plasma and the cathode. Electrons carry most of the current but, because of their relatively great velocity, have low density in this transition space[5] and therefore make only a secondary contribution to the electric field at the cathode. As the field emission increases very sharply with field strength, the cathode-spot position will be that of the peak field. It will be shown that the electron space charge has a significant effect on the position of the field's peak, and therefore influences the cathode spot position.

Quantitative calculations of the effect of magnetic fields on cathode electric field intensity would require a thorough knowledge of space charge distribution. Since this is unknown, only a qualitative discussion will be given here. For simplicity of description, we shall assume independent electric fields at the cathode, one caused by ion space charge (ion field) and one caused by electron space charge (electron field) (ignoring interactions between these). Figure

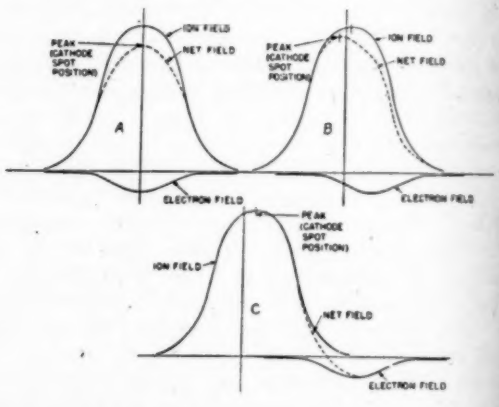

FIG. 1. Qualitative electric fields at the cathode surface. (Magnetic field into Paper.) Figure A—Zero magnetic field. Figure B—Small magnetic field. Shows retrograde motion of the peak field or cathode spot. Figure C—Large magnetic field. Shows the spot moving in the direction of the elementary particles.

1 shows the two fields and their sum, the net field, the peak of which determines the cathode-spot position.

Ions and electrons, having both opposite charges and directions of motion, will be deflected in the same direction by the magnetic field with the electrons being deflected hundreds of times farther than the ions because of their small mass. Thus when a small tangential magnetic field is applied, the average instantaneous position of the ions

and electrons (the space charge) will be displaced in the direction of their deflection. The electron field at the cathode will no longer partially neutralize the ion field symmetrically as in Fig. 1A but will have a greater neutralizing effect in the direction of their displacement, because of the larger electron displacement, as shown in Fig. 1B. Thus, surprisingly enough, while each of the component fields is shifted to the right, the peak of the net field is shifted to the left, thus accounting for the observed motion of the spot.

If the magnetic field intensity is increased greatly in magnitude, the electron and ion fields will be separated to the point of resolution, and then further displacement of the electron space charge would not influence the position of the net field maximum which would then be solely a function of the ion space charge. The displacement of the latter, small though it is, now solely determines the motion of the cathode spot (see Fig. 1C). This theory thus demands that the spot motion should reverse its direction as the magnetic field is greatly increased. This reversal has, indeed, been observed.[2]

Random motion will be superimposed on those described above because of irregularities in the cathode shape which will cause variations in the net field.

* Taken in part from Master's thesis submitted to the University of Pittsburgh.
[1] M. N. Minorsky, J. de phys. et rad. 9, 127 (1928).
[2] C. G. Smith, Phys. Rev. 62, 48 (1942); 64, 40 (1943); 69, 96 (1946).
[3] C. J. Gallagher and J. D. Cobine, Bull. Am. Phys. Soc. 22, 28 (1947).
[4] I. Langmuir, Gen. Elec. Rev. 26, 731 (1923); Zeits. f. Physik 46, 282 (1927).
[5] S. S. Mackeown, Phys. Rev. 34, 611 (1929).

Activities Induced by Pile Neutron Bombardment of Samarium*

MARK G. INGHRAM, RICHARD J. HAYDEN, AND DAVID C. HESS, JR.
Argonne National Laboratory, Chicago, Illinois
March 27, 1947

A SAMPLE of Sm_2O_3 was given a long neutron bombardment in the Hanford pile. By mass spectrographic analysis[1] active masses were observed at mass numbers 145, 151, 152, 154, 155, 156, 161, 167, 169, and 176. The interpretation of these active masses is given in Table I. Parentheses are placed about those half-lives which are tentative.

The assignment of samarium to certain of these active masses was made because samarium emits ions of form Sm^+ and SmO^+ from the heated oxide. The assignment of europium to other active masses was made because europium emits only as the metal. The 169 activity could conceivably have been caused by samarium, gadolinium, erbium, or ytterbium. Since no line was observed as mass 153 the possibility of samarium was ruled out. Gadolinium, which emits mostly as GdO^+, could have caused the line as could erbium or ytterbium emitting as Er^+ and Yb^+. However, since gadolinium was a known impurity in the samarium sample and no erbium or ytterbium impurities could be detected, it was concluded that the 169 mass line

TABLE I.

Mass No.	Ion	Active Isotope	Half-life
145	$Sm^{145}+$	Sm^{145}	>72 days
151	$Sm^{151}+$	Sm^{151}	(~20 years)
152	$Eu^{152}+$	Eu^{152}	(~ 5 years)
154	$Eu^{154}+$	Eu^{154}	(~ 5 years)
155	$Eu^{155}+$	Eu^{155}	2–3 years
156	$Eu^{156}+$	Eu^{156}	15.4 days
161	$Sm^{145}O^+$	Sm^{145}	>72 days
167	$Sm^{151}O^+$	Sm^{151}	(~20 years)
169	$Gd^{153}O^+$	Gd^{153}	>72 days
176	$Tb^{160}O^+$	Tb^{160}	72 days

was caused by a gadolinium isotope of mass 153. The mass observed at 176 was caused by 72-day terbium[2] emitting at TbO^+.

The Sm^{145} was formed by (n,γ) reaction on Sm^{144}. It probably decays by K-capture or positron emission to 61^{145}. Since the ratio of blackening at 145 and 161 positions is that characteristic of samarium, the half-life of the 61^{145} cannot be of the same order of magnitude as the half-life of Sm^{145}. The half-lives of Sm^{145} and Gd^{153} were shown to be greater than 72 days by comparison with the decay of 72-day Tb^{160}. The Sm^{151} has previously been observed only in fission.[3] It decays with a half-life of roughly 20 years to Eu^{151}. The europium activities at masses 152 and 154 were formed by (n,γ) reactions on impurities of europium in the samarium sample. In addition an appreciable part of the 154 observed was formed by the reaction

$$Sm^{152} \xrightarrow{(n,\gamma)} Sm^{153} \xrightarrow{\beta} Eu^{153} \xrightarrow{(n,\gamma)} Eu^{154}.$$
$$T_{\frac{1}{2}} = 47 \text{ hr.}$$

The 2–3 year Eu^{155} was formed by the reaction

$$Sm^{154} \xrightarrow{(n,\gamma)} Sm^{155} \xrightarrow{\beta} Eu^{155}.$$
$$T_{\frac{1}{2}} = 21 \text{ min.}$$

It has previously been observed only in fission.[2] The 15.4-day Eu^{156} had also been observed only in fission. Here it was formed by (n,γ) reaction on the Eu^{155}. The cross section for this reaction was calculated to be roughly $14{,}000 \times 10^{-24}$ cm^2. This is the first example of the determination of an absorbing cross section for a radioactive isotope by means of the mass spectrometer. The half-life of the europium activity at the 156 position on the plate was shown to be 15.4 days by the following method. The active plate was placed successively against various parts of a larger photographic plate for times calculated to give equal intensity at the 156 position if the half-life were 15.4 days. Four exposures were taken for successive times of 5 days, 6.4 days, 9.2 days, and 15.8 days. The lines at masses 152, 154, and 155 became denser with successive exposure, but the intensity of the 156 lines remained constant thus verifying that the half-life of the Eu^{156} was actually 15.4 days. The half-lives of the Sm^{145}, Gd^{153}, and Tb^{160} were determined by a similar method.

* This document is based on work performed under Contract No. W-31-109-eng-38 for the Manhattan Project at the Argonne National Laboratory.
[1] R. J. Hayden and M. G. Inghram, Phys. Rev. 70, 89 (1946).
[2] Bothe, Naturwiss. 31, 551 (1943).
[3] Rev. Mod. Phys. 18, 513 (1946).

The Quadrupole Moments and Spins of BR, Cl, and N Nuclei

C. H. TOWNES, A. N. HOLDEN, J. BARDEEN, AND F. R. MERRITT
Bell Telephone Laboratories, Murray Hill, New Jersey
April 4, 1947

FREQUENCIES and relative intensities of absorption lines near 24,000 megacycles in gaseous BrCN and ClCN have already been reported.[1] These lines represent rotational transitions $J=2$ to $J=3$ for BrCN and $J=1$ to $J=2$ for ClCN, which are split into a hyperfine structure. It has also been pointed out that the main features of this splitting appear to be caused by nuclear quadrupole moments.[2]

More detailed analysis of the spectra yields information about nuclear moments of Br, Cl, and N are shown in Table I.

The spins of the bromine nuclei are in agreement with values given by Tolansky,[4] but spins for the chlorine nuclei found by this work do not agree with the previously determined[5] value of 5/2. The spin of N^{14} is, of course, well known, and its quadrupole moment has been detected in the ammonia spectrum.[6] In the present case the coupling 3.66 Mc is not far different from the value 4.1 Mc for the ammonia molecule, and here we may determine the quadrupole sign, which could not be obtained previously. To determine the quadrupole sign for each nucleus, the sign of $\partial^2 V/\partial_z^2$ is assumed to be the same as that found in the hydrogen molecule.[7]

About one-third of the BrCN molecules are excited to the lowest vibrational (bending) mode at room temperature. Eight weak lines appear to be caused by these excited molecules, and in order to fit the observed positions of these eight lines, values must be assumed for the change in rotational constant with vibrational excitation and for *l*-type doubling. These values are consistent with what is known about such effects but cannot be exactly calculated. The rotational constant B_0 for the ground state is taken smaller by $B_0/340$ than $B_{(v_3=1)}$, the rotational constant for molecules excited to the first level of the bending vibrational mode. The *l*-type doubling, which is present in this excited state, gives a difference in the apparent value of $B_{(v_3=1)}$ for the two states of $B_{(v_3=1)}/1000$. Intensity ratios between two of the BrCN lines attributed to excited states and two lines attributed to the ground state were observed at +65°C and −40°C and found to change with temperature as expected by approximately a factor of two.

Agreement between experimental results previously

TABLE I. Data on nuclear quadrupole moments.

Nucleus	Spin	Sign of quadrupole moment	Quadrupole coupling* in megacycles
Br^{79}	3/2	positive	720±10
Br^{81}	3/2	positive	556±10
Cl^{35}	3/2	negative	84±4
Cl^{37}	3/2	negative	64±4
N^{14}	1	negative	3.66±0.15

* Quadrupole coupling is defined as $(eQ)\partial^2 V/\partial_z^2$ where Q is the nuclear quadrupole moment,[3] V is the electric potential produced at the nucleus by the rest of the molecule, and z is the coordinate along the molecular axis.

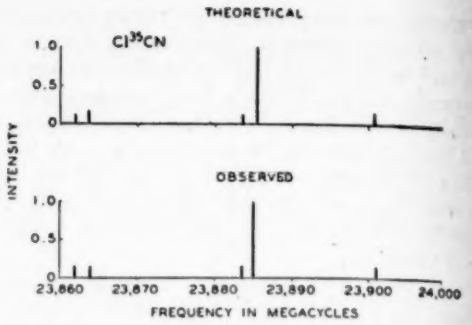

FIG. 1. Comparison of BrCN spectrum observed under low resolution with calculated pattern caused by Br quadrupole moment.

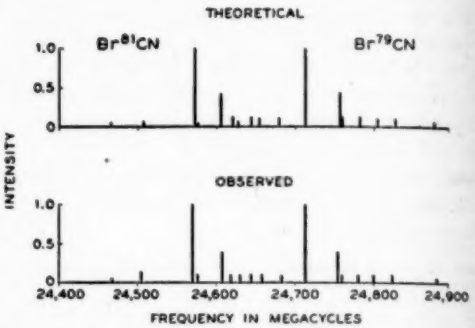

FIG. 2. Comparison of $Cl^{35}CN$ spectrum observed under low resolution with calculated pattern caused by Cl quadrupole moment.

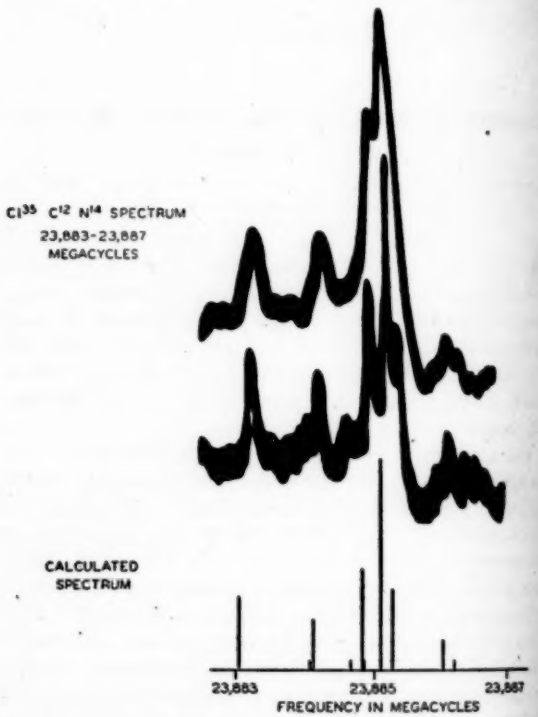

FIG. 3. Comparison of portion of $Cl^{35}CN$ spectrum under high resolution and spectrum calculated, including effects of both Cl and N quadrupole moments.

published and theoretical expectations[8] for BrCN is shown in Fig. 1, and for $Cl^{35}CN$ in Fig. 2, assuming quadrupole splitting caused by Br and Cl nuclei only. One of the lines shown for ClCN was not originally reported, since it had not at that time been resolved.

In order to detect the smaller splitting caused by nitrogen which was superimposed on the spectra of Figs. 1 and 2, it was necessary to increase the resolving power of the apparatus previously used. The oscilloscope trace of the two central lines of ClCN shown in Fig. 2 is displayed under high resolution[8] at two different pressures in Fig. 3. As a comparison, the theoretical splitting expected from N^{14} is included in the figure. The weaker line of the central pair is not split at all by N^{14} effects and is the lowest frequency component of this group. Other ClCN lines were observed under high resolution, and their splitting likewise agreed with expectations. The exact and detailed agreement between observations and theory leaves little doubt that the true value of the spins for the chlorine nuclei is 3/2 rather than 5/2.

Figure 3 gives an interesting indication of the high resolving power which can be obtained. Here, in spite of considerable difference in intensity, lines are resolved which are separated by only 140 kilocycles or 5×10^{-6} cm^{-1}.

[1] Townes, Holden, and Merritt, Phys. Rev. 71, 64 (1947).
[2] Townes, Holden, and Merritt, New York Meeting Am. Phys. Soc. paper X8.
[3] Kellogg, Rabi, Ramsey, and Zacharias, Phys. Rev. 57, 677 (1940).
[4] Tolansky, Proc. Roy. Soc. 136, 585 (1936).
[5] Elliott, Proc. Roy. Soc. 127, 638 (1930); Shrader, Phys. Rev. 64, 57 (1943).
[6] Dailey, Kyhl, Strandberg, Van Vleck, and Wilson, Phys. Rev. 70, 984 (1946); Coles and Good, Phys. Rev. 70, 979 (1946).
[7] Nordsieck, Phys. Rev. 58, 310 (1940).
[8] Details of theory and of experimental methods for obtaining high resolution will be published later.

Proposed Methods of Detecting the Neutrino

K. C. WANG
Department of Physics, National Chekiang University, Hangchow, China
March 24, 1947

IT has been pointed out by the writer[1] and others that the experimental investigation of K-electron capture of Be^7 may give a relatively easy way of detecting the neutrino. Allen[2] has actually carried out such an experiment with a positive result. However, this cannot be regarded as a decisive proof of the existence of the neutrino because, as commented on by some authors,[3] the method is still subject to relatively large corrections. We here propose some new methods of attacking the problem.

Recent experiments of Baldwin and Klaiber[4] have shown that, with x-ray of nearly 100 Mev, nuclear reactions of the types $Z_A(\gamma,n)Z_{A-1}$ and $Z_A(\gamma,pn)(Z-1)_{A-2}$ can occur with rather large probabilities. It thus seems not too difficult to prepare the nucleus B^{12} from C^{13} or N^{14}. If a cloud chamber is filled with gases containing C^{13} or N^{14} and then exposed to a source of 100 Mev x-rays, B^{12} will be produced in the chamber. Since B^{12} has a very large beta-ray energy (12 Mev) and its mass is comparatively small, it may be much easier to detect and to measure the momentum of the recoil nucleus than in the case of Cl^{38} (beta-ray energy 5 Mev) investigated by Crane and Halpern.[5] If, because of its too short lifetime (0.022 sec.), the investigation of the B^{12} recoils as suggested above is found not to be practicable, we propose the use of N^{16} from the reaction $O^{16}(n,p)N^{16}$. Let the cloud chamber be filled with oxygen; under the exposure to neutrons from a Li+D source, some N^{16} nuclei may be formed in the chamber. The expansion of the chamber then follows immediately after the cutting off of the neutron source because the lifetime of N^{16} is only 8 sec. So far as the observation of the recoil nuclei is concerned, N^{16} is also more favorable than Cl^{38} although not so favorable as B^{12}.

There is another method which may also prove valuable. Consider the nucleus Na^{24} which after β-radiation also emits a γ-ray or the internally converted electron (ϵ^--radiation). According to Konopinski,[6] this γ-ray may have a high multipole character and therefore may have a rather long life (about 10^{-7} sec. for octupole radiation). Thus after the β-emission, some of the recoil nuclei will, if they are allowed to move freely by placing the source and accessories in a high vacuum, travel a distance of the order of one centimeter before the emission of the γ-radiation or the ϵ^--radiation. This fact can be utilized to detect the neutrino by applying either the cloud chamber or "directional ϵ^--coincidence counting" technique. By "directional coincidence" we mean that the relative positions of the counters, the source, and the slits are so arranged that coincidence counting can be produced only when the direction of the β-emission and that of the recoil nucleus, which subsequently emits an ϵ^--particle, make a certain definite angle θ. If θ is always found to be 180°, it will be definite that no neutrino has been emitted during the β-disintegration. Otherwise, conservation principles can be used to find the energy and momentum of the neutrino, which can then be statistically checked with the Fermi theory. Even if Na^{24} is not suitable for our purpose, it is very probable that, for certain $\beta\gamma$ (not $\gamma\beta$)-radiative substances, the γ-radiation lifetimes lie between 10^{-7} and 10^{-4} sec. For these substances, there will be a high probability of internal conversion, thus favoring this method. (It is of interest to note that by measuring the length of the recoil path, the lifetime of such γ-radiation can be determined.) Besides, certain fission fragments, which emit β-rays quickly and successively, may also be useful. Finally, the natural $\beta\alpha$-radioactive substance ThCC′ may also be considered although the recoil mass is, in this case, too large, and the troublesome "aggregate recoil" may occur. After all, the possibility of carrying out experiments like these depends on the preparation of a "monolayer" source, since scattering process would probably confuse the results.

A third method is to utilize the K-radioactive property of certain substances like Be^7, Ca^{41}, Cr^{51}, etc. For some of these nuclei the K-capture may be followed by γ-radiation of rather long lifetime. By placing the source in vacuum, the two isomeric forms can be separated and tested for recoil by K-capture. The success of this separation will unambiguously prove the existence of the neutrino.

It may be mentioned that the investigation of the neutrino would also be possible from the meson disintegra-

tion. The general assumption, that positive mesons always decay into positrons and neutrinos while negative mesons are mostly absorbed by nuclei, cannot be regarded as well founded.[6] It seems to the writer that a coupling between a special counter arrangement similar to that designed by Rasetti[7] and a cloud chamber will be suitable for this investigation.

[1] K. C. Wang, Phys. Rev. 61, 97 (1942).
[2] J. S. Allen, Phys. Rev. 61, 692 (1942).
[3] E. J. Konopinski, Rev. Mod. Phys. 15, 209 (1943).
[4] G. C. Baldwin and G. S. Klaiber, Phys. Rev. 70, 259 (1946).
[5] H. R. Crane and J. Halpern, Phys. Rev. 56, 232 (1939).
[6] S. H. Neddermeyer and C. D. Anderson, Phys. Rev. 54, 88 (1938); Y. Nishina, M. Takeuchi, and T. Ichimiya, Phys. Rev. 55, 585 (1939).
[7] F. Rasetti, Phys. Rev. 60, 198 (1941).

Velocity of Propagation of the Discharge in Geiger-Müller Counters

ERNEST WANTUCH
Department of Physics, New York University, New York, New York
March 24, 1947

AN important factor limiting the counting-rate readily achievable with counters is the time required for the avalanche to spread along the length of the central wire. When an ionizing event occurs in the volume of the counter, the electrons will be drawn toward the positive central wire. Near the central wire the electrons will acquire sufficient energy to ionize gas atoms by collision. During the chain of ionizations by collision, recombination, and excitation, photons, as well as new secondary electrons, are produced. The photons travel out in all directions, and eject electrons, thereby spreading the discharge down the length of the counter. The spread velocity of the discharge was measured by two experimental arrangements.

1. The first arrangement consisted of a counter with a divided cylinder. The main section of the copper counter cylinder was 30 cm long and 1 cm in diameter. At each end was placed another section of the same diameter, 1 cm long. The separation between the sections was less than 0.1 cm. One central wire served as anode for the three sections.

The outputs from the end sections were applied to a timing circuit.[1] The resulting pulse which represented the time interval between the discharges of the two end sections was applied to the vertical plates of a DuMont 208 oscilloscope. The background of the counter (approximately 200 counts per minute) was used as our source of impulses. This resulted in a random distribution of time intervals which were observed on the oscilloscope. The maximum time-duration resulted from a discharge initiated at one end of the counter and travelling the length of the counter to be recorded at the other end. The timing circuit was calibrated by a pulse generator giving a pair of pulses of known time separation.

A critical analysis of this experimental arrangement showed that the measurements represented the time taken by the discharge to spread along the length of the counter plus any fluctuations in the time required to collect the positive ions at the cylinder. For this reason, an arrangement designed to minimize these fluctuations was devised.

TABLE I. Velocity of propagation of the discharge.

Gas (cm of Hg)	Max. time interval	Spread velocity
	Method 1	
0.6 cm ethyl alcohol 9.4 cm argon	5.7μ sec.	5.4×10^4 cm/sec.
1.0 cm ethyl alcohol 9.4 cm argon	6.7	4.6×10^4
2.0 cm ethyl alcohol 8.0 cm argon	8.0	3.9×10^4
3.0 cm ethyl alcohol 7.0 cm argon	8.9	3.5×10^4
	Method 2	
1.0 cm ethyl acetate 8.0 cm argon	4.5μ sec.	6.2×10^4 cm/sec.

2. A second counter was constructed consisting of a cylinder 30 cm long and 1 cm diameter. Small circular probes around the central wire were made of No. 26 platinum wire, and were of 0.14 cm inside diameter. The probes were located 28 cm apart.

Pulses obtained from these probes were separately amplified by one stage of 6SJ7 tubes, then combined in a suitable differentiating network. This resulted in a double pulse with the separation between the peaks representing the travel time of the discharge. The double pulse was further amplified by a video amplifier and applied to the vertical plates of a TS-28 synchroscope. The maximum time difference between the peaks can be interpreted in terms of the time scale of the sweeps. The experimental results are summarized in Table I. These results support the theory that the positive-ion sheath spreads by photon emission and ionization. When the proportion of organic vapor is increased, the travel time should increase as the organic molecule should absorb these photons and then pre-dissociate, thus removing the photon from the chain of ionizations. The fluctuations in the time required to collect positive ions at the cylinder must be comparatively small. Our results show a slower propagation velocity than results previously reported,[2] Huber, *et al.*, having found velocities approximately 50 percent higher than the values reported here for corresponding mixtures. One serious objection to their first method is the finite width of the pulses applied to the electrical shutters inside their counter. In their second method the sharp dependence of their experimental values on applied voltage cannot be accounted for.

The author wishes to thank Professor S. A. Korff for helpful suggestions.

[1] B. Rossi and N. Nereson, Rev. Sci. Inst. 17, 65 (1946).
[2] P. Huber, F. Alden, and E. Baldinger, Helv. Phys. Acta 19, 204 (1946).

Direction of Domain Magnetization in Powder Patterns

H. J. WILLIAMS
Bell Telephone Laboratories, Murray Hill, New Jersey
April 7, 1947

IN the course of an investigation of magnetic domain patterns, using colloidal particles of magnetite according to the well-known techniques,[1-4] a number of new patterns have been observed, and the directions of magnet-

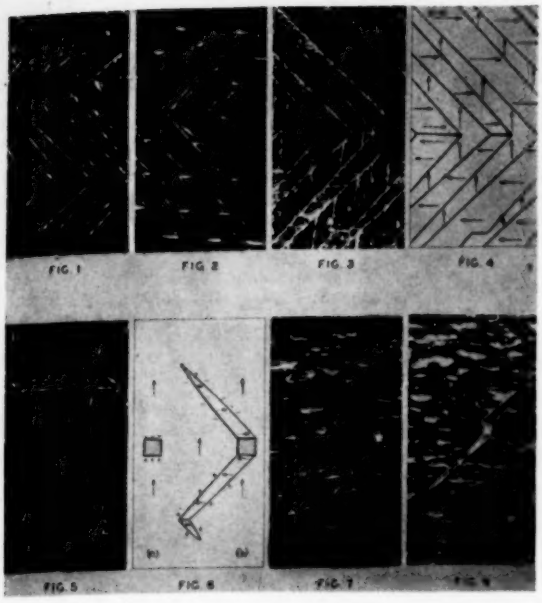

FIG. 1 FIG. 2 FIG. 3 FIG. 4

FIG. 5 FIG. 6 FIG. 7 FIG. 8

FIG. 1. Typical powder pattern on a (100) surface. Magnification about 150.
FIG. 2. Pattern on a (100) surface with a set of parallel scratches made with a ruling engine.
FIG. 3. Pattern on a (100) surface with horizontal and vertical scratches made with a glass fibre brush.
FIG. 4. Arrows indicate directions of magnetization of the domains in Fig. 3.
FIG. 5. Modification of pattern in Fig. 1 by tension, within elastic limit, applied in a horizontal direction.
FIG. 6. (a) Cavity with magnetic poles on the surface. (b) Domain formation having lower energy, proposed by Néel.
FIG. 7. Actual pattern around cavity.
FIG. 8. Pattern around another cavity.

ization in these patterns have been determined. Some of the results of the incomplete investigation are presented here.

The (100) face of a single crystal specimen of iron containing 3.8 weight percent silicon was polished electrolytically to give a strain-free surface. The pattern obtained is of a new and readily interpreted nature, and the interpretation has been checked by several new experiments. Figures 1, 2, and 3 are examples of the pattern for the demagnetized condition. The interpretation (Fig. 4 corresponding to Fig. 3) shows the domains as magnetized in the directions of easy magnetization, <100> for silicon iron, with the pattern arranged so as to minimize the poles produced on the boundaries in accordance with theory.[4,5]

This interpretation is confirmed by two new experiments involving (1) scratching the surface, a technique suggested by Dr. W. Shockley, and (2) applying mechanical stress. In Fig. 2 the horizontal dashes show portions of a series of parallel continuous scratches made by a conical sapphire point and a ruling engine, and reduced in intensity by an electrolytic polish. In the tapered regions the scratches show strongly; according to Fig. 4, in these regions the flux is perpendicular to the scratch; consequently, some flux leaves the metal and attracts the colloid. Where the scratch is parallel to the flux, no field emerges, the colloid is not collected, and the scratch is faint or imperceptible. Figure 3 shows the same effect with scratches running horizontally and vertically made by a brush of fine glass wool.

Applying mechanical tension horizontally favors the horizontally magnetized domains from an energetic viewpoint since silicon iron has positive magnetostriction. When stress is applied, the tapered regions of Fig. 1 (which are unfavorably magnetized) are seen to shrink, and the pattern of Fig. 5 is obtained. On releasing the stress, tapered regions reappear. All of this confirms the interpretation given in Fig. 4.

The tapered regions of the pattern arise because the face is not accurately parallel to (100). This phenomenon, together with the effects of applied magnetic fields, will be discussed at a later date.

A further aid to the interpretation of Fig. 5 is furnished by the vertically elongated splotches. These are thought to be caused by roughness of the surface (prolonged electrolytic polishing produces a lemon-peel appearance) and act through the same mechanism as the scratches. Unlike the domain boundaries, the splotches appear always in the same place. They show up best when a concentrated colloid is used and serve, as the scratches do, to interpret direction of magnetization.

The effect of a hole in the silicon iron is shown in Figs. 7 and 8. Patterns of this kind, as shown in Fig. 6, have been predicted by Néel.[6] The magnetostatic energy caused by the concentration of poles on the surface of an inclusion (Fig. 6a) is reduced by the domain structure (Fig. 6b) which distributes the poles along the curved portions of the boundaries. As the domain elongates the magnetostatic energy decreases and the wall energy increases, and that structure occurs for which the sum of the two energies is a minimum.

[1] F. Bitter, Phys. Rev. 38, 1903–1905 (1931); 41, 507–515 (1932).
[2] L. von Hámos and P. A. Thiessen, Zeits. f. Physik 71, 442 (1931).
[3] L. W. McKeehan and W. C. Elmore, Phys. Rev. 46, 226–228, 529–531 (1934).
[4] W. C. Elmore, Phys. Rev. 62, 486–493 (1942).
[5] Louis Néel, Cahiers de Physique, No. 25, 1–20 (December, 1944).
[6] Louis Néel, Cahiers de Physique, No. 25, 21–44 (December, 1944).